New techniques and first results toward measuring the $6S_{1/2}$ to $5D_{3/2}$ magnetic-dipole transition moment in Ba^+

Spencer R. Williams

A dissertation
submitted in partial fulfillment of the
requirements for the degree of

Doctor of Philosophy

University of Washington

2015

Reading Committee:

Boris B. Blinov, Chair

Subhadeep Gupta

Andreas Karch

Program Authorized to Offer Degree:
Physics

University of Washington

Abstract

New techniques and first results toward measuring the $6S_{1/2}$ to $5D_{3/2}$ magnetic-dipole transition moment in Ba^+

Spencer R. Williams

Chair of the Supervisory Committee:
Associate Professor Boris B. Blinov
Department of Physics

We report the final results from our first-generation attempt to measure the magnetic-dipole transition moment (M1) between the $6S_{1/2}$ and $5D_{3/2}$ manifolds in Ba^+. Knowledge of M1 is crucial for a parity-nonconservation experiment in the ion where M1 will be a leading source of systematic error. To date no measurement of M1 has been made in Ba^+, and moreover, the sensitivity of the moment to electron-electron correlations has confounded accurate calculations as well. A precise measurement may help to resolve the theoretical discrepancies while providing essential information for planning a future PNC measurement in Ba^+. We describe a variety of new measurement techniques that could be useful ultimately measuring M1.

TABLE OF CONTENTS

Page

List of Figures iii

Glossary vii

Glossary viii

Chapter 1: Introduction 1

Chapter 2: Theoretical Preliminaries 5
2.1 General features of atomic structure 5
2.1.1 The valence structure of Ba^+ 8
2.2 Effects of external electro-magnetic fields on atoms internal states 9
2.2.1 The Zeeman effect 10
2.2.2 The Stark effect 12
2.2.3 Laser driven transitions between atomic energy levels 13

Chapter 3: Experimental techniques 18
3.1 Ion trapping 18
3.1.1 A trapping potential for charged particles 18
3.1.2 Photo-ionization and loading the trap 20
3.2 Laser cooling 22
3.3 Optical pumping 24
3.4 State detection by electron shelving 27
3.4.1 Pulse sequences for driving 2051 nm transitions 31
3.4.2 Pulse sequence for rf spectroscopy 35

Chapter 4: The Ba^+ Apparatus 37
4.1 Our trap 37
4.2 Vacuum system 39
4.3 Fluorescence collection optics 40

4.4 The Ba^+ lasers . . . 41
4.4.1 Photo-ionization: 791 nm and 337 nm . . . 41
4.4.2 Shelving and Deshelving: 455 nm and 614/1228 nm . . . 42
4.4.3 Laser cooling and repump: 493/986 nm and 650 nm . . . 48
4.4.4 Forbidden spectroscopy: 2051 nm . . . 53
4.4.5 Optics at the trap . . . 58

Chapter 5: Measurement of $M1$ for the $6S_{1/2} \leftrightarrow 5D_{3/2}$ transition . . . 60
5.1 Deriving formulas for E2 and M1 contributions to Ω . . . 60
5.1.1 Coordinates . . . 60
5.1.2 The magnetic-dipole and electric-quadrupole contributions to $\Omega^{(\Delta m)}$ . . . 61
5.2 Description of two pedagogical methodologies . . . 67
5.2.1 A sketch of the ideal polarization rotation technique . . . 67
5.2.2 A sketch of the ideal reversals techniques . . . 70
5.3 A birefringence-enhanced measurement technique with demonstration . . . 74
5.3.1 Derivation of a practical laser field model . . . 74
5.3.2 Simulation of the experiment . . . 88
5.3.3 Data and analysis . . . 91
5.4 Comments on systematic effects . . . 107
5.4.1 Magnetic field drift and noise . . . 107
5.4.2 More on polarization distortions and noise . . . 112
5.4.3 Other concerns from the 2051 nm laser . . . 115
5.4.4 Ion temperature effects . . . 117
5.5 One final measurement of $\Omega^{(0)}(\phi)$ . . . 118

Bibliography . . . 121

LIST OF FIGURES

Figure Number — Page

2.1 A diagram showing the important energy levels, the resonance frequencies between them, and their uses for Ba^+. The separations between the different levels are not to scale. . . . 9

2.2 A table of g_{eff} for all 2051 nm transitions. . . . 12

3.1 A plot of the ion's position over time modeled by the Matthieu equation. The slow, large amplitude is the ion's secular motion. The fast and small amplitude oscillation is the driven motion from the drive RF, known as micro-motion. Here $q_i/A = 1/10$ and $\omega/\Omega_{RF} = 400$. . . . 21

3.2 A partial energy level diagram for neutral Ba showing the transitions and energy levels that could be used for photo-ionization of the atom. . . . 22

3.3 A diagram of Ba^+ valence structure including its Zeeman substructure and with the optical pumping transitions indicated. The unidirectional dashed blue line represents spontaneous decay from the excited $6P_{1/2}$ state to either of the $6S_{1/2}(m_J = \pm 1/2)$ states. In the figure the 493 nm beam is shown as having $\sigma^{(+)}$ handedness which continuously drives population out of the $6S_{1/2}(m_J = -1/2)$ till the ion completely occupies the $6S_{1/2}(m_J = +1/2)$ state. . . . 25

3.4 A visual summary of shelving and deshelving. Clockwise: An ion addressed only by 493 nm will be pumped to $5D_{3/2}$; cycling between 493 nm and 650 nm transitions the ion will fluoresce; by adding 455 nm radiation the ion is pumped into the $5D_{5/2}$ and the ion will no longer fluoresce since it has been removed from the cooling cycle; addressing the ion with the 614 nm laser will return the ion to the cooling cycle and florescence will resume. . . . 27

3.5 A plot of ion florescence collected from our apparatus while the cooling lasers were applied to a single ion. The blue line tracks photon counts collected per 50 ms. The higher average count rate level was due to 493 nm light scattered by the ion from the cooling laser. At the time indicated on the plot a 455 nm pulse was delivered to the ion, shelving it in the $5D_{5/2}$ and resulting in complete extinction of the ion florescence. After a pulse of 614 nm light the ion was returned to the cooling cycle and the florescence returned. . . . 28

3.6 Three examples of frequency scans with the 2051 nm exposure time set to 100 μs, 300 μs, and 450 μs for a configuration where the π-time was $\sim$100 μs. 33

3.7 A plot of two ARP scans that identify all eight 2051 nm transitions. Each bin is 400 kHz wide, corresponding to the width of the ARP sweep. For the orange scan we optically pumped to the 6S($m_j = -1/2$) state and for the blue to the 6S($m_j = 1/2$) state. From left to right the tall orange bins correspond to $\Delta m = +2$, +1, 0, -1, the blue to $\Delta m = +1$, 0, -1, -2. 34

4.1 The upper image is a photograph of our trap inside the vacuum system. The trap was housed inside a Kimball Physics, Inc. 6 inch spherical octagon, whose pressure was maintained by a 20 L/s ion pump (not shown). The lower drawing shows our ion trap inside the spherical octagon and the coils we used to generate the magnetic field. The CAD model was created by Matt Hoffman. 38

4.2 A photograph taken from our EMCCD camera of the collected fluorescence from a single trapped barium ion in our ion trap. 40

4.3 A schematic of the combined 337 nm and 791 nm beam lines 42

4.4 A photograph of the 455 nm laser head. 45

4.5 Schematic of the 455 nm beam line. 46

4.6 Schematic of the 1228/614 nm beam line. 48

4.7 Schematic of the 986/493 nm beam line. 49

4.8 Schematic of the 650 nm beam line. 53

4.9 A photograph of our ULE cavity taken by former graduate student Jeff Sherman. Not shown is the vacuum system within which it lives. 55

4.10 Schematic of the 2051 nm beam line. The black solid line traces the 2051 nm beam path while the gold follows the 1025 nm path. Dashed lines indicate electrical connections. The remaining symbols are defined in the text. 56

4.11 A schematic of the spherical octagon housing for our ion trap showing the approach of each laser to the ion. The static magnetic field that define the ion's quantization axis are the brown bands that point parallel to the cooling and photo-ionization beams. Note that the 2051 nm beam approach is nominally 90° to that axis. 58

5.1 The primed coordinate system defines the laser frame with the Z$'$-axis set along the 2051 nm laser. The unprimed coordinates define the atom's frame with the Z-axis set along the externally applied magnetic field **B**. The Y and Y$'$ axes are parallel and point out of the page. 61

5.2 A theoretical plot of $\Omega^{(0)}(\phi)$ driven by a linearly polarized 2051 nm beam assuming perfect linear polarization. For this sketch $|A_{E2}|$ is set to ∼10 kHz and $|A_{M1}|$ to ∼30 Hz. 69

5.3 A theoretical plot of $\Omega^{(\pm 2)}(\phi)$ driven by a linearly polarized 2051 nm beam assuming perfect linear polarization. For all curves C_{E2} was set to 25 kHz. Each color corresponds to a different value of θ with red, orange, yellow, green, blue, purple corresponding to 40°, 50°, 60°, 70°, 80°, 90°. 70

5.4 Close up plots of the $\Delta m = 0$ transitions driven by perfect circular polarized laser fields. The red and blue curves are obtained for specific choices of states and laser handedness as described in the text. The dashed back curve shows either transition without any magnetic-dipole coupling and with the beam oriented along $\hat{x}'$ to maximally drive the transition. 71

5.5 A drawing of the polarization control section of the 2051 nm beam line. . . . 75

5.6 A CCD image of the stress pattern in the view port obtained by shining incoherent red light through the view port between a pair of crossed polarizers. The image shows the stress-optic behavior of the view port qualitatively. Bright regions in the image correspond to higher amounts of stress-induced birefringence. The view port edge is indicated in white. 81

5.7 Ratio of P_{Min} to P_{Max} as a function of P1 orientation at the center and ±2.25 mm off center of the view ports. The data is fit to Eq. (5.34) to get Γ and α for each spatial incidence. 82

5.8 Plots of $\Omega^{(0)}$ for the birefringence-enhanced measurement technique. The plot on top shows the full-scale behavior, and the bottom plot zooms in on the minimum feature from which M1 can be extracted. For every plot α was set to 65° and θ was set to 70°, which are experimentally realistic values. Each color represents a different retardance in the arbitrary phase retarder with black, red, purple, and blue corresponding to 0°, 5°, 10°, and 20°, respectively. The dashed lines in the zoomed-in plot have A_{M1} set to zero, and in the solid lines it is 30 Hz. In all plots A_{E2} is 15 kHz. 89

5.9 Plots of both of the $\Omega^{(\pm 2)}$ transitions including the effects of the view port birefringence. The blue and red curves correspond to $\Delta m = +2$ and $\Delta m = -2$, respectively. For this simulation the view port's optical axis, α was set to -20° and its retardance, Γ, was set to 5°. 90

5.10 An example of a Rabi oscillation taken along the 2051 nm $\Delta m=0$ transition. 92

5.11 Plots of the $\Omega^{(0)}$ and $\Omega^{(+2)}$ data sets along with their fits, which are described in the text. The lower panel displays the fractional residuals for both fits. . 98

5.12 The top panel displays plots of the data and the fit of the $\Omega^{(\pm 2)}$ measurements fitted simultaneously to the birefringence laser field model. The blue indicates the $\Delta m = +2$ data and the red indicates the $\Delta = -2$ data. The lower panel shows the fractional residuals from the simultaneous fit of both transitions. . 100

5.13 The top panel shows the ratio between the $\Omega^{(+2)}$ and $\Omega^{(-2)}$ data sets and the bottom panel shows the square difference $\left|\Omega^{(+2)}\right|^2 - \left|\Omega^{(-2)}\right|^2$. From these curves we are able to extract the view port optical axis orientation and retardance experienced by the 2051 nm beam. 102

5.14 Measurements of the ground state Zeeman splitting (or spin-flip resonance frequency) for two and a half hours immediately after loading a single ion. Here we found that the resonance relaxes with a time constant of 26 minutes. 108

5.15 Photographs of our magnetic shielding before being installed and *in situ*. . . . 110

5.16 An example of a ground state spin-flip Rabi oscillations after the installation of magnetic shielding. From these data we know our magnetic field decoherence rate to be better than 5 ± 1 Hz in the ground state. Notice that the horizontal scale is reported in seconds, instead of our usual micro-seconds. . . 111

5.17 The first 50 Rabi oscillations in the ground state. The fitted Rabi frequency was 41.735 kHz ± .003 kHz with a decoherence rate of 0.024 kHz ± 0.009 kHz with a χ^2 of 1.7. 112

5.18 Data and fit for a polarization rotation measurement along the Δm = 0 transition after the installation of our magnetic shielding. In this attempt we found $A_{E2} = 4863 \pm 17$ Hz and $A_{M1} = 13 \pm 12$ Hz. The phase offset ϕ_0 was equal to $85.25^\circ \pm 0.02^\circ$, which indicates a significant change to the experiment's geometry from prior to the shielding's installation. 119

5.19 The slowest 2051 nm transition observed in our experiment at the time of writing this thesis. For this oscillation we found a (linear) Rabi frequency of 44 ± 1 Hz with a decoherence rate of 7 ± 1 Hz. 120

GLOSSARY

APNC: Atomic parity nonconservation.

AOM: Acousto-optic modulator.

CGC: Clebsch-Gordan coefficients.

ECDL: External cavity diode laser.

EMCCD: Electron multiplying charge coupled device.

EOM: Electro-optic modulator.

FWHM: Full width at half max.

HWP: Half-wave plate.

LED: Light emitting diode.

ND: Neutral density (filter).

OP: Optical pumping.

PBS: Polarizing beam splitter.

PMT: Photo-multiplier tube.

PNC: Parity non-conservation

PPLN: Periodically-poled lithium niobate.

RIN: Relative intensity noise.

RF: Radio frequency.

SHG: Second harmonic generation.

ULE: Ultra-low expansion.

SYMBOLS

Mathematical Symbols

$\sim$: Relation for rough equivalence.

$\lesssim$: Relation for approximately less than.

$\approx$: Relation for approximately equal.

$\vec{X}$: Indicates object X as a vector.

$\hat{X}$: Indicates object X as an operator.

i: The complex unit $\sqrt{-1}$.

$\mathcal{O}$: Indicates the rough size or order of magnitude of a quantity.

$|\ \rangle$: A state vector "ket".

$\langle\ |$: The dual of the "ket" state vector "bra".

Physical Symbols

a_0 Bohr radius.

Ba^+ A singly ionized atom of Barium.

B: Magnetic field.

c: The speed of light.

E: Electric field.

Ej: Electric multipole transition moment of order j.

$\Gamma(\gamma)$: Retardance or decoherence based on context.

$\hbar$: Reduced Plank's constant.

Mj: Magnetic multipole transition moment of order j.

Ω: Rabi frequency.

μ_B: Bohr magneton.

ACKNOWLEDGMENTS

First thanks must be given to my advisor, Boris Blinov, for taking me into his group without my knowing a single thing about experimental physics. Thank you for guiding my development as a physicist over these years, and for managing us through the numerous obstacles, both scientific and otherwise, that we continually encountered. Thanks, finally, for not fulfilling your promise to fire me until the measurement was finished. You can fix the glitch now.

Next I owe gratitude to Norval Fortson, who first presented the idea for pursuing these measurements and also for his many insights at the beginning of the project.

Thank you to the other members of my reading committee, Andreas Karch and Subhadeep Gupta, for taking time to read through this document. And also, thank you Ruby Byrne, for the commas.

I am grateful to all of my peers from whom I have learned and grown so much - both professionally and personally. Most notably Anupriya Jayakumar, with whom I collaborated with closely during the first year of this project. It was an absolute privilege to work you. Special thanks as well to Matthew Hoffman for training me on our apparatus and for sharing your experience in optics and atomic physics. Also to the rest of the graduate students and post-docs of our group with whom I overlapped: Carolyn Auchter, Chen-Kuan Chou, Richard Graham, Tom Noel, Tomasz Sakrejda, John Wright, and Zichao Zhou. And also to the long list of undergraduates that joined us throughout these years, for their vast and varied contributions to our work: Matthew Bohman, Toby Bothwell, Morgan Catha, Andrea Johnson, Eric Josberger, Robin Mumm, Sean Nelson, Colby Schimelfenig, Alex Sivitilli, and Wen Lin Tan

The apparatus we used daily would not have existed without the assistance and mentorship of the Physics Department's machinists. In particular, I am grateful for the teaching

and friendship of Ron Musgrave who was by far the most patient collaborator I have ever had the pleasure of working with.

Thank you to the administration of the University Washington's Department of Physics for the extensive support that they provided to me. In particular, I am grateful for the constant support I received from Catherine Provost, and also for the front office staff who were always accommodating.

Finally to thank you to my family, without whose love and support I would not have been capable of completing this feat.

DEDICATION

To my mom,

who shared with me the greatest love I have ever known.

Chapter 1

INTRODUCTION

The attack may or may not have been capable, but it was certainly justified.

Sef Sermak - Foundation

Most of my graduate school career was spent in pursuit of a single number: the magnetic-dipole transition moment (M1) for the $6S_{1/2} \leftrightarrow 5D_{3/2}$ transition of a barium ion (Ba^+). What has come from this effort? Writing at the end of that period, I claim, with relief or regret, that we know $M1$ to be below $93 \times 10^{-5}\,\mu_B$. Ours is the first measurement of this M1, and the details of that experiment are the subject of this thesis. Interest in measuring this somewhat obscure object derives from its significance to a decisive point in a wandering but fascinating narrative whose exposition sets us far afield of our target.

For most of the history of physics it was thought plausible that parity, the three dimensional analog to reflection symmetry, was a fundamental symmetry of nature. However, in the 1950s, along the path to describing the weak interaction, it was shown that the weak interaction does not conserve parity [1, 2]. This discovery was in its own right a revelation, and was a crucial step toward a theory of the weak force. Ultimately, by way of electro-weak unification, this work became part of the Standard Model, which, at the time of writing, was theorist's best articulation of the interactions between fundamental particles.

Those earliest investigations of parity non-conservation (PNC) in the interactions considered β-decay phenomena, but shortly after theorists began to ask whether PNC could be observed in the spectrum of atoms as well [3]. The early conclusion was no; the effect would be too small. However, in the 1970s, inspired by advances in laser technology and electro-weak theory, the question was revisited [4, 5], and the other conclusion reached. In that study it was found that the effective interaction Hamiltonian describing the exchange of a Z^0 boson between the electrons of a hydrogen-like atom and its nucleus scales as the atomic number, Z, cubed. This means that if an experiment were pursued with an atom of,

say, Z = 56, then the parity-violating effect would benefit from about 2×10^5 enhancement from what had been previously predicted. This enhancement elevates atomic parity non-conservation (APNC) in heavy atoms from minute, obscure effect to something observable.

The motivations for pursuing an APNC experiment are diverse and, in some instances, lofty. Perhaps the most ambitious hope for APNC studies are their potential to reveal physics beyond the Standard Model [6, 7]. This theory was famous, and maybe still is at the time of your reading, for its unprecedented predictive power - for example, for predicting the existence of the Higgs boson that was discovered in 2012 - but also for being incomplete [8]. At the time of writing there was a frenzy of theoretical work being undertaken to look for extensions to the Standard Model, some of which make predictions testable by APNC studies [6]. In addition to phenomena of particle physics, APNC studies have been shown to be sensitive to interesting nuclear physics [9, 10]. These emerge from the hadron-hadron sector of the weak interaction, which produces additional parity-violating structure in the atom, called nuclear anapole moments. The most precise APNC measurement to date was able to observe such an anapole moment [11].

Experiments to measure APNC have undergone several generations of refinement and reinvention with results reported for a variety of atomic systems. Histories of these studies are given in several reviews, for example [12, 13]. One approach of particular interest for a next-generation APNC study is to look for the effect in a single trapped Ba^+ ion [14]. In that system the observable consequence of APNC is a small electric-dipole transition moment ($E1_{APNC}$) between the ion's $6S_{1/2}$ ground states and its low-laying metastable $5D_{3/2}$ states. Without APNC a parity selection rule forbids this kind of coupling between the states, however the weak interaction relaxes that constraint. The question of how large $E1_{APNC}$ is expected to be in Ba^+ has been addressed by several numerical studies that have determined [15, 16, 17],

$$\left|E1_{APNC}\right| \approx 2 \times 10^{-11} e a_0 \tag{1.1}$$

where a_0 is the Bohr radius and e is the electron charge. To measure $E1_{APNC}$ it was pointed out that an interference could be induced between it and the leading order electric-

quadrupole moment (E2) so that the total transition rate to first order in A_{PNC} is [14],

$$A^2 = \left|A_{E2} + A_{PNC}\right|^2 \approx A_{E2}^2 + \mathrm{Re}\{A_{E2}A_{PNC}^*\} \tag{1.2}$$

The leading term A_{E2}^2 is a scalar, however the interference cross term, being generated from the parity-violating interaction, is a pseudo-scalar. By changing the parity of the measurement (for example, by reversing the orientation of the experiment's quantization axis) the sign of the interference term is changed, providing experimental access to $\mathrm{E1}_{APNC}$. E2 is known from measurements of the lifetime of the $5\mathrm{D}_{3/2}$ states [18], as well as from theory [16] to be,

$$\left|E2\right| = 12.7\ ea_o^2 \tag{1.3}$$

The point of the work herein is not to measure $\mathrm{E1}_{APNC}$, but rather to address a serious systematic effect that must be understood before that measurement can be pursued. In addition to E2 and $\mathrm{E1}_{APNC}$, there is also a magnetic-dipole transition moment, $M1$, between the $6\mathrm{S}_{1/2}$ and $5\mathrm{D}_{3/2}$ states. Including that moment into Eq. (1.2), and dropping terms below order $A_{M1}A_{PNC}$, gives,

$$A^2 = \left|A_{E2} + A_{M1} + A_{PNC}\right|^2 \approx A_{E2}^2 + A_{M1}^2 + \mathrm{Re}\{A_{E2}A_{PNC}^*\} + \epsilon\,\mathrm{Re}\{A_{E2}A_{M1}^*\} \tag{1.4}$$

Two additions appear: the second quadratic term A_{M1}^2 and an additional interference term $\mathrm{Re}\{A_{E2}A_{M1}^*\}$, which is a scalar, but arises from the fact that if the parity reversal is not done perfectly, then this additional interference term will emerge and mimic the sought-after PNC interference. The parameter ϵ describes the degree to which the parity reversal is missed. How big of a problem is this? It depends on the size of M1. The E2 - M1 interference term in Eq. (1.4) is linear in M1, making it a critical concern for the design of a future PNC study in the atom.

Before pursuing a measurement, we must know at least the rough size of M1. Three calculations of M1 have been performed to our knowledge; they report (in units of the Bohr magneton, μ_B),

$$M1 = \begin{cases} 80 \times 10^{-5}\ \mu_B & [19] \\ 22 \times 10^{-5}\ \mu_B & [20] \\ 17 \times 10^{-5}\ \mu_B & [21] \end{cases} \tag{1.5}$$

The variety of these results should be alarming. The E2 - M1 interference term in Eq. (1.4) is linear in M1, so the factor of four between some of the predictions is a concern. To give a sense of scale of the problem, Table (1.1) lists the predicted and relative size of E2, M1, and $\mathrm{E1}_{APNC}$. From the calculated values of M1 we expect its contribution to be $\wr(10^{-3})$ that of $E2$, however, that is still four orders-of-magnitude larger than the parity-violating contribution; it is a big concern.

All of this is not to say that measuring M1 does not have some seductive quality all its own. To calculate M1, a relativistic treatment of the atom is needed, for which several methods exist; for example, those described in [23] and [24]. The problem though, as discussed in the literature [19] and in private communication [21], is that electron-electron correlation in the atom produces the leading order contribution to M1 and that is hard to calculate accurately within current methods. A measurement of the quantity, then, could be useful for improving the inclusion of many-body correlation effects into future atomic structure calculations.

This thesis describes our strategies for measuring M1 and the results of our first generation attempt of the measurement. These are the topics covered extensively in Chapter 5. Between here and there we will describe enough atomic theory and experimental technology that one could continue what we have started. I hope that mine will not be the final word.

Table 1.1: Calculated [19, 22, 16, 23, 17, 20, 21] and relative sizes of the transition moments between $6S_{1/2}$ and $5D_{3/2}$ in Ba^+. The calculated values are listed in units of ea_0, where e is the electron charge and a_0 is the Bohr radius. The fine structure constant α and the transition wavelength λ enter so that a *bona fide* comparison can be made with these units.

E2	M1	$\mathrm{E1_{PNC}}$
12.7 $(\frac{a_0}{\lambda})$	20 - 80$\times$ 10^{-5} (μ_B)	$\sim 2\times$ 10^{-11}
~ 1	$\sim 10^{-3}$	$\sim 10^{-7}$

Chapter 2

THEORETICAL PRELIMINARIES

In this exceedingly complex and mystique-haunted preserve we can only, like the fools of the aphorism, rush good-naturedly in, make what points we regard as basic and rush even more quickly out again, before the sticklers take us apart.

- Irma S. Rombauer and Marion Rombauer Becker. Joy of Cooking.

Experimental atomic physicists are the beneficiaries of over one hundred years of theoretical efforts to describe atoms. The body of knowledge atomic theorists have produced is vast, growing, and indispensable to the experimentalist. The experiments to be described in this thesis require some familiarity with this parallel world. For the reader's benefit this chapter will review a number of pertinent concepts, to which my only service is as editor. More complete and rigorous treatments of these topics can be found in any number of standard texts covering quantum mechanics and atomic physics [25, 26, 27, 28, 29]. In particular this account will be limited to basics of atomic structure and the interaction between atoms and electromagnetic fields. Topics of a more specialized variety will be explained elsewhere as they are needed.

2.1 General features of atomic structure

What is meant by atomic structure has been a moving target through the history of physics. Today what we mean is defined under the quantum mechanical paradigm, under which one asks, what are the atom's energy levels and how are they distributed? The most refined models theorists have for describing answering these questions include many subtle features (PNC among them) and it is not our business here to paraphrase that complexity. Here we will only remind the reader of the salient qualitative features of the simpler toy models that are in many cases wholly sufficient.

The atom we wish to have a picture for is Ba^+ which, having a single valence electron,

has a spectrum that qualitatively matches that of Hydrogen, for which analytic solutions are obtained in nearly every quantum mechanics and atomic physics text book. From solving the Schroedinger equation for a hydrogen-like atom one finds the energy levels are grouped according to a quantum number n, that we call the principle quantum number, according to the formula,

$$E_n = \frac{-Ry\, Z^2}{n^2} \tag{2.1}$$

The coefficient Ry is the Rydberg constant which is approximately [30],

$$Ry \approx 13.6 \quad \text{eV} \tag{2.2}$$

Formula (2.1) applies to a system of a heavy nucleus to which is bound a single electron, however this grossly over estimates the energy levels of a hydrogen-like ion like Ba^+. In a hydrogen-like ion the more tightly bound electrons effectively screen the lone valence electron from the nucleus. In the absence of external fields these core electrons form closed spherical shells around the nucleus so that the net electrostatic field of the core electrons and the nucleus can be roughly accounted for by using an effective, or screened, nuclear charge Z_{eff}. In principle calculating Z_{eff} requires some detailed knowledge of the electron's wave functions [31], however if we naively take it to be the nuclear charge Z less the core electrons (54, for Ba^+) then we find that the ionization energy from the ground state, for which n = 6, should be on the order of 1 eV, which is order-of-magnitude correct [1].

In addition to the quantum number n, the Schroedinger's equation predicts that different atomic states carry different amounts of angular momentum as well, described by the quantum number l, which we call the orbital angular momentum quantum number. Schroedinger's equation requires that for any given n, that l be an integer between 0 and n - 1. Intuitively we expect states with greater angular momentum to experience something like a greater centrifugal force, pulling the electron further away from the nucleus. Which is equivalent to saying that states of greater l should be less bound than those with lower l. The orbital angular momentum quantum number is a victim of historical naming conventions, and being bound by tradition we too will use so-called spectroscopic notation. In

[1] The ionization energy is needed to remove the least-bound electron from an atom. This topic will be discussed later on in 3.1.2. The actual value for Ba^+ is 5.21 eV [32].

that labeling scheme $l = \{0,\ 1,\ 2,\ 3,\ ...\}$ are labeled {S, P, D, F, ...}. These effects are the dominant features in what could be called gross atomic structure. For the experiments we will describe in this thesis, the only levels from the gross structure that concern us, in descending order of energy, are the 6S (ground state), 5D, and 6P levels.

One final qualitative feature to include is the half-integer elephant of atomic physics, spin angular momentum. Electrons, like other elementary particles, carry an additional angular momentum intrinsically, that we call spin, that is equal to $\hbar/2$. This extra source of angular momentum combines with the electron's orbital angular momentum to give the total angular momentum, $j = l \oplus s$, and adds "fine structure" to the energy levels through the spin-orbit interaction. If we ignore the origin of spin, the effect can be motivated through classical electrodynamics. Because of the electron's intrinsic spin angular momentum, $\hat{S}$, it also has a magnetic-dipole moment,

$$\hat{\mu}_s = -g_s \mu_B \frac{\hat{S}}{\hbar} \tag{2.3}$$

For states with orbital angular momentum, $\hat{L}$, the electron can be thought of as "orbiting" the nucleus at a velocity $\vec{v}$ through the electrostatic field $\vec{E}$ from the nucleus, for which it will see an effective magnetic field,

$$\vec{B} = -\frac{\vec{v} \times \vec{E}}{c} \tag{2.4}$$

We see then that we have an electron with a magnetic moment in a magnetic field for which the spin-orbit interaction Hamiltonian is,

$$H_{SO} = -\hat{\mu}_s \cdot \vec{B} \quad \propto \quad \hat{L} \cdot \hat{S} \tag{2.5}$$

When treated quantum mechanically, this effect leads to the interaction between the spin and angular momentum quantum numbers that splits the different j levels of the atom according to,

$$\Delta E_{SO} = \frac{\beta}{2}\Big(j(j+1) - l(l+1) - s(s+1)\Big) \tag{2.6}$$

with the factor $\beta = Z^4 \frac{\mu_0}{4\pi} g_s \mu_B^2 \frac{1}{n^3 a_0^3 l(l+1/2)(1+1)}$. This additional splitting between the different j levels is called the fine-structure. In Ba^+ the spin-orbit interaction splits the $6P_{1/2}$ and the $6P_{3/2}$ levels by 50 THz as well as the $5D_{3/2}$ and the $5D_{5/2}$ levels by 25 THz.

Next in order would be the atom's hyperfine structure, which emerges from a similar mechanism, through coupling to the nuclear spin. For all of the experiments described in this thesis we used the even isotope $^{138}Ba^{+}$ which has no nuclear spin and thus no hyperfine structure, however, for a description one could look to the thesis of my predecessor, Matt Hoffman [33], where the hyperfine interaction was of foundational importance.

All of these effects, and many of those more subtle features not described, are fundamentally due to electromagnetic interactions between electrons and protons. We have asserted that these interactions give rise to the principle quantum number, n, as well as quantum numbers describing the angular momentum of the atom's state. In addition to these, since the electromagnetic interaction is parity-invariant, there must also be a quantum number describing the parity of the spatial wave functions of the states as well. As it turns out, the parity, π, of a given state is related to the the orbital angular momentum quantum number, l, according to,

$$\pi = (-1)^{l} \tag{2.7}$$

In the context of APNC, we should say that π is only an approximate quantum number. However, since APNC is so small relative to what is studied in this thesis, we will proceed as though parity were an exact symmetry of the ion's eigenstates.

2.1.1 The valence structure of Ba^{+}

The only atomic system we wish to describe is Ba^{+}, and a diagram of its valence structure is given in Fig. (2.1). The levels are labeled in spectroscopic notation with the subscript of each label indicating the total angular momentum, j, of the level. As a preview of what's to come, the five transitions we most often drive are labeled with their nominal wavelength and function in the experiment. In chapter 2 those functions will be explained, and in Sec. (4.4) the light sources will be described. Also labeled are the spontaneous decay lifetimes of the low-lying 5D states (separated by the spin-orbit interaction). These states have exceptionally long lifetimes with $5D_{5/2} \approx 30$ seconds [34] and $5D_{3/2} \approx 80$ seconds [18], a fact that was exploited throughout our work.

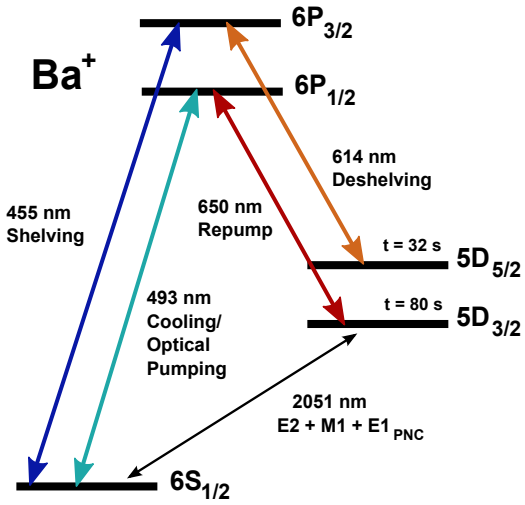

Figure 2.1: A diagram showing the important energy levels, the resonance frequencies between them, and their uses for Ba^+. The separations between the different levels are not to scale.

2.2 Effects of external electro-magnetic fields on atoms internal states

One of the least subtle - though still useful - models of an atom is as an object made up of a tight bundle of positive charges to which are bound a collection of negative charges. That simple picture correctly suggests that the energy in the atom, and thus its internal structure, is affected when the atom is immersed in an external electric or magnetic field. For static fields both types have significant and distinct effects on the atom, although in experiments with trapped ions often the static magnetic field effect, which we call the Zeeman effect, is far more important than the electric field counterpart, known as the Stark effect. For dynamic electromagnetic fields, which are almost always sinusoidally varying in time, the situation is different because atoms can respond to them resonantly or otherwise. In the description given here only the resonant form will be addressed since we will not need the off-resonance interaction. Whether it is the electric, the magnetic, or both parts of the field that the atom chiefly responds to depends on the particular states involved. These kinds of electromagnetic fields are our principle tool in the experiment to be described in this thesis

and are almost without exception sourced from lasers or RF electronics. To describe any of these interactions we need a method and, unsurprisingly to those acquainted with quantum theory, that method is perturbation theory.

2.2.1 The Zeeman effect

Most contemporary experiments on atoms require a well-known and stabilized magnetic field. The characteristic effect of this field - by way of the Zeeman effect - is to remove degeneracies between some atomic states. This is of great practical utility for enabling efficient laser cooling of atoms and the controllable preparation of their internal states. Unfortunately achieving a well-regulated magnetic field can be challenging for two colluding circumstances: stray approximately static magnetic fields are ubiquitous (and, worse still, unpredictable), and they are tricky to divert or cancel. These difficulties are lamentable; the majority of our systematic errors crawl out of the mire of magnetic field noise in our lab. Later on those consequent uncertainties will be explored and estimated, and here the basic formulas for that task will be derived.

Assuming no nuclear spin, the Hamiltonian describing the interaction of an atom with a static and externally applied magnetic field $\left(\vec{B}_{ext}\right)$ is,

$$H_{Zeeman} = -\frac{e}{2m}\big(\underbrace{g_l\hat{L} + g_s\hat{S}}_{\hat{\mu}}\big)\cdot\vec{B}_{ext} \tag{2.8}$$

The bracketed term $\hat{\mu}$ is regarded as the magnetic moment operator of the atom. The factors g_l and g_s are the dimensionless g-factors for the atom's orbital and spin angular momentum, respectively. g_l is simply one, however g_s is a theoretically nuanced quantity and has been measured to better than the part-per-trillion level [35]; for now we need only to know that $g_s \approx 2.002$.

Like the spin-orbit Hamiltonian (H_{SO}), the Zeeman effect removes degeneracies associated with angular momentum quantum numbers in gross atomic structure. For sufficiently large $\vec{B}_{ext}$, when $H_{Zeeman} >> H_{LS}$, the energy shifts on gross structure are well-described by degenerate perturbation theory with the eigenstates of H_{Zeeman}. To get those states we need only to observe that if evaluated in a coordinate system where $\vec{B}_{ext} \,||\, \hat{z}$ then Eq.$\left(2.8\right)$

resolves to $-\frac{e}{2m}\big(g_l\hat{L}_z + g_s\hat{S}_z\big)B_{ext}$. From there we recognize that the eigenstates that diagonalize H_{Zeeman} are $|m_l, m_s\rangle$, and it follows immediately that in the strong-field limit the Zeeman energy shifts are just,

$$E_{Zeeman} = -\mu_B\big(g_l m_l + g_S m_s\big)B_{ext} \quad \big(\text{Strong-field limit}\big) \tag{2.9}$$

The coefficient μ_B leading Eq. (2.9), called the Bohr magneton, is $\frac{e\hbar}{2m}$ or approximately $2\pi \times 1.4\,\hbar$ MHz/Gauss.

In the weak-field limit, when $H_{Zeeman} << H_{LS}$, the Zeeman effect is a perturbation upon the spin-orbit dominated eigenstates $|j, m_j\rangle$. To evaluate $\langle j, m_j|\,\hat{\mu}\,|j, m_j\rangle$ some algebra must be carried out, as is done in [36], whereupon it is found,

$$\langle\hat{\mu}\rangle = \underbrace{\Big[g_l\frac{j(j+1) - s(s+1) + l(l+1)}{2j(j+1)} + g_s\frac{j(j+1) + s(s+1) - l(l+1)}{2j(j+1)}\Big]}_{g_j} m_j \tag{2.10}$$

and that the energy shifts on the $|j, m_j\rangle$ states are,

$$E_{Zeeman} = -\mu_B g_j m_j B_{ext} \qquad \big(\text{Weak-field limit}\big) \tag{2.11}$$

Eqs.(2.9) and (2.11) are the extreme behaviors of the Zeeman effect. To know which if either is quantitatively useful we see whether our atoms fall within one of these limits. The g-factors that we encounter are around one or two so the rough scale of our Zeeman splittings will be $\mu_B B_{ext}$. We employ a magnetic field of a few Gauss and thus we anticipate that $\mathcal{O}\big(E_{Zeeman}\big) \sim 2\pi\hbar \times 5$ MHz. For comparison, the smallest $\hat{L}\cdot\hat{S}$ splitting in our valence structure occurs between the $5D_{3/2}$ and $5D_{3/2}$ manifolds and is about 24 THz [2], placing us well inside of the weak-field limit. Moreover, nowhere in the experiments to be presented is there any need for a precise prediction of the location of our transition. To conclude this section there is one final consideration. What we actually require is a formula describing how the Zeeman effect will shift particular atomic transitions. For that we just take the

[2]This massive mismatch in scale may lead one to over value Eq. (2.11). For most of my time in the group we simultaneously pursued measurements in $^{137}Ba^{+}$, whose hyperfine structure includes splittings between different angular momentum eigenstates on the order of hundreds of megahertz. The details of those experiments are the subject of my predecessor's thesis which, includes a description of the Zeeman effect at second order.

m_j / $m_{j'}$	+1/2		-1/2	
-3/2	-2	-11/5	-1	-1/5
-1/2	-1	-7/5	0	+3/5
+1/2	0	-3/5	+1	+7/5
+3/2	+1	+1/5	+2	+11/5
	Δm	g_{eff}	Δm	g_{eff}

Figure 2.2: A table of g_{eff} for all 2051 nm transitions.

difference between Eq. (2.11) applied to two different states $|j, m_j\rangle$ and $\left|j', m_{j'}\right\rangle$,

$$\Delta E_{j,m_j,\, j',m_{j'}} = -\mu_B \big(g_j m_j - g_{j'} m_{j'}\big) B_{ext} \tag{2.12}$$

The quantity $g_j m_j - g_{j'} m_{j'}$ can be thought of as an effective g-factor (g_{eff}) for a given transition in the weak-field limit. We will only be concerned with g_{eff} for transitions between the $6S_{1/2}$ and $5D_{3/2}$ states.

2.2.2 The Stark effect

Since we experiment with trapped ions it is clear that a stray static electric field will push our atom around; a problem to be sure. The intention of this section is restricted to a very brief description of the effect that field would have on the atom's internal states only. The need for a well regulated and static electric field is less common than for a magnetic field but does arise in some experiments - notably those in search of symmetry-violating effects like some APNC and larger-than-expected EDM searches. Antithetically an unaccounted-for electric field will cause systematic shifts, but these are usually less troublesome than stray magnetic fields since electric fields are not generated on accident nearly as easily and can be blocked by any conducting material. All the same we cannot go forward without some comment of the effect, even if only so that we can justifiably ignore it later on. For this

effect the perturbing Hamiltonian is [36],

$$H_{stark} = -e\vec{E_{ext}} \cdot \hat{z} \tag{2.13}$$

which is the same form as for the energy of a classical electric dipole with charge e immersed in an external electric field $\vec{E}_{ext}$. Following the standard treatment we consider the symmetry of operator for insight. Under a parity transformation $\vec{E}$ is mapped onto itself, whereas the position operator $\hat{z}$ is taken to $-\hat{z}$, so that the interaction Hamiltonian H_{stark} is pseudo-scalar. Recalling that the atomic eigenstates are states of definite parity, we find that at first order the energy shift on any given atomic state $|n, j, m_j\rangle$ must be zero. At higher order, where eigenstates of opposite parity are mixed, the effect does arise, however, not on a scale that is meaningful for the experiments to be presented. As will be discussed in Sec. (5.4.1) we were susceptible to an exponentially decaying static electric field, however data was not recorded till the charge generating the field had dissipated over many decay lifetimes.

2.2.3 Laser driven transitions between atomic energy levels

Oscillating electromagnetic fields, like those from lasers, are able to drive an atom between its states. For a thorough treatment of this phenomena, including a quantized electromagnetic field, we refer the reader to [26]; for our description we begin from the light-atom Hamiltonian,

$$\hat{H} = \frac{1}{2m}\big(\hat{P} - e\hat{A}(r,t)\big)^2 + \hat{V}(r) - \frac{e}{m}\hat{S} \cdot \hat{B}(r,t), \tag{2.14}$$

where $\hat{P}$ is the momentum operator, and $\hat{A}(r,t)$ is the vector potential describing the radiation field, which we take as a plane-wave with frequency ω and wave-vector $\hat{k}$. The potential $\hat{V}(r)$ groups the atomic terms, for example, the electrostatic and the spin-orbit interaction. The field $\hat{B}(r,t)$ is the magnetic field of the laser. The Hamiltonian can be parsed into three parts,

$$\hat{H} = \hat{H}_0 + \hat{H}_{EM} + \hat{H}_I(t) \tag{2.15}$$

The first two pieces are the full many-electron Hamiltonian describing the atom's internal structure and the electromagnetic Hamiltonian, respectively. The third term, $\hat{H}_I(t)$, is the

interaction between the light field and the atom, and is,

$$\hat{H}_I(t) = -\frac{e}{m}\hat{P}\cdot\hat{A}(r,t) - \frac{e}{m}\hat{S}\cdot\hat{B}(r,t) + \frac{e^2}{2m}\hat{A^2}(r,t) \tag{2.16}$$

Because the atomic eigenstates are also states with definite angular momentum it is convenient to expand the $\hat{H}_I(t)$ in terms of electromagnetic multipoles[3], so that,

$$\hat{H}_I = \Big(\hat{H}_{E1} + \hat{H}_{E2} + ...\Big) + \Big(\hat{H}_{M1} + \hat{H}_{M2} + ...\Big) \tag{2.17}$$

where E1, E2, etc. correspond to electric-dipole, -quadrupole, etc. and M1, M2, etc. correspond to magnetic-dipole, -quadrupole, etc. Only three of these terms, $\hat{H}_{E1}$, $\hat{H}_{M1}$, and $\hat{H}_{E2}$, are used for our purposes, which written explicitly are,

$$\hat{H}_{E1} = e\,\hat{r}\cdot\vec{E} \tag{2.18a}$$

$$\hat{H}_{E2} = -\frac{1}{6}\hat{Q}_{i'j'}\frac{\partial E_{i'}}{\partial x_{j'}} \tag{2.18b}$$

$$\hat{H}_{M1} = -\hat{M}\cdot\vec{B}, \tag{2.18c}$$

where the position operator $\hat{r}$ has components $\hat{x}_i$, in terms of which $\hat{Q}_{i'j'}$ is $e\big(3\hat{x}_{i'}\hat{x}_{j'} - \hat{r}^2\delta_{i'j'}\big)$. The magnetic-dipole operator is $\hat{M} = \frac{e}{2mc}\big(\hat{L}+2\hat{S}\big)$ [37]. To see how these multipole interaction Hamiltonians drive transitions we first assume that the system is comprised of only two states, $|1\rangle$ and $|2\rangle$, which are stationary states of $\hat{H}_0$, so that,

$$\begin{gathered}\hat{H}_0\,|1\rangle = E_1\,|1\rangle\,, \quad \hat{H}_0\,|2\rangle = E_2\,|2\rangle\,, \\ \text{with } E_1 < E_2\end{gathered} \tag{2.19}$$

In general, the time evolution of an arbitrary state Ψ is described by the time-dependent Schroedinger equation,

$$i\hbar\frac{\partial}{\partial t}\Psi(r,t) = \hat{H}_I\Psi(r,t) \tag{2.20}$$

which in terms of the stationary states of $\hat{H}_0$ leads to,

$$\Psi(r,t) = c_1(t)e^{-iE_1t/\hbar}\,|1\rangle + c_2(t)e^{-iE_2t/\hbar}\,|2\rangle \tag{2.21}$$

[3]This step takes some justification and algebra, but Eq. (2.17) is the ultimate destination. As suggested at the onset of the discussion, see [26] for the details.

The coefficients $c_1(t)$ and $c_2(t)$ are constrained such that $|c_1(t)|^2+|c_2(t)|^2=1$ at all time. If we define the quantity $\Omega = \langle 1|\,\hat{H}_I\,|2\rangle/\hbar$, called the Rabi frequency, and substitute Eq. (2.21) into Eq. (2.20) we find that the coefficients c_1 and c_2 must obey the coupled differential equations,

$$i\dot{c}_1 = \Omega\cos(\omega t)e^{-i\omega_0}c_2 \tag{2.22}$$

$$i\dot{c}_2 = \Omega^*\cos(\omega t)e^{i\omega_0}c_1 \tag{2.23}$$

Where ω_0 is the resonance frequency between the two levels, defined as $\omega_0 = (E_2 - E_1)/\hbar$. Solving for the population in the excited state, $|c_2|^2$, we find,

$$|c_2|^2 \approx \frac{\Omega^2}{W^2}|\sin^2\big(\frac{Wt}{2}\big)| \tag{2.24}$$

where $\mathrm{W}^2 = \Omega^2 + (\omega-\omega_0)^2$ is called the generalized Rabi frequency. What we find is that when the laser is tuned to the resonance frequency between the two states, so that so that $\omega = \omega_0$, population will cycle between the two states sinusoidally with time at the Rabi frequency Ω. The time that it takes for the atom to be driven from one state into the other is a quantity of particular interest, which is called the π-time, and is related to the Rabi frequency by,

$$\tau_\pi = \frac{\pi}{\Omega} \tag{2.25}$$

For the various experiments to be reported within, π-times ranged from tens of microseconds to tens of milliseconds.

Rabi frequencies are the central observable phenomena of the measurements to be presented in Chapter 5. For any particular transition moment operator, $\hat{\mu}$ - which could be $\hat{E}1$, $\hat{M}1$, $\hat{E}2$, etc. - that moment's contribution to the total Rabi frequency is,

$$\Omega^{(\mu)} = \left\langle n^{'}, j^{'}, m_j^{'}\right|\hat{\mu}\left|n, j, m_j\right\rangle \tag{2.26}$$

By the Wigner-Eckart theorem [27], $\Omega^{(\mu)}$ can be evaluated generically to,

$$\Omega^{(\mu)} = \left\langle n^{'}, j^{'}\right|\left|\hat{\mu}\right|\left|n, j\right\rangle \times \left\langle j, k; m, q\middle| j, k; j^{'}, m^{'}\right\rangle/\sqrt{2j+1} \tag{2.27}$$

The first matrix element, $\left\langle n^{'}, j^{'}\right|\left|\hat{\mu}\right|\left|n, j\right\rangle$, properly called the reduced transition matrix element, are the objects of interest to this thesis. In particular, this thesis describes a

Table 2.1: A table of the selection rules for electric-dipole, electric-quadrupole, and magnetic-dipole transitions.

	$E1$	$M1$	$E2$
Δj	0, ± 1	0, ± 1	0, ± 1, ± 2
Δm_j	0, ± 1	0, ± 1	0, ± 1, ± 2
$\Delta \pi$	$\pm$ 1	0	0

measurement of $M1 = \langle 5, 3/2 | \left| \hat{M}1 \right| | 6, 1/2 \rangle$. The rest of the terms in Eq. (2.27) can be calculated simply from the various quantum numbers. Explicit forms for $\Omega^{(E2)}$ and $\Omega^{(M1)}$ are derived later in Sec. (5.1.2).

Because of the properties of the multipole operators, we know that the Rabi frequency can be non-zero only for states with particular quantum numbers. The conditions governing which states can be connected by a given kind of multipole interaction are called selection rules and are partially summarized in Table (2.1).

Adiabatic rapid passage

Another useful approach to controllably transfer population between states using a laser is adiabatic rapid passage (ARP). The technique exploits the adiabatic theorem [36], which, assuming non-degeneracy, can be stated as [36], a physical system remains in its instantaneous eigenstate if a given perturbation is acting on it slowly enough. Here, the perturbing Hamiltonian is $\hat{H}_I$ of Eq. (2.16) with the adiabatic parameter being the frequency of the laser, ω. The name, "adiabatic rapid passage", references the two competing time scales involved in transferring population from one state to another: the Rabi frequency and the decoherence rate. The sweep rate of the laser frequency must be adiabatic with respect to the Rabi frequency, but, since the process is coherent, it must be rapid with respect to the system's decoherence rate. In theory, the laser frequency would have to be swept from $-\infty$ to $+\infty$, however as a practical matter the laser frequency's detuning need only extend a

few linewidths off the transition resonance. In our apparatus a laser frequency sweep rate between $1 - 10$ MHz/s was typically able to transfer population from the $6S_{1/2}$ to one of the $5D_{3/2}$ states with >90% efficiency.

The advantages offered by ARP over a π-pulse are that this technique is largely insensitive to noise in the laser parameters. In order to perform a π-pulse, the laser frequency must be held constant to within a small fraction of the laser-driven transition width, and the exposure time must be carefully set as well. By contrast, our group has seen that ARP transfer efficiency can be >90% for roughly full order of magnitude of laser frequency sweep rates [38]. The biggest trade-off of using ARP is that the process is by comparison very slow. When we use ARP to drive 2051 nm transitions in Ba^+'s we typically sweep over 200 kHz in 20 ms, compared to performing a π-pulse which could be as fast as 30 μs. More important still for the measurement of M1 is that we have found ARP to be an unreliable technique for determining Ω. It is, however, still a very useful technique, especially when trying to locate the narrow transitions between the $6S_{1/2}$ to either of the 5D state manifolds.

Chapter 3

EXPERIMENTAL TECHNIQUES

3.1 Ion trapping

3.1.1 A trapping potential for charged particles

To trap a single ion we would like to somehow arrive at an electromagnetic potential that confines the ion in all spatial directions. To get there let's investigate a candidate made obvious by our physicist-training, a three-dimensional electrostatic harmonic potential,

$$\Phi\big(x,y,z\big) = \frac{\Phi_0}{2}\big(\alpha x^2 + \beta y^2 + \gamma z^2\big) \tag{3.1}$$

Since this potential is electrostatic, for it to be physically realizable it must satisfy the Laplace equation $\Delta\Phi = 0$ requiring,

$$\alpha + \beta + \gamma = 0 \tag{3.2}$$

Evidently one of these coefficients must be negative[1], so that we could take, for example, $\alpha = \beta = 1$ and $\gamma = -2$ or $\alpha = -\beta = 1$ with $\gamma = 0$. These are partial solutions, in that an ion would be confined harmonically along an axis with a positive coefficient, however it would be repelled to $\pm\infty$ along one with a negative coefficient, and free of influence along the direction of vanishing coefficient. The shortcomings of these specific configurations indicate a generic result of electrostatics called Earnshaw's theorem which can be stated as you can't confine charged objects electrostatically. The preclusion of any stable equilibrium does not generalize to electrodynamic potentials however, and from the advantageous position of knowing the answer we can motivate such a potential from our failed electrostatic ansatz. As noted if $\beta = -1$ then the ion will be accelerated toward $\pm\infty$ along $\hat{y}$. If after some time the potential were to change signs then the ion would be accelerated back toward $y = 0$ but crucially, since the potential is harmonic, with an increasingly greater force until the

[1] We will ignore the trivial null solution of $\alpha = \beta = \gamma = 0$, which is utterly useless.

particle turns around [39]. It follows that if the potential were to oscillate sinusoidally, and the displacements being not too great, that the average force the ion would experience would tend to restore the particle to the $x = y = 0$ equilibrium. Having conceptually found a dynamical way to confine the ion in two "radial" dimensions, an independent harmonic DC voltage could confine the ion electrostatically in the third "axial" dimension. This describes one variety of a class of ion traps called a Paul trap[2]. There are several geometries that achieve the same end, but ultimately all employ a combination of an RF voltage and ground arranged to generate a quadrupole potential with a DC voltage [40]. The case just described can be implemented by four rod electrodes extending normal to the $\hat{x}-\hat{y}$ plane at the corners of a square with two "end-cap" electrodes along their center. The potential created by this configuration near its central axis is given in [41],

$$\Phi_V\big(x,y,t\big) = \frac{V_0}{2}\Big(1+\frac{x^2-y^2}{R_0^2}\Big)\cos\big(\Omega_{RF}t\big) \tag{3.3a}$$

$$\Phi_U\big(x,y,z\big) = \frac{\kappa U_0}{Z_0^2}\Big[z^2-\frac{1}{2}(x^2+y^2)\Big] \tag{3.3b}$$

The parameters V_0 and Ω_{RF} are the RF voltage and drive frequency, respectively, applied to the trap rods. The distance R_0 is that from the rods to the center of the trap. U_0 is the DC voltage applied to the "end-cap" needles, which are separated by $2Z_0$. The factor κ is an additional geometric factor describing those needles. The equation's of motion for an ion acted upon by these potentials are the solutions of the Mathieu equation,

$$\ddot{u}_i + \frac{\Omega_{RF}^2}{4}\big[a_i + 2q_i\cos\big(\Omega_{RF}t\big)\big]u_i = 0 \tag{3.4}$$

after making a change of variables in Eqs. $\big(3.3\big)$ to,

$$\vec{u} = u_x\hat{x} + u_y\hat{y} + u_z\hat{z} \tag{3.5a}$$

$$a_x = a_y = -\frac{1}{2}a_z = -\frac{4\kappa QU_0}{mZ_0^2\Omega_{RF}^2} \tag{3.5b}$$

$$q_x = -q_y = \frac{2QV_0}{mR_0^2\Omega_{RF}^2}, \quad q_z = 0 \tag{3.5c}$$

---

[2]The other variety, called a Penning trap, uses a static magnetic field with a static electric field to confine charged particles to a bound orbit. This approach is used with great success in a number of experiments but is not the technique we employ.

To find an analytic solution for the ion's equations of motion, from which its qualitative behavior can be modeled, we make the approximation that $a_i < q_i^2 << 1$, under which the solution to Eq. (3.4) along the x direction is,

$$x_i(t) = A\cos(\omega_i t + \phi)\big[1 + q_i/2\cos(\Omega_{RF}t)\big] \tag{3.6}$$

The frequency ω_i is related to the trap parameters by,

$$\omega_i = (a_i + q_i^2/2)^{1/2}\,\Omega_{RF}/2 \tag{3.7}$$

A few features stand out upon inspection of our solution. Under our supposition that $a_i < q_i^2 << 1$ we observe that $\Omega_{RF} >> \omega_i$ so that the ion has two distinct well-resolved frequencies in its motional spectrum. Also we observe that the ω_i motion is dominate over the Ω_{RF} motion, which is scaled down by q_i from the ω contribution. These spectrally distinct features are clearly discernible in Fig. (3.1), which plots Eq. (3.7). In that simulation $q_i/A \propto 1/10$ and $\omega_i/\Omega_{RF} = 1/400$, which were chosen simply so that the different behaviors would be clear. The low frequency and large amplitude oscillation is the desired harmonic oscillator motion we sought from our trapping potentials. The frequency of this motion is ω_x and is called the 'secular frequency'. The rapidly oscillating but low amplitude contribution, due to Ω_{RF}, is called micro-motion and is the remnant part of the ion's motion due the trap's RF drive voltage. Micro-motion is an unwanted feature that tended to smear the ion's wave function in the trap [42]. Micro-motion is minimized at the trap center, and to minimize its effect on the ion we apply additional DC voltages to push the ion to the trap center. These voltages are applied on dedicated electrodes on the periphery of our trap rods.

3.1.2 Photo-ionization and loading the trap

In order to perform an experiment on a single trapped ion one needs a method to ionize the neutral atom. Throughout history different methods have been used successfully to singly ionize atoms for experimentation, but one particularly attractive technique is to use light from lasers. The typical ionization energy for the most commonly trapped atoms is roughly 5 - 10 eV, and for barium in particular the number is 5.21 eV [32]. In terms of wavelength

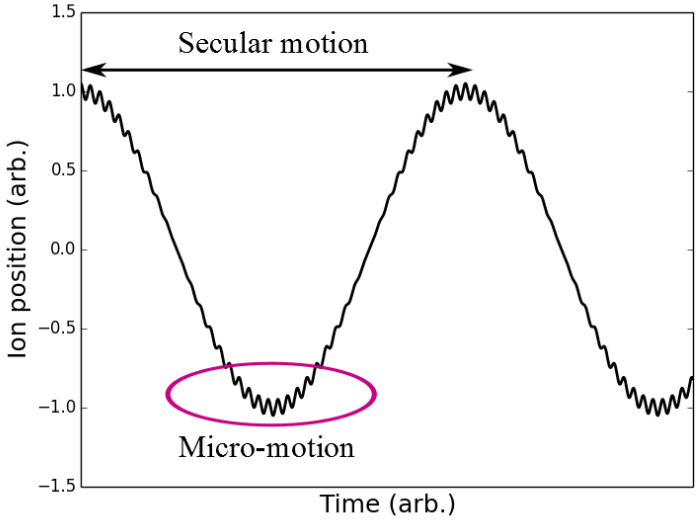

Figure 3.1: A plot of the ion's position over time modeled by the Matthieu equation. The slow, large amplitude is the ion's secular motion. The fast and small amplitude oscillation is the driven motion from the drive RF, known as micro-motion. Here $q_i/A = 1/10$ and $\omega/\Omega_{RF} = 400$.

this translates to a single photon of about 237 nm. Although a single photon could be used to directly ionize atoms it is usually better to use a few lower energy resonant photons to reach the ionization threshold to avoid problems related to the use of high energy photons. These include unintentionally charging surrounding material (by way of the photoelectric effect) and dealing with loss of UV power to absorption by various optics. Beyond avoiding problems, if resonant photons are used for transitions that are sufficiently narrow that isotope shifts can be resolved, then one can also be isotope selective when loading, which is essential for many applications. For barium we follow the scheme described in [43] using the 791 nm transition in the neutral atom. This transition is an inter-combination line between the $6S_0$ singlet ground state and an excited $6P_1$ triplet state, and is inherently narrow [44]. In all experiments presented in this thesis we used ^{138}Ba exclusively, which is the by far the most abundant isotope. The nearest isotopes, 136, 134, and 130, are separated from ^{138}Ba by about 100 MHz, which is far more than the width of the transition itself or than our 791

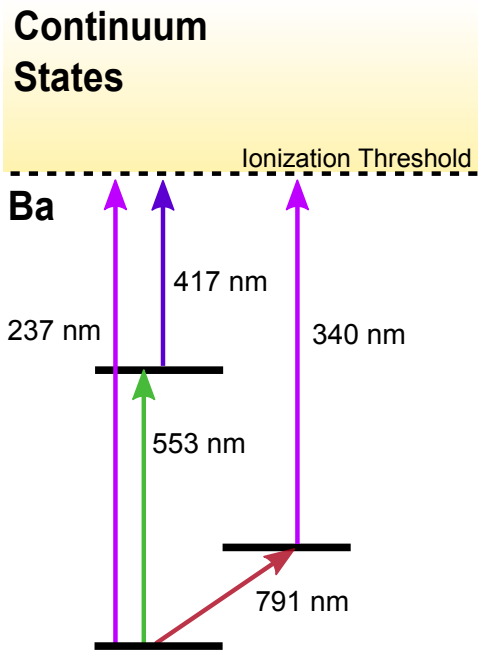

Figure 3.2: A partial energy level diagram for neutral Ba showing the transitions and energy levels that could be used for photo-ionization of the atom.

nm laser. Occasionally, however, a ^{138}Ba would be loaded with a second "dark" partner; dark in the sense that both could not be laser-cooled with the same frequency. For fun we would occasionally tune our cooling lasers up to address the dark parter, which sometimes could be made bright as well.

3.2 Laser cooling

Coherent experiments of the sort we seek to perform require that the ions be cold. Temperature is not something that we naturally ascribe to a single quantum particle, but it is not too great a conceptual leap that we use that language to describe the motional kinetic energy of the ion inside a trap. It was shown in the late 1970s that the special properties of laser light make it an excellent tool for this purpose [45, 46]. Laser cooling of atoms, in its various forms, has become one of the standard technologies of atomic physics laboratories and has enabled such feats as the realization of Bose-Einstein condensation [47, 48], the first degenerate Fermi gas [49], and atom-based frequency standards [50]. Optical cooling

techniques have been pushed to their extreme of cooling a quantum particle to their motional ground state [51, 52, 53]. Those exotic methods require a full quantum mechanical treatment of laser cooling; here we will describe the standard process, semi-classically, called Doppler cooling, and write down the limits of the method. Since photons carry momentum, an atom scattering resonant light will experience a back pressure from the interaction with the light source. In the canonical treatment of Doppler cooling it has been believed that light scattered by spontaneous emission was necessary to carry away the entropy from the cooled atom, and that is the picture we will outline shortly. However, interestingly, recent studies have found and demonstrated that spontaneous emission and the scattering force are not the only means by which the Doppler effect can be leveraged to cool an atomic ensemble [54, 55]. With that caveat, the form of that scattering force, F_{scatt}, is given in [31],

$$F_{scatt} = \frac{\hbar k \Gamma}{2} \frac{s}{1 + s + (\frac{2(\delta + k\nu)}{\Gamma})^2} \tag{3.8}$$

The parameter Γ is the width of the transition, Ω is the Rabi frequency, and the parameter s is the saturation parameter, which is $2\Omega^2/\Gamma^2$. The term $\delta = (\omega - \omega_0)$ is the detuning of the laser from the transition resonance, including a factor $k\nu$ to account for any Doppler shift on the resonance. To proceed, we expand in ν which gives,

$$F_{scatt} \simeq \frac{\hbar k \Gamma}{2} \big(\frac{1}{1 + s + 4\delta^2/\Gamma^2} \big) \times \big(1 - \frac{8 k \nu \delta/\Gamma^2}{1 + s + 4\delta^2/\Gamma^2} \big) \tag{3.9}$$

From which we see that by grouping,

$$z_0 = \frac{1}{m\omega_z^2} \frac{\hbar k \Gamma}{2} \Big(\frac{1}{1 + s + 4\delta^2/\Gamma^2} \Big) \tag{3.10}$$

along with,

$$\alpha = -\frac{4\hbar k^2 s \delta/\Gamma}{(1 + s + 4\delta^2/\Gamma^2)^2}, \tag{3.11}$$

the total force experienced by the ion, including the trapping potential of frequency ω_z, is,

$$F_{total} = -m\omega_z^2 (z - z_0) - \alpha\nu \tag{3.12}$$

What we find then is that we recover the old harmonic oscillator force on the ion, now offset by the radiation pressure from the laser, with an additional damping term linear in ν. The

effect of the damping is to reduce the motional energy of the ion in the trap, however, that cooling does not continue to zero kelvin. Each scattered photon imparts momentum to the ion in a random direction. These kicks set the minimum temperature that can be reached by Doppler cooling, T_D, which has the form,

$$T_D = \frac{\hbar\Gamma}{2k_B} \quad \text{(Doppler cooling limit)} \tag{3.13}$$

The minimum temperature attainable from the radiation pressure felt by the ion is proportional to the scattering transition's width. The factor k_B is the Boltzmann constant. This description of Doppler cooling assumes implicitly a two-state atom, a class to which our atom is not strictly a member. The three-state "Λ-structure" of Ba^+ does complicate the analysis [56], but not any essential features. Using the two-state model, the Doppler cooling limit for of Ba^+ is predicted to be $T_D \approx 500\mu$K. In our lab we have routinely achieved ion temperatures of $T \approx 2$ mK, measured using a characteristic decoherence which is described in detail in [57] and that will be outlined later in Sec. (5.4.4). This non-zero ion temperature does have implications which will be explored in that section.

Doppler cooling of trapped ions has a very important ancillary feature: the scattered photons, which we call the ion's fluorescence, can be collected and imaged. That light is the only signal we get from our ion and is the basis of every spectroscopic measurement we perform. How we interpret the fluorescence to determine the ion's state is the subject of Sec. (3.4) and how it is collected is described in Sec. (4.3).

3.3 Optical pumping

Because of the narrow linewidths of the $6S_{1/2} \leftrightarrow 5D_{3/2}$ transitions, we require a means of controllably populating either $6S_{1/2}(m_J = \pm 1/2)$ state. This can be done optically by clever manipulation of transition selection rules, in a range of techniques called optical pumping [58]. For Ba^+ we optically pump into either ground state using the cooling transitions, exploiting the angular momentum selection rules for electric-dipole transitions. For this two beams are needed: a circularly polarized 493 nm beam (independent of the primary cooling beam) and the 650 nm beam to repump out of the $5D_{3/2}$ states. In a geometry where these beams co-propagate with the ion's quantization axis, the electric-dipole transition selection

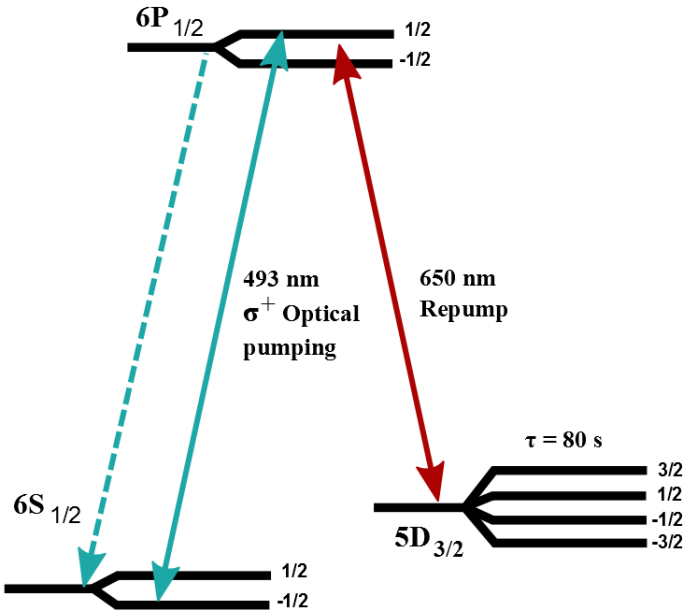

Figure 3.3: A diagram of Ba^+ valence structure including its Zeeman substructure and with the optical pumping transitions indicated. The unidirectional dashed blue line represents spontaneous decay from the excited $6P_{1/2}$ state to either of the $6S_{1/2}(m_J = \pm 1/2)$ states. In the figure the 493 nm beam is shown as having $\sigma^{(+)}$ handedness which continuously drives population out of the $6S_{1/2}(m_J = -1/2)$ till the ion completely occupies the $6S_{1/2}(m_J = +1/2)$ state.

rules require that the absorption of one of these circularly polarized 493 nm photon must change the atom's angular momentum according to,

$$\sigma^{(\pm)} \rightarrow \Delta J = \pm 1 \tag{3.14}$$

where $\sigma^{(\pm)}$ corresponds to the handedness of the 493 nm beam with respect to the quantization axis. By choosing a 493 nm polarization handedness we can selectively drive one of the ground state populations to the excited $6P_{1/2}$ state, while leaving any population in the other ground state unperturbed. The consequence is that the atomic population rapidly accumulates in the ground state that is not excited by the 493 nm beam. The fidelity of this process depends most critically on two experimental considerations: the purity of the 493 nm beam polarization and having a sufficiently well-defined quantization axis. The 493 nm beam inevitably will have some ellipticity, wherein both $\sigma^{(\pm)}$ handednesses are present

and compete with each other. Alignment of the optical pumping beams to the ion's quantization axis can also reduce fidelity, however pointing and polarization can be tweaked easily enough to maximize the optical pumping efficiency. The second problem, that of a weakly defined quantization axis, occurs when the applied magnetic field is low enough that the laser field competes to define the quantization axis [59]. This occurs at low strength applied magnetic fields, lower than those used by the experiments to be described herein. In our apparatus optical pumping efficiencies of greater than 90% were regularly obtained.

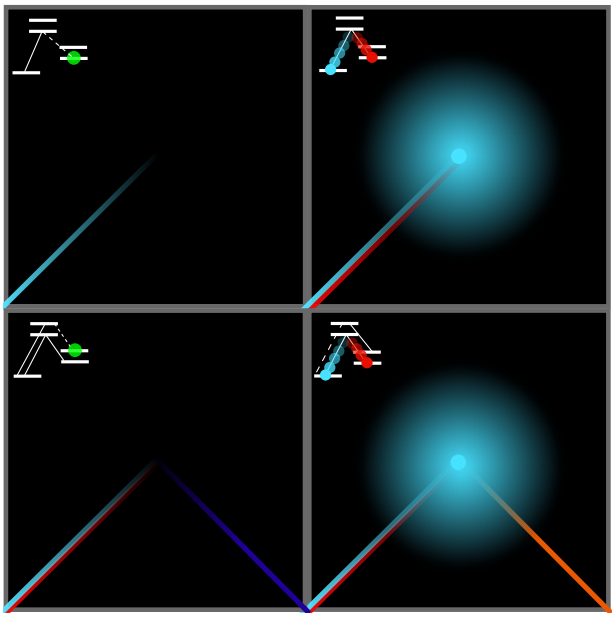

Figure 3.4: A visual summary of shelving and deshelving. Clockwise: An ion addressed only by 493 nm will be pumped to $5D_{3/2}$; cycling between 493 nm and 650 nm transitions the ion will fluoresce; by adding 455 nm radiation the ion is pumped into the $5D_{5/2}$ and the ion will no longer fluoresce since it has been removed from the cooling cycle; addressing the ion with the 614 nm laser will return the ion to the cooling cycle and florescence will resume.

3.4 State detection by electron shelving

Electron shelving, or alternatively, quantum jump spectroscopy, describes the signal that we measured and then interpreted in every experiment we performed. It is a method for directly determining what state the ion was in and was first demonstrated with a single trapped barium ion in 1986 at the University of Washington [60]. The description that is about to be given is easier to follow if Fig. (2.1) is close at hand.

As we saw previously, while being laser-cooled the ion will scatter a large quantity of 493 nm and 650 nm photons, which can be collected and imaged. In our setup we collected the 493 nm light only. While that light is seen it must be that the atom is among the $6S_{1/2}$ and $5D_{3/2}$ states since no other states are connected by those beams. The question we seek to answer is, which of those states was the ion in? Imagine that the ion occupies

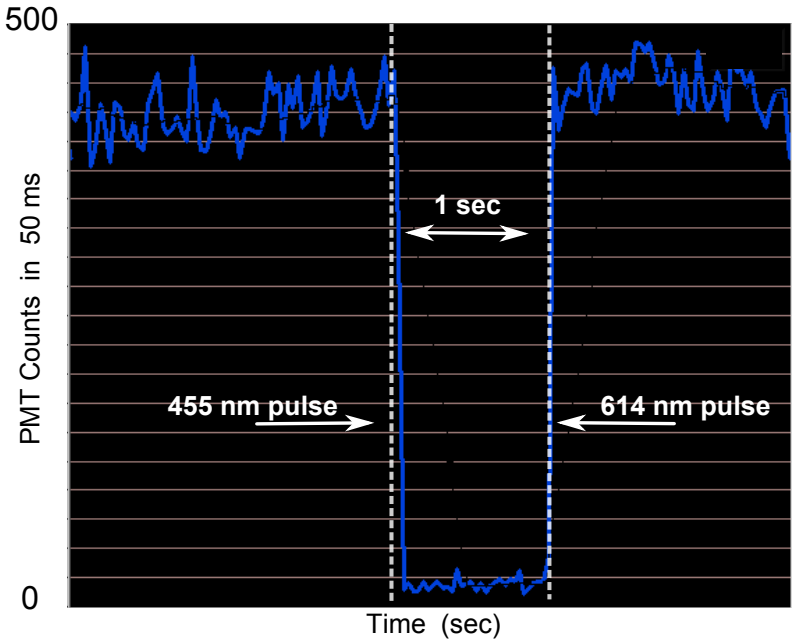

Figure 3.5: A plot of ion florescence collected from our apparatus while the cooling lasers were applied to a single ion. The blue line tracks photon counts collected per 50 ms. The higher average count rate level was due to 493 nm light scattered by the ion from the cooling laser. At the time indicated on the plot a 455 nm pulse was delivered to the ion, shelving it in the $5D_{5/2}$ and resulting in complete extinction of the ion florescence. After a pulse of 614 nm light the ion was returned to the cooling cycle and the florescence returned.

one of the $6S_{1/2}$ states and we have another laser that can directly drive the ion from there to $5D_{5/2}$. If we drive that transition and reapply the cooling lasers then we would observe no ion florescence because the ion was removed from the cooling cycle. An ion in such a circumstance is said to be "shelved". The $5D_{5/2}$ state is metastable with a lifetime of 32 seconds, which gives the experimenter plenty of time to discriminate between the ion fluorescing or not. This is the binary signal (a bright or dark ion) from which the ion's state can be inferred. A fluorescing ion would indicate the ion started among the $5D_{3/2}$ states while a dark ion would indicate that it was shelved, implying it started among the $6S_{1/2}$ states.

In our lab shelving was achieved indirectly by means of the $6S_{1/2} \leftrightarrow 6P_{3/2}$ transition, which we drove with a laser at 455 nm. This method of shelving has the advantages that one need not worry which $6S_{1/2}$ state is occupied (the transition is broad) and it is particularly easy to find (it is a very strong transition). The disadvantages are that the approach is not state selective (some experiments may need that), that the method requires a second laser at 614 nm, and that some contrast is lost to the probability that the ion decays to the $5D_{3/2}$ state from the $6P_{3/2}$ state. Though greater in number, the disadvantages are less important for our needs. From the branching ratios for spontaneous decay from the $6P_{3/2}$ we know the ion could become shelved at best 89% of the time for a sufficiently long 455 nm pulse [61]. That 9% loss of contrast was not a significant factor in our experiments. In principle it required that we collect more data than if we were to have driven the $6S_{1/2} \leftrightarrow 5D_{5/2}$ transition directly by means of the 1762 nm transitions (not explicitly labeled in Fig. (2.1)), but in that alternative scenario a π-time or ARP sweep rate would have had to be calibrated and maintained, and those extra complications (not to mention we did not have easy access to that laser) were not worth the modest loss of contrast for us. The second laser at 614 nm was needed to pump the ion back into the cooling cycle (to "deshelve" it) after the ion was shelved so that the next iteration of an experiment could be undertaken in a reasonable amount of time. The need for a separate laser to depopulate the shelved states was hardly any inconvenience, as that laser was among our most stable, and the transition was strong enough that it needed only minimal tuning day-to-day. In our setup both the shelving and deshelving pulses were 10 ms long, which was limited by other hardware in their beam lines. The important details of those lasers and other relevant systems are given in the subsequent chapter on the Ba^+ apparatus.

In our apparatus a maximally bright single ion would produce between 10,000 and 12,000 photon counts per second on our PMT on a background count rate of about 200 counts per second. This high signal-to-noise is apparent in Fig. (3.5) which demonstrates shelving and deshelving in our apparatus. There one finds actual photon counts (per 50 ms) from a trapped ion held by our apparatus over a several seconds. The cooling lasers were left on continuously, and the higher average count rate is due to the florescence from continuously laser cooling the ion. The sharp drop in photon counts was due to the ion being shelved to

the $5D_{5/2}$ states by a 10 ms pulse from the 455 nm laser. About one second later (I just counted that in my head) a 10 ms pulse of 614 nm light was delivered to return the ion to the cooling cycle. In all actual experiments described in this thesis a 10 ms integration time was used to discriminate between the bright and dark levels.

3.4.1 Pulse sequences for driving 2051 nm transitions

We use electron shelving in the same basic pulse sequence to both locate the 2051 nm resonance frequencies and to measure the Rabi frequency at those resonances.

1. Laser cool the ion with the 493 nm and 650 nm beams for 50 ms.
2. Optically pump to either $6S_{1/2}(m = +1/2)$ or $6S_{1/2}(m = -1/2)$ for 20 ms.
3. Attempt to drive a 2051 nm transition; variable duration and frequency depending on the application.
4. Deliver shelving pulse for 10 ms.
5. Reapply the cooling lasers for 10 ms and collect any florescence.
   (a) If the ion is bright then record result and return to step (1).
   (b) If the ion is dark then record result, apply a deshelving pulse of 10 ms, and then return to step (1).

This pulse sequence would be repeated between 50 and 100 times depending on the statistical uncertainty desired, which yielded the average probability that the ion was found to be dark P_D. The statistical uncertainty in P_D was calculated from the standard expected error for a binomial distribution. The intention of the scan determined exactly what happened in step (3) but generically P_D had the form,

$$P_D = P_{sh}\big(1 - P_{op} \times P_{2051}\big) \tag{3.15}$$

The first probability P_{sh} is the shelving efficiency. Both the shelving and deshelving efficiencies would be checked at the onset of any data collection day, and once set these lasers rarely needed additional tuning, particularly the 455 nm laser. P_{sh} was a fit parameter for both frequency scan and Rabi frequency measurements, so it was monitored by default throughout data collection also. The optical pumping efficiency P_{op} described how well we initially prepared the ion's state in step (2). It was also a fit parameter in the experiments and was typically around 90%. P_{2051} was the probability of successfully driving the 2051 nm transition in step (3). To find the resonance frequency the 2051 nm pulse duration was fixed to the transition's π-time and P_D would be measured over a range of frequencies to

map out the resonance. To find the Rabi frequency the 2051 nm frequency was set to the resonance's center and the pulse duration was varied over a range wide enough to observe a few Rabi oscillations. Since finding the resonance center frequency or the Rabi frequency required knowledge of the other we would sometimes have to iterate between the two to hone in on either. Frequency scans were performed "bin-by-bin" so that the laser frequency was fixed and the procedure repeated until the full statistics for that bin were accumulated before moving onto the next frequency bin. Rabi flop scans were typically performed by stepping the 2051 nm exposure time through the full range upon each iteration. The reason for that was that if the 2051 nm transition frequency was slowly drifting then a bin-by-bin procedure would imitate decoherence, whereas looping over the full time scale would lead to an overall loss of contrast which was an additional way to diagnose the problem.

In Fig. (3.6) there are three example frequency scans performed with 2051 nm exposure times of 100 μs, 300 μs, and 450 μs, for a configuration where the π-time was about 100 μs and the linewidth was 6 kHz[3]. Throughout our experiments it was important to consider the linewidths of the laser-driven transitions, by which we mean the full width at half max of the resonance when driven by a π-pulse. In our work the linewidths of the 2051 nm transitions ranged from 30 kHz down to 60 Hz, but were separated by about 3 MHz. This relatively large spacing made it convenient to have a means to cut down the frequency space within which a particular transition was located. For that purpose we used adiabatic rapid passage in place of π-pulses to drive the transitions. In an ARP scan the same procedure given above was used except that in step (3) the 2051 nm was swept over a some frequency range at a rate appropriate to drive the transitions. An example of two long range ARP scans showing all eight 2051 nm transitions is shown in Fig. (3.7). In those scans each bin occupied a 400 kHz frequency window that was swept over 20 ms, which were typical values that we used. The data binned in orange corresponded to optically pumping to the $6S(m_j = -1/2)$ and in blue to $6S(m_j = +1/2)$. The numbers hovering above the various features indicate Δm for the transition contained within. The detuning against which the spectra were plotted were with respect to the 2051 nm optical reference cavity.

[3]As an aside, the width of the driven transition is closely related to the Rabi frequency, however it was not a reliable enough quantity to infer the Rabi frequency from.

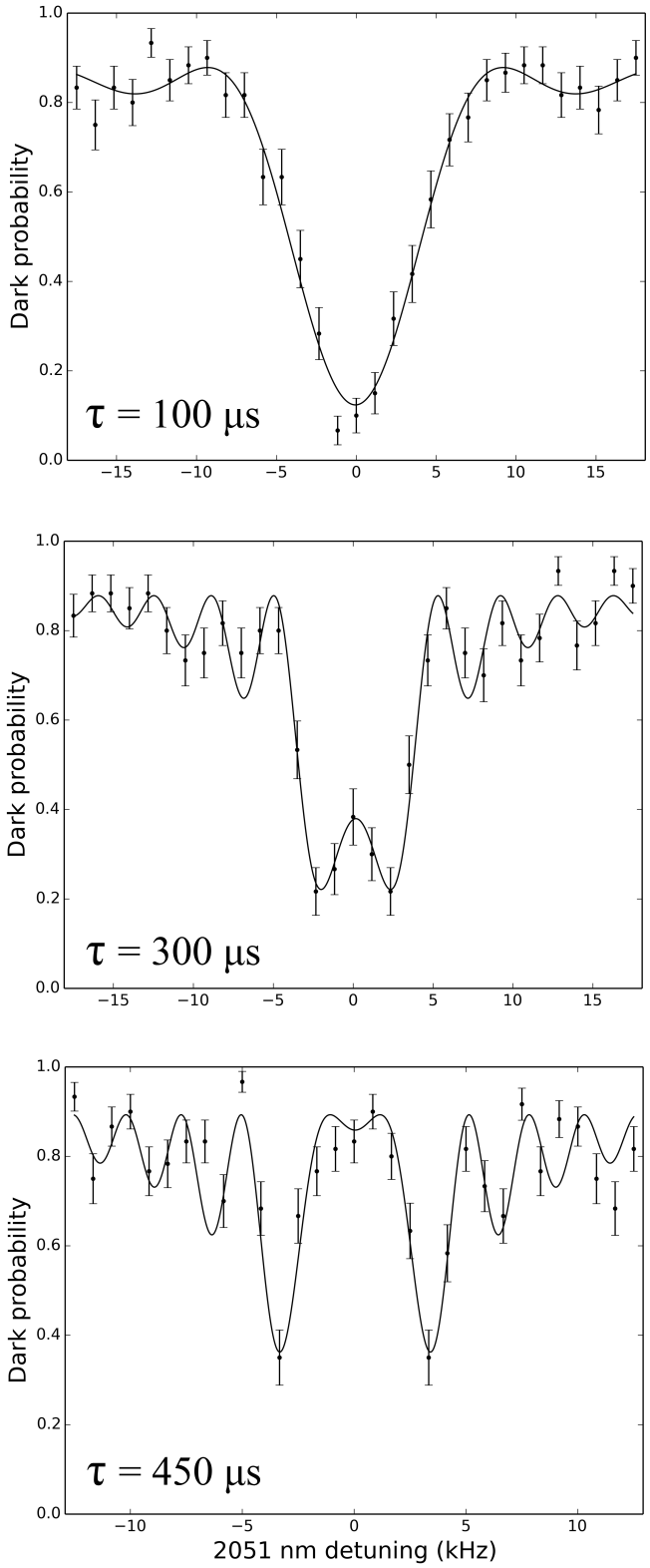

Figure 3.6: Three examples of frequency scans with the 2051 nm exposure time set to 100 μs, 300 μs, and 450 μs for a configuration where the π-time was $\sim$100 μs.

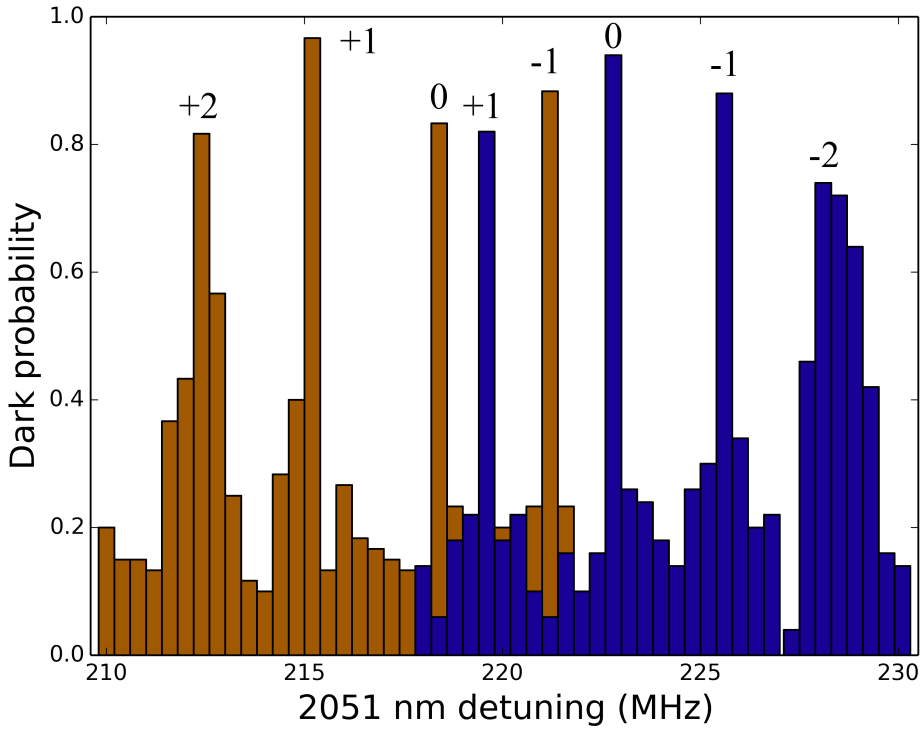

Figure 3.7: A plot of two ARP scans that identify all eight 2051 nm transitions. Each bin is 400 kHz wide, corresponding to the width of the ARP sweep. For the orange scan we optically pumped to the 6S($m_j = -1/2$) state and for the blue to the 6S($m_j = 1/2$) state. From left to right the tall orange bins correspond to $\Delta m = +2$, +1, 0, -1, the blue to $\Delta m =$ +1, 0, -1, -2.

3.4.2 Pulse sequence for rf spectroscopy

Occasionally it was insightful to perform spectroscopy on the $6S_{1/2}(m = 1/2) \leftrightarrow 6S_{1/2}(m = -1/2)$ transition. Such a measurement is called a ground state spin-flip, since that is the only degree of freedom that is changed in the transition. The energy difference between the levels is determined (by way of the Zeeman effect) by our static applied magnetic field at a sensitivity of ≈ 2.8 MHz/Gauss. In our experiments the applied magnetic field was $\approx$ 2.6 Gauss, which resulted in a ground state spin-flip resonance frequency of 7.4 MHz. To perform the spectroscopy we used the 2051 nm laser to discriminate between the two ground states. After optically pumping into one of the ground states and attempting the ground state spin-flip, the 2051 nm laser would be used to pump one of the $6S_{1/2}(m = \pm 1/2)$ states to the $5D_{3/2}$ manifold, and the other would be shelved with the 455 nm laser. Then the cooling lasers were applied to determine the success of the spin-flip attempt. For these experiments the 2051 nm transition would be driven with an ARP sweep to ensure robust pumping efficiency (by whichever state chosen that day) to the $5D_{3/2}$ level. By using ARP the oscillation in the dark ion probability, from which the spin-flip Rabi oscillation is obtained, is nearly insensitive to decoherence effects from the 2051 nm laser itself, and more over, the low recoil of the RF photon makes the process virtually immune to decoherence from the ion's non-zero temperature[4]. Since the ground state effective g-factor is somewhat large (≈ 2) for the transition though, it is an excellent place to study the magnetic field stability and decoherence. Toward the end of the thesis we will use these facts to estimate the expected contribution magnetic field noise makes to the decoherence in our optical spectroscopies.

[4]Ion temperature will be discussed toward the end of the thesis.

The pulse sequence is very similar to that used for 2051 nm spectroscopy:

1. Laser cool the ion with the 493 nm and 650 nm beams for 50 ms.
2. Optically pump to either $6S_{1/2}(m = +1/2)$ or $6S_{1/2}(m = -1/2)$ for 20 ms.
3. Attempt to drive the ground state spin-flip; variable duration and frequency depending on the application.
4. Pump one of the ground states to the $5D_{3/2}$ states with a 2051 nm ARP sweep.
5. Deliver shelving pulse for 10 ms.
6. Reapply the cooling lasers for 10 ms and collect any florescence.

    (a) If the ion is bright then record result and return to step (1).
    (b) If the ion is dark then record result, apply a deshelving pulse of 10 ms, and then return to step (1).

Chapter 4

THE BA$^+$ APPARATUS

Reminds me of that fella back home who fell off a ten-story building. As he was falling, people on each floor kept hearing him say, "So far, so good."

- Vin, The Magnificent Seven

Working in our lab one often feels like a fisherman at war against the sea. The battlegrounds and sinking vessels of our scientific campaigns are charted here. We will cover the essential equipment, which was nearly all either part of the trapping apparatus or of an optical network. These systems and their complement of ancillary devices were without exception conceived of, designed, built, broken, serviced, salvaged, repaired, or destroyed thoroughly by myself or a (relatively) recent predecessor. Some aspects of this chapter will be redundant with other recent theses, others are new, but all of the content herein is an equal obligation to present. Only with a description of this rickety apparatus can we navigate out from the woods of theory to the seas of experimentation - and have some bearing when we arrive.

4.1 Our trap

Our ion trap was built by former graduate student Gang "Rick" Shu [62]. In its original implementation the trap system included an integrated mirror to increase the amount of ion fluorescence that could be collected. It was a linear Paul trap of the type described in Sec. (3.1.1). We held our end-cap needles to 25 V, which resulted in a 440 kHz axial trapping frequency. The trap's (quadrupole) RF rods carried between 1 W and 2 W of RF power, depending on whatever prognostications the lab oracles conferred, at about 12 MHz. In that range our radial trap frequencies varied but were roughly hundreds of kilohertz and close to one megahertz. These frequencies were on various occasions resolved in the 2051 nm transition spectrum and confirmed in that way.

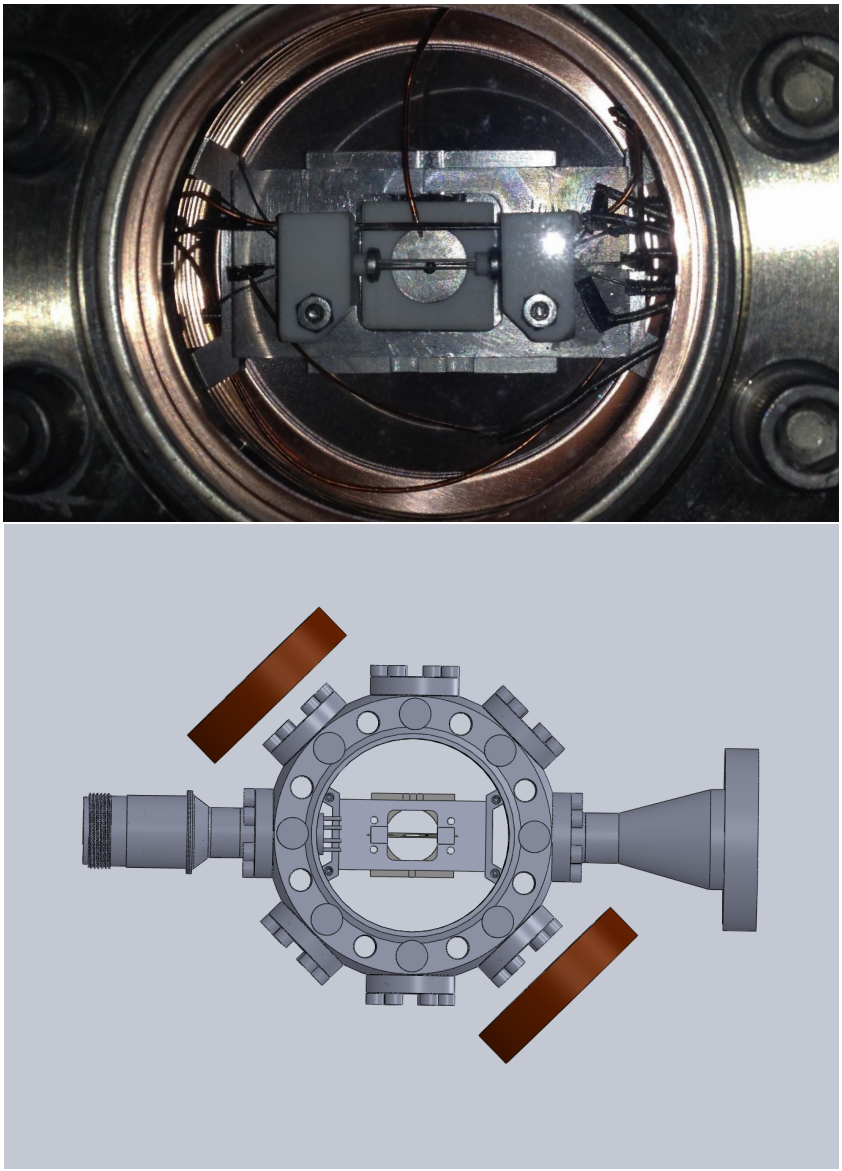

Figure 4.1: The upper image is a photograph of our trap inside the vacuum system. The trap was housed inside a Kimball Physics, Inc. 6 inch spherical octagon, whose pressure was maintained by a 20 L/s ion pump (not shown). The lower drawing shows our ion trap inside the spherical octagon and the coils we used to generate the magnetic field. The CAD model was created by Matt Hoffman.

During a vacuum system rebuild undertaken in 2013 we included additional electrodes for micromotion compensation and to perform RF spectroscopy. These, along with the rest of the trap structure, are barely visible in Fig. (4.1). The new electrodes were housed in Macor® fixtures. A disk-shaped electrode set below the trap provided vertical micro-motion compensation that was held to $\sim$ 60 V, which was determined experimentally. The small aperture bored through the center of disk allowed neutral barium flux from the oven to reach the trapping region. The disk was fit snugly into a Macor® housing that occupied the same space that the collection mirror did originally [62]. The assembly was held in place by set screws on two sides (top and bottom in the figure) that were partially stripped of thread to prevent virtual leaks. The RF spectroscopy and horizontal micro-motion electrodes run parallel to the trap axis. The horizontal micro-motion rod voltage needed to be optimized daily and varied between 300 V and 500 V.

4.2 Vacuum system

The trap was housed inside a Kimball Physics, Inc. 6 inch spherical octagon as drawn in Fig. (4.1). The pressure inside of the chamber was monitored by an ion gauge that reported our pressure to be $\sim 3 \times 10^{-10}$ Torr which was maintained by a 20 L/s ion pump. Our vacuum system had a known (slow) leak that would bring the pressure up to $\sim 6 \times 10^{-10}$ Torr over about two weeks. The leak has persisted for over a year and our best speculation was that was due to damage incurred by the all-metal bankable valve used to seal the chamber during our last trap rebuild in 2013. In addition to the ion pump we had a titanium sublimation pump as well, which was flashed about weekly, driven at 40 A for 90 seconds, to maintain the pressure to $\sim 3 \times 10^{-10}$ Torr. This was not ideal, but it was functional. Our somewhat high pressure allowed us to investigate collisional quenching effects affecting the lifetime of the $5D_{5/2}$ state, which informed our group's study on the spontaneous decay branching ratio from that state [34].

Figure 4.2: A photograph taken from our EMCCD camera of the collected fluorescence from a single trapped barium ion in our ion trap.

4.3 Fluorescence collection optics

Fluorescence from a laser-cooled ion was collected through a vacuum view port from above our vacuum system. About 30 mm above the ion trap light was collected by a long working distance Mitutoyo 10x microscope objective. This light was spatially filtered through a pin hole and passed through a custom 493 nm narrow band interference filter to filter background light. The remaining light was focused onto either our Hamamatsu PMT or onto our Andor iXom+ EMCCD camera, which were selected between with a motorized flipper mirror. In our setup up a maximally bright single ion typically would produce between 10,000 to 12,000 counts per second on the PMT on top of a background count rate of about 200 counts per second. With the fluorescence directed to the EMCCD camera we were able to image the ion, an example photograph of which is shown in Fig. (4.2). Beyond the inspired beauty of the photograph, imaging the ion fluorescence on the EMCCD camera was an indispensable diagnostic tool for tuning the laser and trap parameters for the experiments to be described.

4.4 The Ba^+ lasers

4.4.1 Photo-ionization: 791 nm and 337 nm

791 nm laser "system"

The 791 nm laser we used was shared between five different labs. The laser itself was a home built ECDL, using the same standard aluminum-bronze design that will be described in the 455 nm laser section, with the geometry slightly varied to accommodate the different diffraction angle of the 791 nm light. The laser was referenced to a low finesse optical cavity using a side-of-the-fringe lock. Details of the laser, cavity and locking circuit are in [63]. It was housed and principally maintained by our group's Remote Entanglement lab, where it was fiber coupled and delivered down the hall to our lab space. From the fiber coupler the 791 nm beam was transmitted through a dichroic mirror and combined with the 337 nm beam. Together these two were steered toward the trap with a pair of mirrors, all of which can be seen in Fig. (4.3).

337 nm laser "system"

There is very little to say about the 337 nm light source that we used for photo-ionization because it required none of the grooming that the other beams do to be useful. The laser itself was a Laser Science inc. VSL-337-NDS, which is a nitrogen gas laser. To ionize a barium atom excited along its 791 nm transition a second photon of at least 340 nm ($\sim$ 3.6 eV) is needed, which is just slightly less energy than the photons produced by this laser carry. To control our loading rate we pulsed the N2 laser. Following the laser itself those pulses were combined with the 791 nm beam and focused through the trap. That's it. When all other parts of the loading apparatus were well-tuned loading of a single ion was typically achieved in about one to two minutes while pulsing the N2 laser at 2 Hz.

The 337 nm photons did add one complication, however. Barium vapor tends to deposit onto the various metal surfaces in the trap, and the work function for barium is only 2.5 eV [64]. We did attempt to focus the 337 nm beam at least well enough that it would not

hit trap structure directly, but, loading this way still generated patches of electric charge near the ion. From experience we knew that at least two time scales were present in the dissipation of these patch potentials. Anecdotally the slower scale is something on the order of days, but the faster was measured to be ∼26 minutes. A discussion of that experiment and its implications is forthcoming, but the point will be that little spectroscopy could be undertaken for a couple of hours after loading an ion. Luckily, our trap held atoms pretty well, and there was always something else to do for those couple of hours.

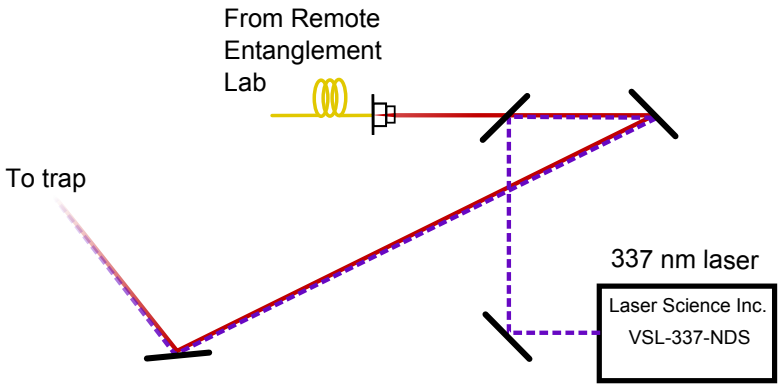

Figure 4.3: A schematic of the combined 337 nm and 791 nm beam lines

4.4.2 Shelving and Deshelving: 455 nm and 614/1228 nm

455 nm laser system

Building the 455 nm laser was not just my first project for this group, but also my first project as an experimentalist. The need for this laser preceded me by many years, and the story of its realization is worth documenting briefly for whatever moral it may have. At the time I joined with the group, we drove the $6S_{1/2} \leftrightarrow 6P_{3/2}$ transition with a 1 Watt LED that we attempted to filter down and focus through the trap. With that old setup the fastest I saw us able to shelve was 500 ms, and this made our experimental repetition rate cripplingly slow. Before my arrival a laser head had been machined for a 910 nm laser to then be frequency doubled to 455 nm, but the student responsible for that project left,

and the project was abandoned. After my arrival that laser head was commandeered by the MUSIQC collaboration where it was successfully employed as a 450 nm laser[1]. As history had it, that reallocation of capital was very fortunate for us. Laser diodes at 455 nm (at room temperature) are, to my knowledge, never made intentionally. When these do appear on the market from a vendor capable of a proper characterization, their rarity demands a high price. At the same time that I began to machine a new laser head, intended to be a 910 nm laser, MUSIQC bought a handful of inexpensive and untested 450 nm laser diodes from Ebay. Some were at 450 nm, one was red, and one was exactly where we needed it at 455 nm. That diode became our light source for shelving.

Generally the spectral widths of inexpensive semiconductor laser diodes are too broad to be immediately useful for atomic physics applications like laser cooling, which require linewidths on the order of megahertz or less. Moreover, the ability to fine-tune the laser's frequency, and the potential to stabilize that frequency, are invariably necessary. An elegant solution to satisfy all of these requirements is to provide wavelength-selective feedback to the laser diode itself using the so-called Littrow configuration. The laser diode and the wavelength selective element, usually a diffraction grating, form an optical cavity external to the laser diode itself, and so this kind of laser is known as an external cavity diode laser (ECDL). Five of the light sources that we employed were of this kind, and in the case of the 455 nm laser the external cavity system was home built. We used a standard design suitable for both atomic physics research and in-house machining [65]. The laser head was constructed from aluminum bronze, which is a hard alloy that is resistant to fatigue. The hardness of the material makes carbide cutting tools favorable to high speed steel. The diffraction grating was a $1/2 \times 1/2$ inch blazed grating from Edmund Optics. Coarse tuning of the external cavity is allowed in the design by two 1/4 - 100 adjuster screws. The first controls the vertical tilt of the diffraction grating by pushing apart the two base plates at the far end from the diode. This dimension has no fine adjustment mechanism. The horizontal tilt of the grating is handled by a second screw behind the cantilevered flexor arm to which the grating is mounted. Fine tuning in the horizontal is performed by a low-

[1] 450 nm drives a weak transition in neutral barium that is useful for photo-ionization.

voltage piezo stack behind the grating. The piezo was driven by a standard single axis piezo driver from Thorlabs[2]. In practice, for all of our home-built ECDL systems, these allowed degrees of freedom are not quite enough to align the external cavity for lasing at the desired wavelength. Luckily there are more options for the bold. By machining the laser diode housing block and grating arm fixture with loose clearance holes, the diode and grating gain many degrees of play. We found this useful in many of our home built lasers because of the ease with which the laser heads can be modified to accommodate a new wavelength (the 450 nm laser, for example). The laser head sits upon a thermoelectric peltier heater/cooler which was controlled by an MPT-5000 from Wavelength Electronics to stabilize the diode's temperature.

Our Ebay-special diode was an Osram PL-450B. It had its center frequency roughly at 455 nm at room temperature with a spectral width of a 2 nm (according the spec sheet). The spatial structure of the collimated beam was decidedly not a pure Gaussian and appeared to include some faint vertical nodal lines reminiscent of the (2,0) Hermite-Gauss mode. This diode had a "messy" output and a stronger tendency to scatter (a non-trivial amount of) light than any of our other beams. The diode was driven by a Thorlab's LDC 205 C benchtop laser diode controller. We found its free running threshold current to be 32.0 mA, which was reduced to 24 mA when the external cavity was aligned. We lacked the ability to measure the resulting reduction of the linewidth, but based on the dimensions of the external cavity we suspected that the spectral width of the laser in single-mode operation was $\mathcal{O}$(1 MHz). The external cavity of our 455 nm laser was about 1 inch, giving the device an expected free spectral range (FSR) of $\sim$6 GHz. What we saw instead was more complicated. The outer glass window of the diode was not AR coated, meaning that rather than having one external cavity between the grating and semiconductor, we observed a more intricate spectrum that we attributed to reflections off of the outer glass surfaces. We observed single-mode behavior only for driving currents below 42 mA; at any higher than that the spectrum became decisively multi-mode. While operating single-mode we were able to achieve a mode-hop free tuning range in excess of 2 GHz by fine-tuning the piezo. Also

[2]Generally low bandwidth feedback to the piezo is used to stabilize the laser's frequency. In this particular system we found that to be unnecessary. A full discussion follows.

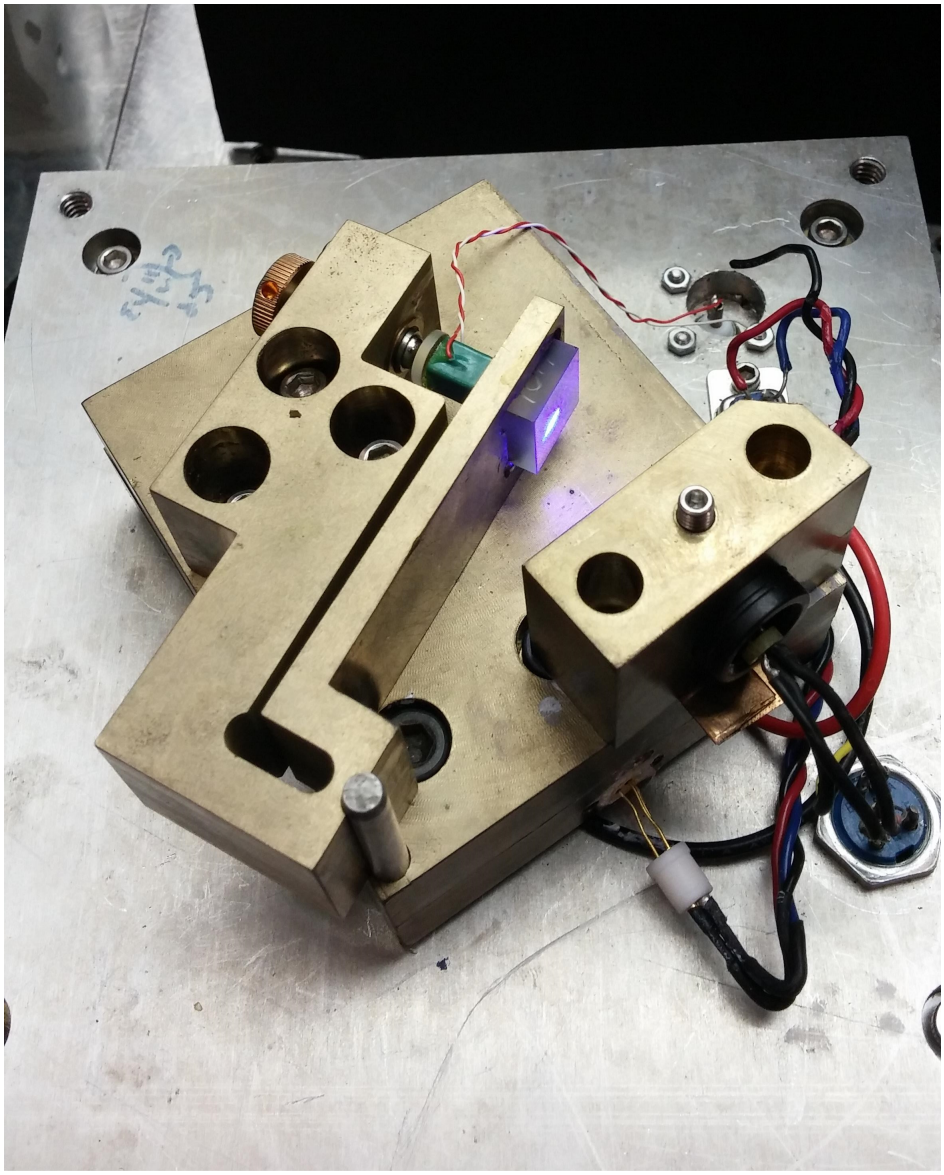

Figure 4.4: A photograph of the 455 nm laser head.

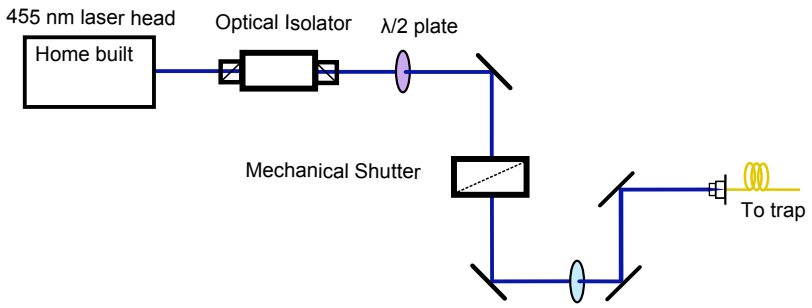

Figure 4.5: Schematic of the 455 nm beam line.

while in single-mode operation, we were able to mode-match and lock the laser to a 2 GHz FSR reference cavity with a finesse of a few hundred. However, because of misinformation from our wave meter, we were unable to find the atomic transition under these conditions[3]. Instead, we drove the diode strongly (typically around 80 mA) and used the diode current to find a multi-mode structure with which the transition could be driven. The correct current setting was heralded by a characteristic telegraph signal in the ion's florescence seen while the cooling lasers and the deshelving laser were also on the ion. This shotgun-ish approach to shelving was very successful. It eliminated any need for electronic feedback circuitry and frequency reference, which greatly simplified its maintenance and setup. The diode current from which the transition could be driven was surprisingly stable, requiring adjustment only a few times over three years. With this multi-mode implementation, and testing with 500 trials, we were routinely able to shelve the ion 100% of the time with a 10 ms exposure time and $\sim$20 μW of power focused toward the ion[4].

The beam line for the 455 nm laser was among the simplest of our optical networks. It is represented schematically in Fig. (4.5). Following the laser head the beam passed through an optical isolator and half wave plate. Then it was redirected through a mechan-

[3]It turned out that our wave meter's readings became increasingly offset as the wavelength tends toward UV. We had this realization after we abandoned single-mode operation of the laser.

[4]This test was done by exposing the atom to 455 nm and 650 nm light simultaneously, allowing us to beat the shelving efficiency limit of 87% imposed by the excited state's branching ratio.

ical shutter, onto a focusing lens, and coupled into an optical fiber for delivery to the ion. Because of the strength of the 455 nm transition a mechanical shutter was chosen to ensure no light unintentionally leaked to the ion. The shutter took 8 ms to open, which was the limiting time scale for the duration of 455 nm pulses we could deliver to the ion. The fiber coupling efficiency was horrendous at only 20%. We attributed this chiefly to the beam's unusual spatial structure and secondarily to our lack of will for improvement. With the 40 - 50 μW delivered through the fiber we were already able to shelve the ion faster than we could operate the mechanical shutter. Not pictured in Fig. (4.5) is the final focusing lens and view port following the output fiber coupler. Accounting for losses at these elements we estimated that the total 455 nm power in the trap was around 20 μW, which, as noted already, was more than enough.

One final comment about the 455 nm laser is notable, particularly for future users. The photon energy for a single 455 nm photon is 2.7 eV, which is just barely larger than the barium work function. That suggests that, like the 337 nm laser, the 455 nm laser could also induce patch charges in the trap. We have not observed evidence of this effect from the 455 nm laser when employed as described above, but its propensity for scattering light could make it a possibility, especially if one was to poorly focus the beam or if significantly more power were to be sent into the trap. User beware.

614 nm laser system

Like our 455 nm light, when I began our 614 nm light was produced by a 1 Watt LED. For its replacement we had a 614 nm laser system that had fallen into disrepair. We recommissioned it in our experiment around the same time that the 455 nm laser was implemented. The 614 nm system is presented in Fig. (4.6) and begins with a Toptica DL 100 diode laser operating at 1228 nm. Directly from the DL 100 the roughly 30 mW output is fiber coupled into a waveguide PPLN frequency doubling unit. The fiber has affixed to it three tension paddles to control the beam's polarization so that it could be aligned optimally to the doubling crystal. The leftover 1228 nm and 614 nm light was free spaced from the

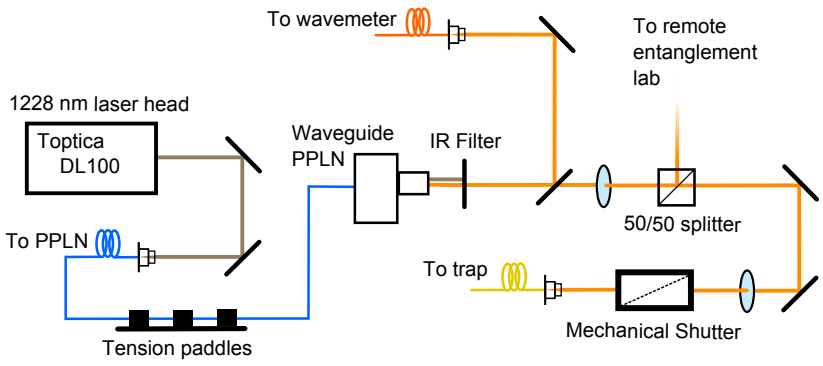

Figure 4.6: Schematic of the 1228/614 nm beam line.

doubler unit and the IR was filtered out, leaving about $100\mu W$ of 614 nm light. A pickoff took some of the orange light to the wave meter and a subsequent 50/50 beam-splitter cube took half the light to be used by other experiments. What was left was passed through a mechanical shutter and fiber coupled for ultimate delivery to the trap. Unlike the 455 nm, the 614 nm laser is not delivered directly to the trap. Its final path leading to the trap will be described in the final section of this chapter.

As seen in the diagram this laser was not stabilized to any reference. Due to the strength of the 614 nm transition and the stability of the DL 100 we found it suitable to leave the laser "free running" and to simply tune the piezo as needed to bring it to the right frequency as seen on the wave meter. Overnight the laser would typically drift a few hundred megahertz and, once tuned in the morning, rarely needed to be touched up until the next day.

4.4.3 Laser cooling and repump: 493/986 nm and 650 nm

The 986/493 nm laser system

The laser cooling transition for Ba^+ is its $6S_{1/2} \leftrightarrow 6P_{1/2}$ transition at 493 nm. Direct diodes for this wavelength were not known to exist when this laser system was first implemented, and so instead we started from a 986 nm laser which was frequency doubled to the desired

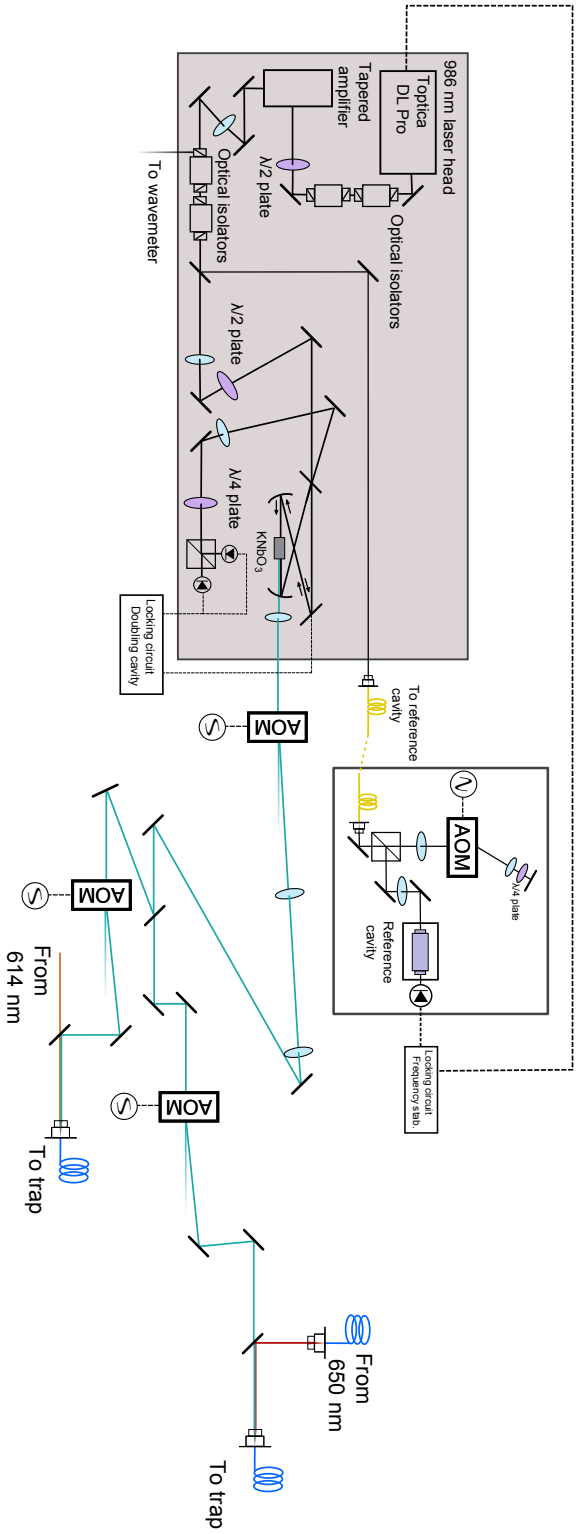

Figure 4.7: Schematic of the 986/493 nm beam line.

wavelength. The 986 nm laser diode was housed in a Toptica DL Pro laser head, which provided us with 15 mW of power and a mode-hop-free tuning range of 15 GHz. The 986/493 nm beam line is drawn in Fig. (4.7). From the laser head the light was passed through an optical isolator and then amplified by a Sacher-Lasertechnik tapered amplifier, which increased the power to 250 mW. The amplified beam was then passed through a second optical isolator, and the small fraction of rejected light was picked off and sent to the wave meter. Following the second isolation stage some additional light was picked off and fiber coupled to be delivered to a reference cavity for frequency stabilization, and the primary beam continued forward toward the doubling crystal.

To frequency stabilize the 986 nm laser we re-purposed an old optical reference cavity that was originally used for an experiment at a similar wavelength in indium. The description of that cavity is provided here [66]. To allow for us to tune the laser frequency with respect to the reference cavity mode - useful when searching for and driving atomic transitions - the light was double passed through an Acousto-optic modulator (DPAOM). A half-wave plate oriented the beam's polarization such that it was maximally reflected off a PBS and directed toward the AOM. On the first pass through the AOM the +1 order was saved and passed through a quarter wave-plate, then retro-reflected back through the wave-plate and AOM. On the second pass the +1 order is saved again, which counter-propagates against the incident beam. Having twice passed through a quarter wave plate, the beam's polarization was rotated 90° so that the light was transmitted by the PBS. Immediately following the DPAOM the light was coupled into the optical reference cavity. Tuning of the laser frequency with respect to the cavity was achieved by changing the AOM drive frequency, which could be varied by ± 30 MHz on top of its nominal frequency of 200 MHz. Since the laser was stabilized in the IR, another factor of two in tuning range existed in the 493 nm beam so that there the total tuning range was 120 MHz. Another benefit of double passing the AOM was that it reduced the need to recouple light into the cavity when the AOM drive frequency was changed. In a single passed configuration, changing the AOM drive frequency would also change the deflection angle and thus the pointing into the cavity. However, in the double passed configuration the deflection from the first pass is corrected by the second pass. The cavity itself is made of Zerodur and is isolated from the room by

a sealed vacuum can. The laser is stabilized to the cavity by a side-of-the-fringe lock. In this approach the transmission through the optical cavity is monitored. The laser frequency is set to some point midway along a cavity transmission line. Frequency shifts above or below that reference level increase or decrease the amount of transmitted light through the cavity, and from that an error signal was generated. A shortcoming of this straightforward approach is that generally the locking circuit cannot discriminate between frequency and intensity noise; nonetheless this approach suited us well in this application.

The majority of the 986 nm light transmitted through the pickoff was frequency doubled by a $KNbO_3$ crystal. The crystal was housed inside of a optical enhancement cavity, sometimes called a "bow-tie" or "ring" cavity [67], to improve conversion efficiency. The enhancement cavity itself required stabilization to maintain the constant production of 493 nm light. The error signal was produced by the Hansch-Couillaud method [68]. In this method of locking an error signal is generated by analyzing the ellipticity of the laser light reflecting off of an optical cavity containing some birefringent element (in the ideal case a polarizer, in ours the $KNbO_3$ crystal). The idea is simplified to consider the polarization of the light reflecting off of the input coupler. This light has two contributions, first from light directly reflected off of the input coupler from the incident beam and another from light leaking out from inside of the cavity. When the cavity is on resonance with the laser these contributions are necessarily in phase, though the plane of their polarization will be rotated due to the polarizing element. If the cavity is off resonance with the laser then these contributions are necessarily not in phase and the polarizer (or birefringent element) in the cavity translates the resulting phase difference to ellipticity. The quarter wave-plate and photo-diode pair that follow after the cavity-reflected beam are used analyze that ellipticity and generate an error signal, which is used to feed back to a piezo to which one of the cavity mirrors are glued. This approach is good for several reasons among which are that it recycles reflected light that would otherwise be wasted and that it exploits a birefringent element that we required in the cavity anyway. In this arrangement we obtained a 150 μW 493 nm beam.

The first element the 493 nm beam encountered was an AOM that served as a master shutter. This laser was adjacent to the 2051 nm laser, whose description is forthcoming,

and the high sensitivity that system had to vibrations precluded use of a mechanical shutter as was done elsewhere. Although the diffracted beam from an AOM is shifted in both space and frequency, a single passed AOM does not give enough optical isolation to be a good shutter. For that reason a second AOM was used as well, which when shuttered in tandem provided sufficient attenuation of the beam. Proceeding the first master-shutter AOM a small percentage of the beam was picked off to be used for optical pumping. That path had its own second AOM and was then combined with the 614 nm laser and fiber coupled for ultimate delivery to the ion. The majority of the 493 nm light, with its own second AOM, was combined with the 650 nm beam and fiber coupled for delivery to the ion.

The 650 nm laser system

The 650 nm laser is an off-the-shelf device. It is a New Focus Vortex laser operating a direct 650 nm diode. Figure (4.8) traces the laser's path. Following an optical isolator and cylindrical lens pair for shaping its spatial profile, the beam is split by a 50/50 beam splitter. Half of the power was sent directly to the wave meter via fiber optic cable. The other half was sent to a beam splitter that send half of the remaining light toward an optical reference cavity and the other half toward the trap by way of another optical fiber. Here, as elsewhere, the high sensitivity of the atom to 650 nm light made a mechanical shutter favorable to alternatives. Occasionally the noise of the shutter would upset the locking system, but that was seldom a problem. To stabilize the 650 nm laser a side-of-the-fringe lock, like the 986 nm laser above, was implemented. The details of the reference cavity and its locking circuitry are described in the thesis of my predecessor, who was responsible for their design and construction [33]. The laser provided us with a total of 8 mW, which was enough that it never caused much of a problem and allowed us to do silly things like send half its power to the wave meter. The ND filter preceding the cavity was added just so that I could see the transmission through the cavity without all the peaks railing. Even with that addition, once locked this laser seldom budged.

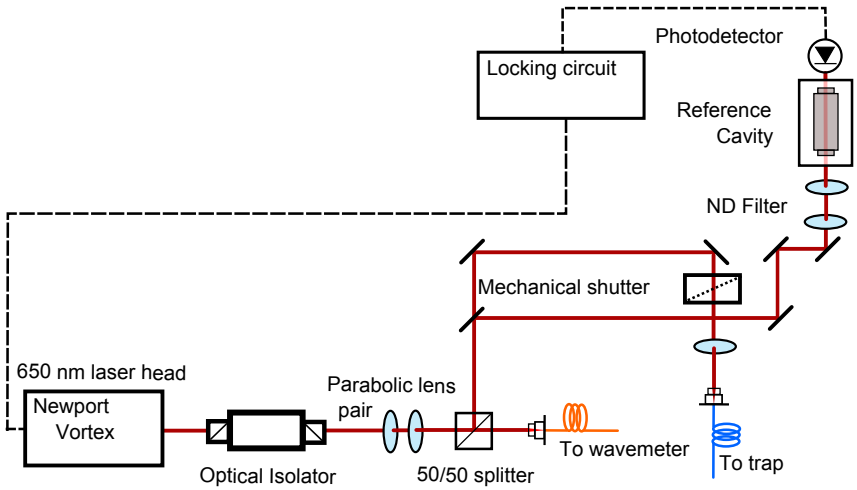

Figure 4.8: Schematic of the 650 nm beam line.

4.4.4 Forbidden spectroscopy: 2051 nm

This laser was the most important tool that we had. It has been written about extensively by my predecessors [69], so my account will be comparatively brief; most of what I have to add to the record are only profanities, anyway. The electric-quadrupole selection rules between the $6S_{1/2}$ and $5D_{3/2}$ states make possible several interesting precision experiments including Ba^+ as an atomic clock and a next-generation APNC measurement. To pursue these experiments the 2051 nm laser must have a very narrow linewidth and good frequency stability, both of which are achieved by stabilizing the laser to a high finesse ultra-low expansion (ULE) reference cavity. The problem, however, is that at the time of its initial construction, sufficiently high quality optical coatings for the cavity mirrors were not available at 2051 nm, and so the choice to stabilize the laser to its second harmonic at 1025 nm was made. This is a variation of the theme that the 2051 nm radiation itself is hard to work with. Standard silicon based photo-detectors and NIR sensor cards have little to no sensitivity to the laser's light which makes even simple laser alignment a challenge. For that reason we do not know accurately how much laser power was in the beam, though we know the total power to be between 35 mW to 40 mW. The 2051 nm beam line, which is depicted

in Fig. (4.10), was probably the most complicated that we employed and undoubtedly the most delicate of our laser systems.

Unlike nearly all of the other lasers previously described, the 2051 nm light source was not an ECDL. It was a diode pumped solid state laser (DPSS) using a TmHo:YLF crystal manufactured by CLR Photonics [70]. The manufacturer-specified linewidth for the laser was <10 kHz with 24 hour stability better than 1 GHz. Coarse tuning of the laser was done by adjusting the laser cavity temperature and fine tuning with a piezo that adjusts the position of one of the cavity mirrors (analogous to an ECDL).

The 2051 nm beam line had three distinct sections: the second harmonic generation section, which was followed by the frequency locking section, and, separated from these by a pickoff, the path to the ion. From the laser head the light passed through an optical isolator and half-wave plate directly through the first AOM. The laser controller box does not permit feedback to the pump diode current so instead this AOM, nominally operated at 55 MHz, was used for high bandwidth feedback from the ULE cavity. Next the beam encounters the pickoff, which sent about 3% of the light toward the ion trap and passed the rest of the light on to the SHG/ULE sections.

The beam passed through the pickoff was immediately sent to be frequency doubled. SHG was done with a custom-made periodically poled lithium niobate crystal (PPLN). The crystal was surrounded by an enhancement cavity to optimize the SHG efficiency, the specific description of which is in [69], and a general discussion of these cavities can be found in [67]. The cavity must be stabilized, and was so with a Hansch-Couillaud locking scheme as in the 493 nm beam line [68].

The 1025 nm light produced by the doubling enhancement cavity was periscoped down and sent through a double-passed AOM, which was nominally driven at 200 MHz. By way of tuning the AOM frequency we were able to tune the laser's frequency over a range of $\pm$ 30 MHz, which was enough in principle to reach all of the 2051 nm transitions. The zeroth order light from the first AOM pass was picked off and redirected to the wave meter. We used the wave meter reading routinely to rough tune the 2051 nm laser frequency. What followed the DPAOM was there to stabilize the laser's frequency to the ULE cavity, which is displayed in Fig. (4.9). Again a reflection based signal was used, but in this instance

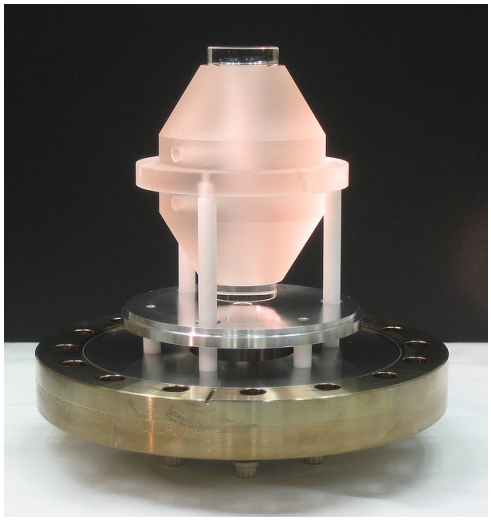

Figure 4.9: A photograph of our ULE cavity taken by former graduate student Jeff Sherman. Not shown is the vacuum system within which it lives.

the Pound-Drever-Hall (PDH) technique [71, 72] was used to generate the error signal. In this approach the frequency of the incident beam is modulated so that a derivative of the reference's resonance feature can be taken and locked to. In our implementation the frequency modulation was generated by an electro-optic modulator (EOM) operating at 20 MHz. Light reflected off of the cavity was rotated into an orthogonal polarization state with respect to the incident beam and redirected by a polarizing beam-splitter cube (PBS) onto a photo-diode. The photo-diode signal along with the 20 MHz modulation frequency are mixed and filtered inside the ULE lock-box to generate the error signal. From there high bandwidth feedback with proportional gain was sent to the initial 55 MHz AOM and low bandwidth feedback with integral gain went to the piezo inside the 2051 nm laser to tune the resonator directly. In addition to the PDH locking circuit, we additionally monitored the ULE cavity transmission with another photo-diode which was useful for monitoring and tuning the locking circuitry. The ULE cavity itself had a measured finesse of around 350,000 and a FSR of $\sim$ 2 GHz [33]. We do not know exactly to what level the laser linewidth was reduced by the stabilization scheme, however from spectroscopy we know it to be bounded to $\mathcal{O}$(10 Hz) or less. Although we have broached that topic here, a proper discussion will

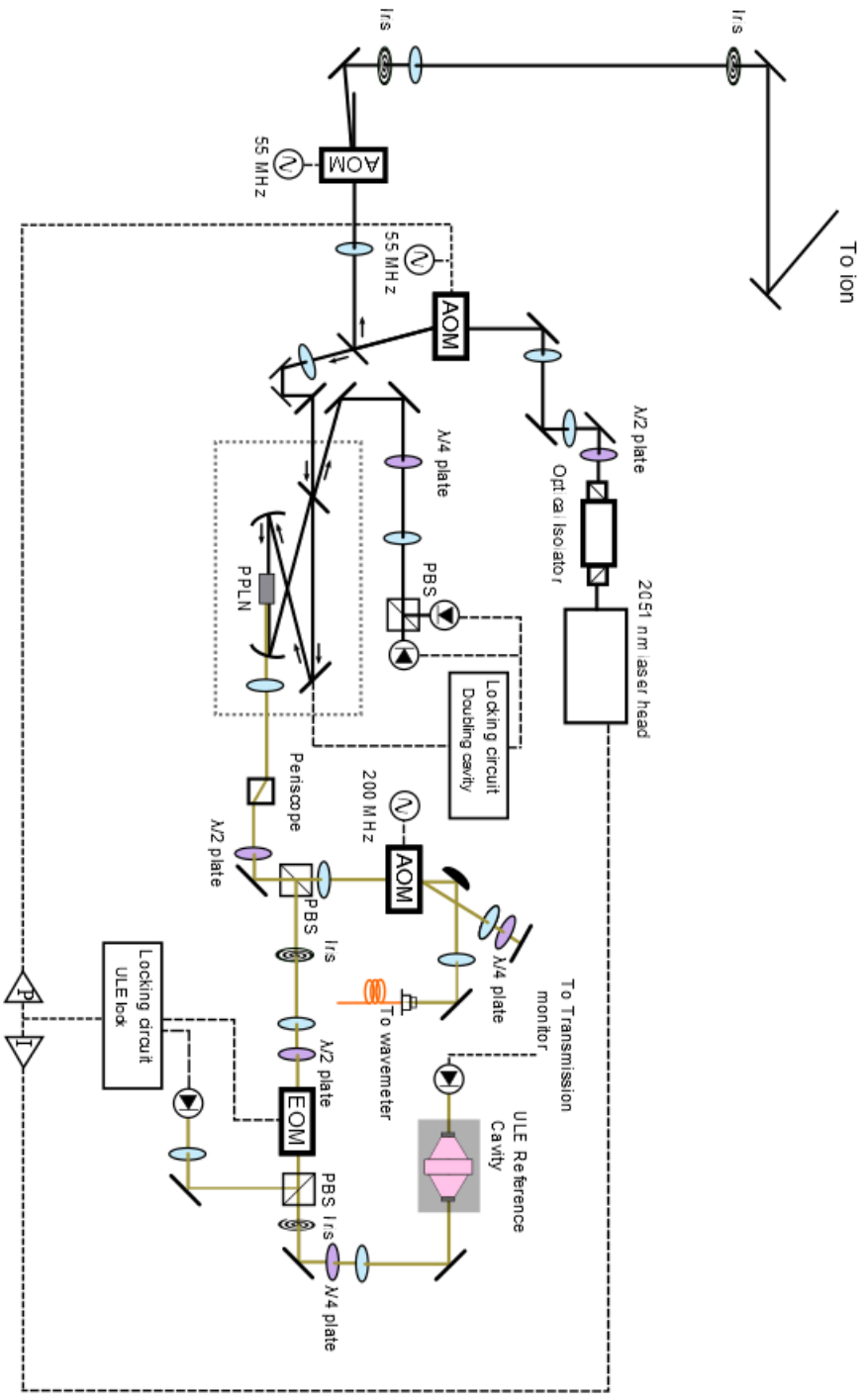

Figure 4.10: Schematic of the 2051 nm beam line. The black solid line traces the 2051 nm beam path while the gold follows the 1025 nm path. Dashed lines indicate electrical connections. The remaining symbols are defined in the text.

be postponed until the systematic analysis of our 2051 nm spectroscopy is presented.

This scheme of stabilizing the 2051 nm laser to its second harmonic was functional but did lead to some frustrating tendencies. Because the two feedback loops are nested they are codependent and could destabilize one another. The SHG lock was particularly susceptible to being unlocked by vibrational perturbations like chairs being moved or tools dropped, which occurred often in my last few years, as there was a new apparatus being built across the room. One future upgrade to this system, should this scheme remain in use with someone brave enough to undertake it, could be to take steps to more thoroughly isolate the SHG cavity from the table. Another more mundane, but also more serious, problem was that the high voltage from the ULE lock-box that was fed back to the laser resonator would become noisy for even modest offset voltages. The consequence was that although the DPAOM had enough tuning bandwidth to reach all of the atomic transitions in principle, this could only be achieved with very tedious temperature tuning so that the lowest transition (in terms of AOM frequency) appeared at nearly zero high voltage offset. For the long run, and especially if 2051 nm laser power becomes more desirable, future 2051 nm operators may wish to revisit the question of how to stabilize this laser. To avoid finding a proper citation, I will report that rumors have existed for some time that coatings at 2000 nm are now feasible and that a high finesse cavity could be constructed there. That would not remedy all of the 2051 nm difficulties, but this is the last of my suggestions for a future I know nothing about.

Redirecting our attention back to the pickoff that sent the majority of the light toward the SHG cavity, the remaining beam was sent to address the ion. We did not have an accurate means to measure the 2051 nm laser power, but we have estimated that about 3% of the laser light was reflected from the pickoff. That light was focused through another AOM that operated at a steady 55 MHz and served as a fast shutter. The single passed diffraction efficiency of this AOM was between 70% to 80%. A mechanical shutter was inappropriate for the 2051 nm beam because they are not fast enough for the kinds of experiments we performed. Moreover, mechanical shutters (that we had anyway) were far too noisy and would destabilize the SHG enhancement cavity lock. After the shutter AOM, the light was lifted to the height of the trap by a long and gradual periscope within which we placed two

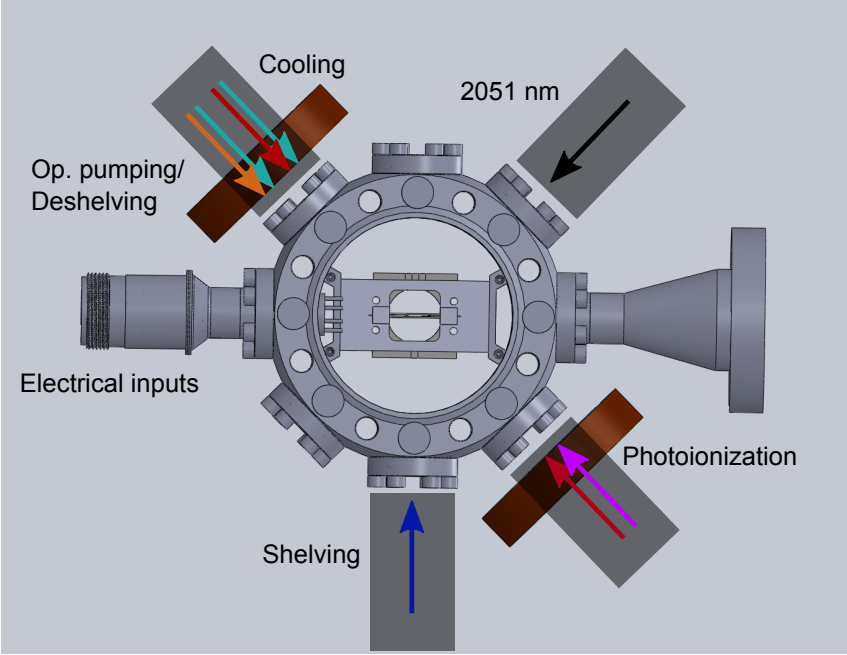

Figure 4.11: A schematic of the spherical octagon housing for our ion trap showing the approach of each laser to the ion. The static magnetic field that define the ion's quantization axis are the brown bands that point parallel to the cooling and photo-ionization beams. Note that the 2051 nm beam approach is nominally 90° to that axis.

irises to assist in alignment. After that a final mirror directed the 2051 nm beam toward the trap and on to the ions.

4.4.5 Optics at the trap

The 493 nm cooling beam and 650 nm beam were delivered to the ion together by an optical fiber. Co-propagating with these are the 493 nm optical pumping beam and 614 nm deshelving beam. Once brought together these beams were reflected off two mirrors for pointing and passed through a focusing lens before entering the trap chamber. These beams were incident on the ion from the direction parallel to the ion's quantization axis, but 45° off of the axial trap dimension. This configuration enabled optimal optical pumping and laser cooling efficiency. Because of the abundance of available red power and the relaxed

demands of the 614 nm beam the focus was set to maximize 493 nm intensity at the ion.

The photo-ionization lasers entered the chamber counter propagating against the cooling lasers. Like with the others, these beams were first roughly pointed through the trap using two mirrors, then focused through the trap with a focusing lens. The ionization lasers and cooling lasers could be tightly aligned to one another by coupling the 791 nm beam into the optical fiber that combined the cooling lasers on the other side of the vacuum chamber, but usually demands on the pointing of the 791 nm and 337 nm beams were not stringent enough to make this necessary. After the measurement described herein was performed, an aperture was added to block some of the 337 nm to mitigate issues it caused related to inducing patch potentials on the trap structure.

The 455 nm beam was delivered to the vacuum chamber by an optical fiber at a view port normal to the ion trap's axial dimension. The fiber output coupler was mounted directly onto a three-axis stage with a lens tube that housed its focusing lens. When used in the multi-mode method previously described the shelving efficiency could be maximized with only minimal effort pointing the laser through the center of the ion trap.

The 2051 nm beam was passed through the trap at nominally 90° to the cooling and photo-ionization beams. After reaching a pair of mirrors that roughly pointed the beam through the vacuum chamber the beam was passed through a polarizer and half-wave plate before being focused through the ion trap. These additional polarization optics were used extensively to carry out the experiments described in Chapter 5.

Chapter 5

MEASUREMENT OF $M1$ FOR THE $6S_{1/2} \leftrightarrow 5D_{3/2}$ TRANSITION

Everything has to be somewhere

- Mrs. Sobel, 9th grade English teacher

Measuring a transition moment is not straightforward. Because they represent rates, which are also affected by the strength and geometry of the driving field, careful work must be undertaken to isolate the underlying matrix elements. The first sections of this chapter describe our attempt to cleverly subvert that difficulty, the rest of the chapter details our first attempt at a measurement of $M1$.

5.1 Deriving formulas for E2 and M1 contributions to Ω

5.1.1 Coordinates

The techniques for measuring the magnetic-dipole-transition moment (M1) we present are conveniently explained by representing the various $6\mathrm{S}_{1/2} \leftrightarrow 5\mathrm{D}_{3/2}$ transition Rabi frequencies in a coordinate system mixed between the atomic reference frame and the 2051 nm laser reference frame. The laser coordinate system, delineated with primes, has its $Z^{'}$ axis parallel to the propagation of the 2051 nm beam at the ion. The atomic frame, which has no primes, is defined with its Z axis parallel to the magnetic field that sets the atom's quantization axis. The angle subtended between these axes will be called θ , so that $\theta = \cos^{-1}\left(\hat{Z} \cdot \hat{Z'}\right)$. The two frames have a common Y-axis which is taken to be normal to the plane spanned by Z and $\mathrm{Z}^{'}$ with the convention that it points "vertically" toward the collection optics. The plane in which θ is subtended is spanned, in either coordinate system, by its Z-axis and an orthogonal X-axis whose orientation is such that both coordinate systems are right-handed. These two coordinate systems are shown graphically in Fig. (5.1) and are related

mathematically by,

$$X^{'} = X\cos(\theta) - Z\sin(\theta) \tag{5.1a}$$

$$Y^{'} = Y \tag{5.1b}$$

$$Z^{'} = X\sin(\theta) + Z\cos(\theta) \tag{5.1c}$$

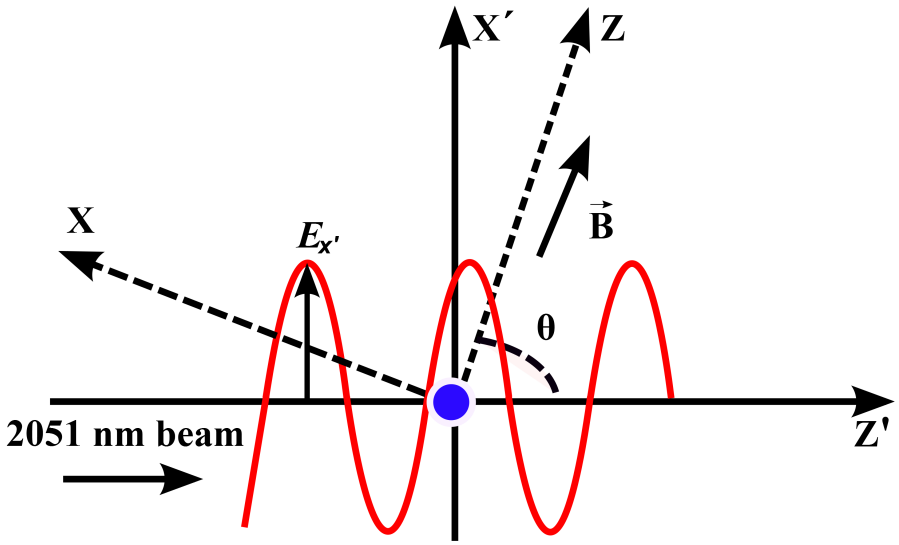

Figure 5.1: The primed coordinate system defines the laser frame with the Z$^{'}$-axis set along the 2051 nm laser. The unprimed coordinates define the atom's frame with the Z-axis set along the externally applied magnetic field **B**. The Y and Y$^{'}$ axes are parallel and point out of the page.

5.1.2 The magnetic-dipole and electric-quadrupole contributions to $\Omega^{(\Delta m)}$

The formulas for the Rabi frequencies $\left(\Omega^{(\Delta m)}\right)$ of each 2051 nm transition between the $6S_{1/2}$ and $5D_{3/2}$ states are derived by deriving the electric-quadrupole and magnetic-dipole contributions separately. The procedure for finding these terms is a standard one: first write down the Cartesian form of the classical Hamiltonian for the interaction in the laser frame, rotate the operators into the atomic reference frame, and transform these into the spherical

basis. These steps yield a general formula, and for each particular transition the Wigner-Eckart Theorem can be applied to leave only the non-vanishing contributions to $\Omega^{(\Delta m)}$ in terms of the reduced matrix elements $M1$ and $E2$ with a few more essential parameters. To begin, recall that for a magnetic-dipole transition [26] the Rabi frequency between the $6S_{1/2}$ and $5D_{3/2}$ states is,

$$\Omega_{M1} = \frac{1}{\hbar}\langle 5D_{3/2}, m^{'}| - \hat{\vec{M}} \cdot \vec{B}|6S_{1/2}, m\rangle \tag{5.2}$$

where the magnetic-dipole operator $\hat{\vec{M}} = M\hat{\vec{J}}$. The magnetic field $\vec{B}$ is that of the 2051 nm laser, not to be confused with the static field that defines the ion's quantization axis. The laser field is described as a classical electromagnetic plane wave,

$$\vec{E} = |E|\hat{\epsilon}e^{i(\vec{k}\cdot\vec{r}-\omega t)} \tag{5.3a}$$

$$\vec{B} = \frac{|E|}{c}(\hat{k}\times\hat{\epsilon})e^{i(\vec{k}\cdot\vec{r}-\omega t)} \tag{5.3b}$$

where $\hat{\epsilon}$ is the plane-wave's polarization vector, $\vec{k}$ and ω are the beam's wave-vector and frequency, respectively, and $|E|$ is the amplitude of its electric field. Maxwell's equations require that an electromagnetic plane wave propagating along $\mathrm{Z}^{'}$ must have $B_{z'} = 0$, so that Ω_{M1} written purely in the laser frame is,

$$\Omega_{M1} = -\frac{1}{\hbar}\langle 5D_{3/2}, m^{'}|\hat{M}_{x'}B_{x'} + \hat{M}_{y'}B_{y'}|6S_{1/2}, m\rangle. \tag{5.4a}$$

Following our prescription we next rotate $\hat{M}_{i'}$ into the (unprimed) atom-frame by applying Eqs. (5.1) to the previous line, which gives,

$$\Omega_{M1} = -\frac{1}{\hbar}\langle 5D_{3/2}, m^{'}|[\,\hat{M}_x\cos(\theta) - \hat{M}_z\sin(\theta)\,]B_{x'} + \hat{M}_y B_{y'}|6S_{1/2}, m\rangle. \tag{5.5}$$

The formulas relating the components, $\hat{M}_x$, $\hat{M}_y$, $\hat{M}_z$, of an arbitrary Cartesian tensor of rank-1 to the rank-1 spherical tensors, $\hat{M}^{(1)}_{-1}$, $\hat{M}^{(1)}_0$, $\hat{M}^{(1)}_{+1}$, are in [27] which are,

$$\hat{M}_x = \frac{1}{\sqrt{2}}\big(\hat{M}^{(1)}_{-1} - \hat{M}^{(1)}_{+1}\big) \tag{5.6a}$$

$$\hat{M}_y = \frac{i}{\sqrt{2}}\big(\hat{M}^{(1)}_{-1} + \hat{M}^{(1)}_{+1}\big) \tag{5.6b}$$

$$\hat{M}_z = \hat{M}_0^{(1)}. \tag{5.6c}$$

Substituting these into Eq. (5.5) gives Ω_{M1},

$$\Omega_{M1} = -\frac{1}{\sqrt{2}\hbar}\langle 5D_{3,2}, m^{'}\big|\left[\,(\hat{M}_{-1}^{(1)} - \hat{M}_{+1}^{(1)})\cos(\theta) - \sqrt{2}\hat{M}_0^{(1)}\sin(\theta)\,\right]B_{x^{'}} + i\left[\,\hat{M}_{-1}^{(1)} + \hat{M}_{+1}^{(1)}\right]B_{y^{'}}\big|6S_{1/2}, m\rangle \tag{5.7}$$

The derivation of Ω_{E2}, the electric-quadrupole contribution to $\Omega^{(\Delta m)}$, proceeds exactly as that for Ω_{M1} starting from the Hamiltonian for an electric-quadrupole interaction [26],

$$\Omega_{E2} = \frac{1}{\hbar}\langle 5D_{3/2}, m^{'}\big| - \frac{1}{6}\hat{Q}_{i^{'}j^{'}}\frac{\partial E_{i^{'}}}{\partial x_{j^{'}}}\big|6S_{1/2}, m\rangle \tag{5.8a}$$

$$\hat{Q}_{i^{'}j^{'}} = e\big(3\hat{x}_{i^{'}}\hat{x}_{j^{'}} - \hat{r}^2\delta_{i^{'}j^{'}}\big) \tag{5.8b}$$

where the quadrupole moment $\hat{Q}_{i^{'}j^{'}}$ is written in terms of the position operators $\hat{x}_i$, e is the electron charge, and $\hat{r}^2 = \hat{x}^2 + \hat{y}^2 + \hat{z}^2$. To evaluate the derivative in Eq. (5.8a) observe that since the beam propagates along the Z$^{'}$-axis in the laser-frame, then the beam's wave vector is $\vec{k}^{'} = \{0, 0, |k|\}$, so that only $\partial E_{i^{'}}/\partial z^{'}$ can be nonzero. Since Maxwell's equations require E_z to be zero as well, only two terms remain, each coming with an ik pre-factor from the derivative,

$$\Omega_{E2} = -\frac{1}{6\hbar}ik\langle 5D_{3,2}, m^{'}\big|\hat{Q}_{x^{'}z^{'}}E_{x^{'}} + \hat{Q}_{y^{'}z^{'}}E_{y^{'}}\big|6S_{1/2}, m\rangle. \tag{5.9}$$

Applying Eq. (5.1) to Eq. (5.9) one arrives at the final Cartesian form of Ω_{E2},

$$\Omega_{E2} = \frac{-ik}{6}\Big\{\Big[\big(\hat{x}^2 - \hat{z}^2\big)\frac{1}{2}\sin(2\theta) + \hat{x}\hat{z}\cos(2\theta)\Big]E_{x^{'}} + \Big[\hat{y}\hat{x}\sin(\theta) + \hat{y}\hat{z}\cos(\theta)\Big]E_{y^{'}}\Big\} \tag{5.10}$$

To proceed with the transformation into the spherical tensor basis we need the spherical tensor representation of the Cartesian tensor combinations in Eq. (5.10). Expressions for generic rank-2 spherical tensors in terms of rank-1 Cartesian tensors follow directly from the discussion found in [27] and are,

$$\hat{Q}^{(2)}_{-2} = \frac{1}{2}\big(\hat{x}^2 - 2\,i\,\hat{x}\,\hat{y} - \hat{y}^2\big) \tag{5.11a}$$

$$\hat{Q}^{(2)}_{-1} = \hat{x}\,\hat{z} - i\,\hat{y}\,\hat{z} \tag{5.11b}$$

$$\hat{Q}^{(2)}_{0} = -\frac{1}{\sqrt{6}}\big(\hat{x}^2 + \hat{y}^2 - 2\hat{z}^2\big) \tag{5.11c}$$

$$\hat{Q}^{(2)}_{+1} = -\big(\hat{x}\,\hat{z} + i\,\hat{y}\,\hat{z}\big) \tag{5.11d}$$

$$\hat{Q}^{(2)}_{+2} = \frac{1}{2}\big(\hat{x}^2 + 2\,i\,\hat{x}\,\hat{y} - \hat{y}^2\big) \tag{5.11e}$$

These equations can be solved for the Cartesian tensor combinations in Eq. (5.10) which, after some algebra, turn out to be,

$$\hat{x}^2 - \hat{z}^2 = \frac{1}{2}\big(\hat{Q}^{(2)}_{-2} + \hat{Q}^{(2)}_{+2} - \sqrt{6}\hat{Q}^{(2)}_{0}\big) \tag{5.12a}$$

$$\hat{x}\hat{z} = \frac{1}{2}\big(\hat{Q}^{(2)}_{-1} - \hat{Q}^{(2)}_{+1}\big) \tag{5.12b}$$

$$\hat{y}\hat{x} = \frac{i}{2}\big(\hat{Q}^{(2)}_{-2} - \hat{Q}^{(2)}_{+2}\big) \tag{5.12c}$$

$$\hat{y}\hat{z} = \frac{i}{2}\big(\hat{Q}^{(2)}_{-1} + \hat{Q}^{(2)}_{+1}\big) \tag{5.12d}$$

Substituting for these gives the final result,

$$\begin{aligned}\Omega_{E2} = \frac{-ik}{2\sqrt{6}\hbar}\big\langle 5D_{3/2},m'\big|\big[\big(\hat{Q}^{(2)}_{-2} + \hat{Q}^{(2)}_{+2} - \sqrt{6}\hat{Q}^{(2)}_{0}\big)\frac{1}{2}\sin(2\theta) + \big(\hat{Q}^{(2)}_{-1} - \hat{Q}^{(2)}_{+1}\big)\cos(2\theta)\big]E_{x'} \\ + i\big[\big(\hat{Q}^{(2)}_{-2} - \hat{Q}^{(2)}_{+2}\big)\sin(\theta) + \big(\hat{Q}^{(2)}_{-1} + \hat{Q}^{(2)}_{+1}\big)\cos(\theta)\big]E_{y'}\big|6S_{1/2},m\big\rangle\end{aligned} \tag{5.13}$$

To conclude the derivation the electric-quadrupole and magnetic-dipole contributions must be added to obtain the total Rabi frequency. This lengthy expression can then be parsed according to particular transitions, whose Rabi frequencies from here on are denoted by $\Omega^{(\Delta m)}$. This is done by selecting appropriate values for m and m' and applying the Wigner-Eckart Theorem to evaluate all matrix elements up to the reduced matrix elements $M1$ and $E2$. The Δm superscript labeling the different transitions is naturally just $m' - m$. In each instance the Clebsch-Gordan coefficients (CGC) are written in explicitly. Table (5.1) organizes the Rabi frequencies for all eight 2051 nm transitions, compiled with its corresponding

states, Δm, and Clebsch-Gordan coefficients.

Now that expressions for each $\Omega^{(\Delta m)}$ have been determined expressions for the components of the laser field $\left(E_{x'}, E_{y'}, B_{x'} \text{ and, } B_{y'}\right)$ are needed to proceed. These expressions, as will be shown in subsequent sections, can become quite cumbersome in their own right.

Table 5.1: $6S_{1/2} \leftrightarrow 5D_{3/2}$ Rabi frequency summary

m	$m^{'}$	Δm	CGC (E2)	CGC (M1)	$\Omega^{(\Delta m)}$
-1/2	3/2	+2	$-\frac{2}{\sqrt{5}}$	0	$\frac{k}{2\sqrt{30}\hbar}\, E2 \left\vert \frac{1}{2}\sin(2\theta)E_{x'} - i\sin(\theta)E_{y'} \right\vert$
-1/2	1/2	+1	$-\sqrt{\frac{3}{5}}$	$\sqrt{\frac{1}{3}}$	$\left\vert \frac{ik}{2\sqrt{10}\hbar} E2(\cos(2\theta)E_{x'} - i\cos(\theta)E_{y'}) - \frac{1}{\sqrt{6}\hbar} M1(\cos(\theta)B_{x'} - iB_{y'}) \right\vert$
-1/2	-1/2	0	$-\sqrt{\frac{2}{5}}$	$\sqrt{\frac{2}{3}}$	$\left\vert \frac{ik}{4\sqrt{10}\hbar}\, E2\, \sin(2\theta)E_{x'} - \frac{1}{\sqrt{6}\hbar}\, M1\, \sin(\theta)B_{x'} \right\vert$
-1/2	-3/2	-1	$-\sqrt{\frac{1}{5}}$	1	$\left\vert \frac{ik}{2\sqrt{30}\hbar} E2(\cos(2\theta)E_{x'} - i\cos(\theta)E_{y'}) + \frac{1}{\sqrt{2}\hbar} M1(\cos(\theta)B_{x'} + iB_{y'}) \right.$
1/2	3/2	+1	$\sqrt{\frac{1}{5}}$	1	$\left\vert \frac{ik}{2\sqrt{30}\hbar} E2(\cos(2\theta)E_{x'} + i\cos(\theta)E_{y'}) + \frac{1}{\sqrt{2}\hbar} M1(\cos(\theta)B_{x'} + iB_{y'}) \right.$
1/2	1/2	0	$\sqrt{\frac{2}{5}}$	$\sqrt{\frac{2}{3}}$	$\left\vert \frac{ik}{4\sqrt{10}\hbar}\, E2\, \sin(2\theta)E_{x'} + \frac{1}{\sqrt{6}\hbar}\, M1\, \sin(\theta)B_{x'} \right\vert$
1/2	-1/2	-1	$\sqrt{\frac{3}{5}}$	$\sqrt{\frac{1}{3}}$	$\left\vert \frac{ik}{2\sqrt{10}\hbar} E2(\cos(2\theta)E_{x'} - i\cos(\theta)E_{y'}) + \frac{1}{\sqrt{6}\hbar} M1(\cos(\theta)B_{x'} - iB_{y'}) \right\vert$
1/2	-3/2	-2	$\frac{2}{\sqrt{5}}$	0	$\frac{k}{2\sqrt{30}\hbar}\, E2 \left\vert \frac{1}{2}\sin(2\theta)E_{x'} + i\sin(\theta)E_{y'} \right\vert$

5.2 Description of two pedagogical methodologies

5.2.1 A sketch of the ideal polarization rotation technique

From the entries in Table (5.1) we can begin to dream up experiments that yield $M1$. The $\Delta m = \pm\ 2$ transitions are magnetic-dipole forbidden, leaving six options containing M1. Of those left we are immediately drawn to the $\Delta m = 0$ transitions for their simplicity. In general a $\Delta m = 0$ transition can only be driven by a field component, electric or magnetic, that is parallel to the system's quantization axis. Each coupling contributes one term, each depending only on the $\hat{x}$ component of the field. It follows that if we drive the $\Delta m = 0$ transitions with a linearly polarized field, we can turn off the electric-quadrupole coupling by rotating the 2051 nm beam's polarization to an orientation where its electric field is perpendicular to the quantization axis. In that geometry only the $M1$ coupling is present and, better still, it is maximized. If we take ϕ to be the orientation of a suitably chosen half-wave plate, with $\phi = 0$ corresponding to the beam's electric field being oriented along $\hat{y}'$, then the electric and magnetic fields are;

$$\begin{pmatrix} E_{x'} \\ E_{y'} \end{pmatrix} = |E| \begin{pmatrix} \sin\left(2\phi\right) \\ -\cos\left(2\phi\right) \end{pmatrix} \qquad \begin{pmatrix} B_{x'} \\ B_{y'} \end{pmatrix} = \frac{|E|}{c} \begin{pmatrix} \cos\left(2\phi\right) \\ \sin\left(2\phi\right) \end{pmatrix}$$

If we subsequently define $A_{E2} = \frac{ik}{4\sqrt{10}\hbar}\big|E\big|\, E2 \sin\left(2\theta\right)$ and $A_{M1} = \frac{1}{\sqrt{6}\hbar}\,\big|E\big|/c\, M1\, \sin(\theta)$, then the total Rabi frequency for either $\Delta m = 0$ transition ($\Omega^{(0)}$) is,

$$\Omega^{(0)} = \sqrt{|A_{E2}|^2 \sin^2\left(2\phi\right) + |A_{M1}|^2 \cos^2\left(2\phi\right)} \tag{5.14}$$

Referring to Table (5.1) (or above to $A_{E2/M1}$), observe that these two contributions have a relative complex phase of i. For that reason in Eq. (5.14) the two contributions add in quadrature and not as a direct sum. This phase will have important consequences later on. Figure (5.2) plots $\Omega^{(0)}(\phi)$ presuming $|A_{E2}|$ to be $\sim$10 kHz, $|A_{M1}|$ to be 30 Hz, and θ to be 70°, which are experimentally realistic values for our apparatus. The plot on top shows $\Omega^{(0)}$ over one full period; the bottom plot is zoomed in on the lowest 100 Hz so that the effect of M1 can be clearly distinguished. The black dashed line shows how $\Omega^{(0)}$ would continue to zero without any M1 contribution, and the blue dashed line shows the M1 contribution by

itself. The minimum in $\Omega^{(0)}$ is solely A_{M1}, but measuring the bottom alone is insufficient for getting to the transition moment since the laser field's amplitude and angle from the quantization axis also factor in. We can eliminate the laser field amplitude dependence by taking the ratio A_{M1} to A_{E2} which leaves,

$$\left|\frac{A_{M1}}{A_{E2}}\right| = \frac{2}{ck}\sqrt{\frac{5}{3}} \times \frac{1}{\cos\left(\theta\right)} \times \frac{M1}{E2} \tag{5.15}$$

The wave-vector of the laser k is known, as is $E2$, leaving only θ as unknown. The experiment then is to measure $\Omega^{(0)}$ as a function of the orientation of the 2051 nm beam's polarization and extract A_{E2} and A_{M1} from a fit.

The alignment angle θ cannot be distinguished well from the same fit since it, independent of the ratio of M1 to E2, also affects the relative size of the two Rabi frequency contributions. We can, however, repeat our polarization rotation measurement on the $\Delta m = \pm 2$ transitions to find θ. For those there is only electric field coupling, but to both the $E_{\hat{x}'}$ and $E_{\hat{y}'}$ components of the laser field. The only thing affecting the relative contributions from these field components are geometrical factors, most pertinent of which is θ. When driven by a linear polarized laser field the Rabi frequency for $\Delta m = \pm\ 2$ are both,

$$\Omega^{(\pm 2)} = C_{E2}\ \sin(\theta)\sqrt{\cos^2(\theta)\sin^2\left(2\phi\right) + \cos^2\left(2\phi\right)} \tag{5.16}$$

Virtually all of the challenges of this approach are in the measuring the minimum in $\Omega^{(0)}$. Qualitatively one can expect a strong trade-off in this approach: more laser power makes A_{M1} larger and easier to measure, but it also makes the approach steeper, requiring tighter control of the beam's polarization alignment. This technique also necessitates measurements of very slow Rabi frequencies, which places stringent demands on the system's decoherence and on the frequency stability of the 2051 nm laser. In terms of the experiment's accuracy the biggest trouble is having the beam's polarization be sufficiently linear. Ellipticity is a complex and multifaceted topic which will be plunged into thoroughly in the subsequent sections.

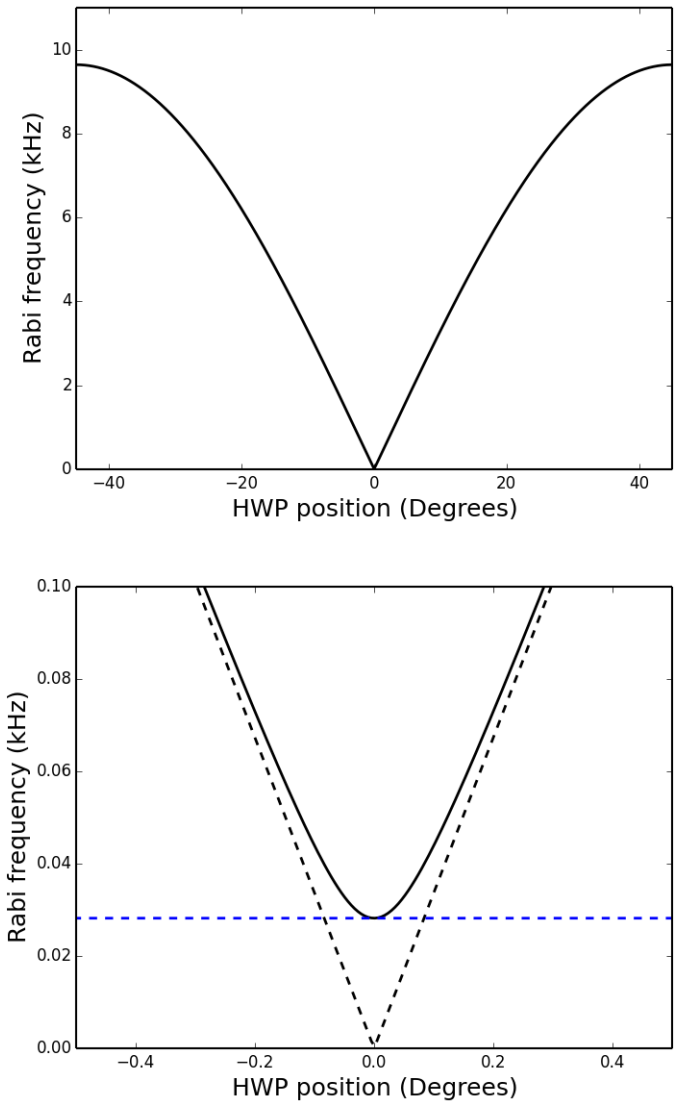

Figure 5.2: A theoretical plot of $\Omega^{(0)}(\phi)$ driven by a linearly polarized 2051 nm beam assuming perfect linear polarization. For this sketch $|A_{E2}|$ is set to $\sim$10 kHz and $|A_{M1}|$ to $\sim$30 Hz.

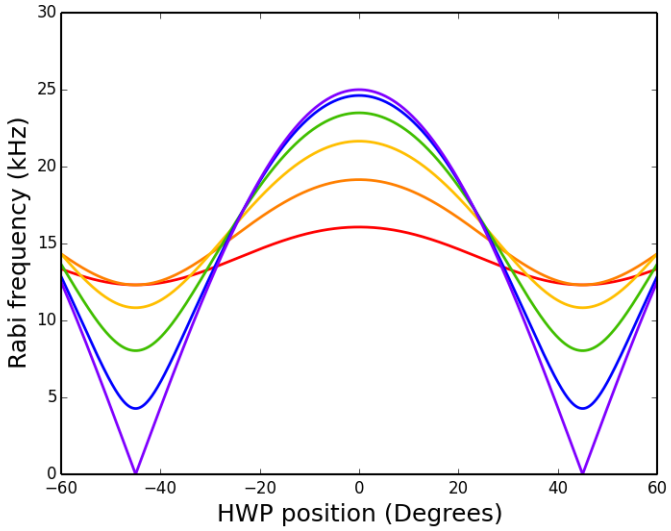

Figure 5.3: A theoretical plot of $\Omega^{(\pm 2)}(\phi)$ driven by a linearly polarized 2051 nm beam assuming perfect linear polarization. For all curves C_{E2} was set to 25 kHz. Each color corresponds to a different value of θ with red, orange, yellow, green, blue, purple corresponding to 40°, 50°, 60°, 70°, 80°, 90°.

5.2.2 A sketch of the ideal reversals techniques

The relative complex phase between the electric and magnetic field couplings in $\Delta m = 0$ offers an opportunity for interference that is not exploited by the polarization rotation technique. Physically it accounts for the fact that, for a linearly polarized electromagnetic wave, $\vec{E}$ and $\vec{B}$ oscillate in-phase and so $|\bigtriangledown \vec{E}|$ and $|\vec{B}|$ must be out-of-phase, resulting in that they combine as an incoherent sum without interference between the couplings. Consider the situation with circularly polarized light for which there are two electric field components, $E_{x'}$ and $E_{y'}$, with a relative complex phase of $\pm i$. That phase difference causes $\partial_{x'} E_{x'}$ to lag or be advanced with respect to $B_{x'}$, so that now they add as a coherent sum. The electric and magnetic fields for a circularly polarized beam are,

$$\begin{pmatrix} E_{x'} \\ E_{y'} \end{pmatrix} = \frac{|E|}{\sqrt{2}} \begin{pmatrix} 1 \\ -\sigma i \end{pmatrix} \qquad \begin{pmatrix} B_{x'} \\ B_{y'} \end{pmatrix} = \frac{|E|}{\sqrt{2c}} \begin{pmatrix} \sigma i \\ 1 \end{pmatrix}$$

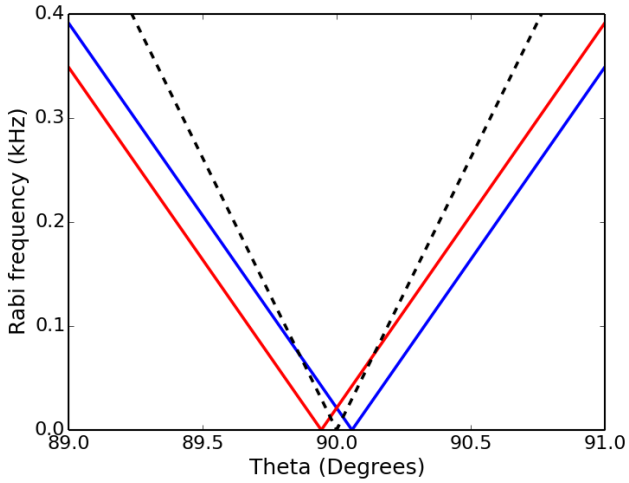

Figure 5.4: Close up plots of the $\Delta m = 0$ transitions driven by perfect circular polarized laser fields. The red and blue curves are obtained for specific choices of states and laser handedness as described in the text. The dashed back curve shows either transition without any magnetic-dipole coupling and with the beam oriented along $\hat{x'}$ to maximally drive the transition.

The parameter σ is either +1 or -1 corresponding to right or left handed polarization. As opposed to the polarization rotation technique, for these laser fields it now matters which of the two $\Delta m = 0$ transitions are driven. That choice is parameterized by which magnetic sub levels are connected, m = m$'$ = $\pm$ 1/2. Taking both these degrees of freedom into account the total Rabi frequency is,

$$\Omega^{(0)}_{\sigma,m} = |C_{E2}\sin(2\theta) + 2m\sigma C_{M1}\sin(\theta)| \tag{5.17}$$

The coefficients $C_{E2/M1}$ are the same as $A_{E2/M1}$ from the last section but with their θ dependences factored to the foreground. This seemingly arbitrary parsing is chosen so that we have something to plot against. Figure (5.4) displays $\Omega^{(0)}_{\sigma,m}$ as a function of θ with the 2mσ = 1 case colored in blue and 2mσ = -1 in red. For comparison $\Omega^{(0)}_{\sigma,m}$ is also included without M1 in the black dashed line; without M1 there is no interference and all choices of m and σ are equivalent.

Eq. (5.17) suggests a few ways to isolate C_{M1}, and from there to get M1. One approach is to hold the handedness of the laser polarization constant and switch between

which transitions are driven by tuning the laser's frequency and optical pumping beam handedness. Another is to hold the transition constant and change the handedness of the 2051 nm beam. The difference between these parameter reversals $\Delta\Omega$ gives,

$$\Delta\Omega = \left|\Omega^{(0)}_{+1,m} - \Omega^{(0)}_{-1,m}\right| = 2C_{M1}\sin(\theta) \tag{5.18a}$$

$$\Delta\Omega = \left|\Omega^{(0)}_{\sigma,+1/2} - \Omega^{(0)}_{\sigma,-1/2}\right| = 2C_{M1}\sin(\theta) \tag{5.18b}$$

Knowledge of θ is still required, as is the laser field amplitude, which are best measured by the polarization rotation method. In terms of these experimentally accessible parameters $M1$ is,

$$M1 = \frac{\sqrt{6}}{2}\hbar c \times \frac{\Delta\Omega}{|E|\sin(\theta)} \tag{5.19}$$

A complementary reversal technique, which was brought to our attention by Professor Emeritus Norval Fortson and that also was the progenitor to the ideas so far described, is to symmetrically flip θ about 90° as a means of measuring $\Delta\Omega$, which in our notation looks like,

$$\Delta\Omega = \left|\Omega^{(0)}_{\sigma,m}(90^\circ + \delta) - \Omega^{(0)}_{\sigma,m}(90^\circ - \delta)\right| \tag{5.20}$$

Flipping θ symmetrically about 90° by a small angle δ reverses the polarization handedness relative to the ion's quantization axis, which is physically equivalent to reversing σ at a fixed θ. The important difference between these approaches is that they (as with changing which transition is driven) reverse the sense of the induced interference with independent experimental degrees of freedom and therefore provide opportunities to test the measurement's consistency.

The reversal approach has a number of advantages over the polarization rotation technique. First and most importantly is that in this approach the E2 coupling is not turned off, but rather is used to significantly enlarge the Rabi frequencies that must be measured to get $M1$. Therefore, in this approach the stringent demands on the system's decoherence placed by the linear polarization method are significantly reduced. Moreover because Eqs. (5.18) and Eq. (5.20) involve reversing experimental unrelated degrees of freedom they can be used in combination to test for systematic effects in the experiment, for example measuring $\Delta\Omega$ by reversing the handedness of the beam using both transitions and other equivalent

combinations. Another potentially powerful means to tune the apparatus could be to make two equivalent reversals in tandem and find the difference to be zero; for example,

$$\Omega^{(0)}_{+1,+1/2} - \Omega^{(0)}_{-1,-1/2} = \Omega^{(0)}_{-1,+1/2} - \Omega^{(0)}_{+1,-1/2} = 0. \tag{5.21}$$

5.3 A birefringence-enhanced measurement technique with demonstration

The polarization rotation technique and the method by reversals use the extreme ideal ends of polarization space. The fundamental challenge with either approach is achieving sufficiently pure polarization states that E2 can be turned off or canceled out to the point that M1 can be clearly distinguished. In the language of those experiments, the theory that existed suggested that A_{M1}/A_{E2} or $C_{M1}/C_{E2} \lesssim 0.01$, which informed us that to not have an erroneous E2 coupling overwhelm M1, the polarization purity must be at least to that same order. At the time of writing, off-the-shelf polarization optics that were adequate to reach that benchmark do not exist, and although (expensive) custom optics could be fabricated to meet the challenge, birefringence in the UHV view port made that alone pointless. The inevitability of ellipticity induced in the beam by the view port, without a large infrastructure investment at any rate, inspired another idea: characterize the ellipticity and use it to make a hybrid approach between the polarization rotation and reversal method. The experiment described and demonstrated herein is to perform the polarization rotation experiment with an elliptical beam, with that ellipticity provided by the UHV view port itself.

5.3.1 Derivation of a practical laser field model

The 2051 nm beam line can be separated into two parts: the final few elements that control the beam's final polarization immediately preceding the ion and everything that comes before. This final section included a polarizer, then a custom made $\lambda/2$-plate, and then the view port leading into the vacuum chamber. A drawing of this arrangement is given in Fig. (5.5). In this section we carry out the Jones calculus for the arrangement to find a realistic model for the 2051 nm laser field.

In accordance with the coordinates defined previously in section (5.1.1), the preferred choice of basis vectors for our Jones analysis of the beam line is,

$$\hat{\epsilon}_{\parallel} = \begin{pmatrix} 1 \\ 0 \end{pmatrix} \qquad \& \qquad \hat{\epsilon}_{\perp} = \begin{pmatrix} 0 \\ 1 \end{pmatrix} \tag{5.22}$$

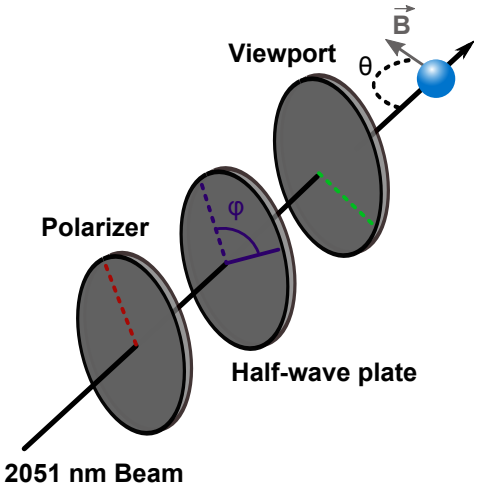

Figure 5.5: A drawing of the polarization control section of the 2051 nm beam line.

where $\hat{\epsilon}_{\|}$ is the field component in the plane spanned by the applied magnetic field $\left(\hat{z}\right)$ and the 2051 nm propagation axis $\left(\hat{z'}\right)$ and $\hat{\epsilon}_{\perp}$ being the field component normal to that plane. Before the polarizer we have some Jones vector,

$$\begin{pmatrix} E_{\|} \\ E_{\perp} \end{pmatrix} \tag{5.23}$$

The size and relative phase of $E_{\|}$ and $E_{\perp}$ summarize the history of the beam before the polarizer, and the details are unimportant. One observation of note, though, is that at the beam's source, immediately following an optical isolator, we had placed a $\lambda/2$-plate which set the beam's initial polarization to be nearly vertical with respect to the optical table. This minimized phase shifts induced from reflecting S- and P- polarized light off of the many mirrors in the beam's path, and thus reduced light wasted by the polarizer. Consequently what is true is that $E_{\perp}$ is substantially larger than $E_{\|}$ at the polarizer, and that there is some non-zero relative phase between them. From here the destination we seek is expressions for $E_{x'}$, $E_{y'}$, $B_{x'}$, and $B_{y'}$ at the ion that can be plugged into the formula of Table (5.1). To treat the polarizer it is important to observe that the orientation of the polarizer's optical axis is not necessarily parallel to $\hat{\epsilon}_{\perp}$, although as a practical matter they were close. Thus we must introduce a tilt angle, named ζ, between the polarizer's optical

axis and $\hat{\epsilon}_\perp$. Following the polarizer, one has,

$$\begin{pmatrix} E_{\parallel'} \\ E_{\perp'} \end{pmatrix} = \begin{pmatrix} \sin^2(\zeta) & -\sin(\zeta)\cos(\zeta) \\ -\sin(\zeta)\cos(\zeta) & \cos^2(\zeta) \end{pmatrix} \begin{pmatrix} E_\parallel \\ E_\perp \end{pmatrix} \tag{5.24a}$$

$$\begin{pmatrix} E_{\parallel'} \\ E_{\perp'} \end{pmatrix} = -\underbrace{\left[E_\perp \cos(\zeta) - E_\parallel \sin(\zeta)\right]}_{E} \sin(\zeta) \begin{pmatrix} 1 \\ 0 \end{pmatrix} + \underbrace{\left[E_\perp \cos(\zeta) - E_\parallel \sin(\zeta)\right]}_{E} \cos(\zeta) \begin{pmatrix} 0 \\ 1 \end{pmatrix} \tag{5.24b}$$

where the matrix in Eq. (5.24a) is the Jones matrix for a polarizer with its with optical axis rotated to ζ. Observe that if $\zeta \to 0$ then we are left with $E_{\perp'}\hat{\epsilon}_\perp$ as expected. The common term E is the total electric field amplitude passed by the polarizer. Since the relative phase between $E_\perp$ and $E_\parallel$ is not known E has some complex phase as well, but since it appears globally it can be omitted and E can be assumed to be real. With the polarizer accounted for there are two more elements whose action on the fields must be determined. First there is the $\lambda/2$ plate, which we model as an arbitrarily oriented phase retarder of retardance γ and optical axis orientation ϕ.

$$\begin{pmatrix} \cos\left(\frac{\gamma}{2}\right) + i\sin\left(\frac{\gamma}{2}\right)\cos(2\phi) & i\sin\left(\frac{\gamma}{2}\right)\sin(2\phi) \\ i\sin\left(\frac{\gamma}{2}\right)\sin(2\phi) & \cos\left(\frac{\gamma}{2}\right) - i\sin\left(\frac{\gamma}{2}\right)\cos(2\phi) \end{pmatrix} \tag{5.25}$$

We treat the view port similarly by labeling its retardance Γ and optical axis orientation α. These parameters are not constant over the view port face, but since the ion interacts with only a small fraction of the total beam it is reasonable to approximate its action with a single phase retarder. To get the combined action of all three elements, we apply these last two Jones matrices in order to the basis vectors in Eq. (5.24b) and get,

$$\begin{pmatrix} E_{x'} \\ E_{y'} \end{pmatrix} = -E\sin\left(\zeta\right) \begin{pmatrix} A_h \\ A_v \end{pmatrix} + E\cos\left(\zeta\right) \begin{pmatrix} B_h \\ B_v \end{pmatrix} \tag{5.26}$$

where the intermediate expressions A_h, A_v, B_h, and B_v are calculated on the next page.

$$\begin{pmatrix} \cos\left(\frac{\Gamma}{2}\right) + i\sin\left(\frac{\Gamma}{2}\right)\cos(2\alpha) & i\sin\left(\frac{\Gamma}{2}\right)\sin(2\alpha) \\ i\sin\left(\frac{\Gamma}{2}\right)\sin(2\alpha) & \cos\left(\frac{\Gamma}{2}\right) - i\sin\left(\frac{\Gamma}{2}\right)\cos(2\alpha) \end{pmatrix} \begin{pmatrix} \cos\left(\frac{\gamma}{2}\right) + i\sin\left(\frac{\gamma}{2}\right)\cos(2\phi) & i\sin\left(\frac{\gamma}{2}\right)\sin(2\phi) \\ i\sin\left(\frac{\gamma}{2}\right)\sin(2\phi) & \cos\left(\frac{\gamma}{2}\right) - i\sin\left(\frac{\gamma}{2}\right)\cos(2\phi) \end{pmatrix} \begin{pmatrix} 1 \\ 0 \end{pmatrix} = \begin{pmatrix} A_h \\ A_v \end{pmatrix}$$

$$A_h = -\sin\left(\frac{\gamma}{2}\right)\sin\left(\frac{\Gamma}{2}\right)\cos(2\alpha - 2\phi) + \cos\left(\frac{\gamma}{2}\right)\cos\left(\frac{\Gamma}{2}\right) + i\Big[\sin\left(\frac{\gamma}{2}\right)\cos\left(\frac{\Gamma}{2}\right)\cos\Big(2\phi\Big) + \cos\left(\frac{\gamma}{2}\right)\sin\left(\frac{\Gamma}{2}\right)\cos\Big(2\alpha\Big)\Big] \quad (5.27)$$

$$A_v = \quad -\sin\left(\frac{\gamma}{2}\right)\sin\left(\frac{\Gamma}{2}\right)\sin(2\alpha - 2\phi) + i\Big[\cos\left(\frac{\gamma}{2}\right)\sin\left(\frac{\Gamma}{2}\right)\sin(2\alpha) + \sin\left(\frac{\gamma}{2}\right)\cos\left(\frac{\Gamma}{2}\right)\sin(2\phi)\Big] \quad (5.28)$$

$$\begin{pmatrix} \cos\left(\frac{\Gamma}{2}\right) + i\sin\left(\frac{\Gamma}{2}\right)\cos(2\alpha) & i\sin\left(\frac{\Gamma}{2}\right)\sin(2\alpha) \\ i\sin\left(\frac{\Gamma}{2}\right)\sin(2\alpha) & \cos\left(\frac{\Gamma}{2}\right) - i\sin\left(\frac{\Gamma}{2}\right)\cos(2\alpha) \end{pmatrix} \begin{pmatrix} \cos\left(\frac{\gamma}{2}\right) + i\sin\left(\frac{\gamma}{2}\right)\cos(2\phi) & i\sin\left(\frac{\gamma}{2}\right)\sin(2\phi) \\ i\sin\left(\frac{\gamma}{2}\right)\sin(2\phi) & \cos\left(\frac{\gamma}{2}\right) - i\sin\left(\frac{\gamma}{2}\right)\cos(2\phi) \end{pmatrix} \begin{pmatrix} 0 \\ 1 \end{pmatrix} = \begin{pmatrix} B_h \\ B_v \end{pmatrix}$$

$$\begin{aligned} B_h &= i\sin\left(\frac{\gamma}{2}\right)\cos\left(\frac{\Gamma}{2}\right)\sin(2\phi) - \sin\left(\frac{\gamma}{2}\right)\sin\left(\frac{\Gamma}{2}\right)\cos(2\alpha)\sin(2\phi) + i\cos\left(\frac{\gamma}{2}\right)\sin\left(\frac{\Gamma}{2}\right)\sin(2\alpha) + \sin\left(\frac{\gamma}{2}\right)\sin\left(\frac{\Gamma}{2}\right)\sin(2\alpha)\cos(2\phi) \\ &= \sin\left(\frac{\gamma}{2}\right)\sin\left(\frac{\Gamma}{2}\right)\sin(2\alpha - 2\phi) + i\Big[\cos\left(\frac{\gamma}{2}\right)\sin\left(\frac{\Gamma}{2}\right)\sin(2\alpha) + \sin\left(\frac{\gamma}{2}\right)\cos\left(\frac{\Gamma}{2}\right)\sin(2\phi)\Big] \end{aligned} \quad (5.29)$$

$$\begin{aligned} B_v &= -\sin\left(\frac{\gamma}{2}\right)\sin\left(\frac{\Gamma}{2}\right)\sin\Big(2\alpha\Big)\sin(2\phi) + \cos\left(\frac{\gamma}{2}\right)\cos\left(\frac{\Gamma}{2}\right) - \sin\left(\frac{\gamma}{2}\right)\sin\left(\frac{\Gamma}{2}\right)\cos\Big(2\alpha\Big)\cos(2\phi) \\ &\quad - i\Big[\sin\left(\frac{\gamma}{2}\right)\cos\left(\frac{\Gamma}{2}\right)\cos\Big(2\phi\Big) + \cos\left(\frac{\gamma}{2}\right)\sin\left(\frac{\Gamma}{2}\right)\cos\Big(2\alpha\Big)\Big] \\ &= -\sin\left(\frac{\gamma}{2}\right)\sin\left(\frac{\Gamma}{2}\right)\cos(2\alpha - 2\phi) + \cos\left(\frac{\gamma}{2}\right)\cos\left(\frac{\Gamma}{2}\right) - i\Big[\sin\left(\frac{\gamma}{2}\right)\cos\left(\frac{\Gamma}{2}\right)\cos\Big(2\phi\Big) + \cos\left(\frac{\gamma}{2}\right)\sin\left(\frac{\Gamma}{2}\right)\cos\Big(2\alpha\Big)\Big] \end{aligned} \quad (5.30)$$

For aesthetic reasons it is nice at this point to change the overall phase of the beam by a factor of $-i$. Doing so and plugging A_h, A_v, B_h, and B_v into Eq. (5.26) one finds,

$$\begin{aligned} E_{x'} = & E \sin\left(\frac{\gamma}{2}\right)\cos\left(\frac{\Gamma}{2}\right)\sin\left(2\phi-\zeta\right) \\ & + E \cos\left(\frac{\gamma}{2}\right)\sin\left(\frac{\Gamma}{2}\right)\sin\left(2\alpha-\zeta\right) \\ & + i\,E \sin\left(\frac{\gamma}{2}\right)\sin\left(\frac{\Gamma}{2}\right)\sin\left(2\phi-2\alpha+\zeta\right) \\ & + i\,E \cos\left(\frac{\gamma}{2}\right)\cos\left(\frac{\Gamma}{2}\right)\sin\left(\zeta\right) \end{aligned} \qquad \begin{aligned} E_{y'} = & -E \sin\left(\frac{\gamma}{2}\right)\cos\left(\frac{\Gamma}{2}\right)\cos\left(2\phi-\zeta\right) \\ & - E \cos\left(\frac{\gamma}{2}\right)\sin\left(\frac{\Gamma}{2}\right)\cos\left(2\alpha-\zeta\right) \\ & + i\,E \sin\left(\frac{\gamma}{2}\right)\sin\left(\frac{\Gamma}{2}\right)\cos\left(2\phi-2\alpha-\zeta\right) \\ & - i\,E \cos\left(\frac{\gamma}{2}\right)\cos\left(\frac{\Gamma}{2}\right)\cos\left(\zeta\right) \end{aligned} \tag{5.31}$$

The Eqs. (5.31) are the total electric field components intentionally passed by the polarizer, but there is still the matter of light leaking through the polarizer, which must be added to Eq. (5.26). We can include these terms without additional algebra by observing that the leaked field must be perpendicular to Eq. (5.24b) immediately following the polarizer, and that the matrices representing an arbitrary phase retarder is unitary. Then all that needs to be done is to rotate Eqs. (5.31) by 90 degrees and replace the electric field amplitude E with a new quantity, η. One notable difference, however, is that although we force the field amplitude E to be real by choice of a global phase, η may well be complex. Keeping that in mind the full electric field seen at the ion will in general be,

$$
\begin{aligned}
E_{x'} = & E \sin\left(\frac{\gamma}{2}\right)\cos\left(\frac{\Gamma}{2}\right)\sin\left(2\phi-\zeta\right) \\
& + E \cos\left(\frac{\gamma}{2}\right)\sin\left(\frac{\Gamma}{2}\right)\sin\left(2\alpha-\zeta\right) \\
& + i\,E \sin\left(\frac{\gamma}{2}\right)\sin\left(\frac{\Gamma}{2}\right)\sin\left(2\phi-2\alpha+\zeta\right) \\
& + i\,E \cos\left(\frac{\gamma}{2}\right)\cos\left(\frac{\Gamma}{2}\right)\sin\left(\zeta\right) \\
& + \eta \sin\left(\frac{\gamma}{2}\right)\cos\left(\frac{\Gamma}{2}\right)\cos\left(2\phi-\zeta\right) \\
& + \eta \cos\left(\frac{\gamma}{2}\right)\sin\left(\frac{\Gamma}{2}\right)\cos\left(2\alpha-\zeta\right) \\
& - i\,\eta \sin\left(\frac{\gamma}{2}\right)\sin\left(\frac{\Gamma}{2}\right)\cos\left(2\phi-2\alpha-\zeta\right) \\
& + i\,\eta \cos\left(\frac{\gamma}{2}\right)\cos\left(\frac{\Gamma}{2}\right)\cos\left(\zeta\right)
\end{aligned}
\qquad
\begin{aligned}
E_{y'} = & - E \sin\left(\frac{\gamma}{2}\right)\cos\left(\frac{\Gamma}{2}\right)\cos\left(2\phi-\zeta\right) \\
& - E \cos\left(\frac{\gamma}{2}\right)\sin\left(\frac{\Gamma}{2}\right)\cos\left(2\alpha-\zeta\right) \\
& + i\,E \sin\left(\frac{\gamma}{2}\right)\sin\left(\frac{\Gamma}{2}\right)\cos\left(2\phi-2\alpha-\zeta\right) \\
& - i\,E \cos\left(\frac{\gamma}{2}\right)\cos\left(\frac{\Gamma}{2}\right)\cos\left(\zeta\right) \\
& + \eta \sin\left(\frac{\gamma}{2}\right)\cos\left(\frac{\Gamma}{2}\right)\sin\left(2\phi-\zeta\right) \\
& + \eta \cos\left(\frac{\gamma}{2}\right)\sin\left(\frac{\Gamma}{2}\right)\sin\left(2\alpha-\zeta\right) \\
& + i\,\eta \sin\left(\frac{\gamma}{2}\right)\sin\left(\frac{\Gamma}{2}\right)\sin\left(2\phi-2\alpha+\zeta\right) \\
& + i\,\eta \cos\left(\frac{\gamma}{2}\right)\cos\left(\frac{\Gamma}{2}\right)\sin\left(\zeta\right)
\end{aligned}
\tag{5.32}
$$

The term-heavy Eqs. (5.32) are the total electric field components having assumed nothing about ζ , γ , Γ or η, and, as such, seem to portend the experiment's doom more than they would seem to be useful for its analysis. Each of these parameters are small, however, which suggests that a next step is to expand the field in their powers. The resulting expansion is a useful framework for estimating uncertainties due to erroneous polarization distortions here and in the ideal polarization rotation experiment. Of course what matters, though, is not how large any of these particular distortions are relative to the rest of the electric field, but rather how they compare to their magnetic field counterparts. Before writing down the expansion a few comments on each of the parameter's relative sizes are called for.

The angle ζ appearing in every term is the tilt between $\hat{\epsilon}_{y'}$ and the orientation of the polarizer. The polarizer was set to pass as much light as possible, which was nearly vertical with respect to the optical table, however that orientation need not coincide with $\hat{\epsilon}_{y'}$ for several reasons. The magnetic field coils used to generate the quantization axis for the experiment are not in true Helmholtz configuration, the effect of which is a magnetic field that diverges slightly. Spurious DC magnetic fields, like that due to the earth, for example, which largely point along the table norm, could also add some tilt. Equivalently the 2051 nm beam does not necessarily pass through the center of its focusing lens. Optical pumping

efficiency is a decent indicator of how parallel the static magnetic field is relative to the OP beam. However, since the OP efficiency is tuned by pointing the laser and not the static magnetic field, and the OP beam passes through lenses on either side of the trap, we can only conclude that ζ is probably not more than a couple degrees. We do not expand in ζ, but its smallness is still important to keep in mind.

We estimated the size of view port birefringence in several view ports using our 650 laser [73]. Each point on the view port acts like a wave-plate with relative phase retardance Γ and an unknown optical-axis orientation α, which can be either of the fast or slow axes. Generally the relative phase difference seen by a beam of wavelength λ, that transmits through a transparent isotropic material under mechanical stress, is described by the stress-optic law [74]:

$$\Gamma = \frac{2\pi C t}{\lambda}\big(\sigma_{11} - \sigma_{22}\big) \tag{5.33}$$

where C is the stress-optic coefficient, t is the thickness of the sample, and σ_{11} and σ_{22} are the first and second principle stresses, respectively. It is thought that stresses associated with installing these view ports and achieving UHV add significantly to the birefringence[1], and so characterizing the exact view port before installation is not predictive, however it does give us the scale of the problem. In order to estimate the size of the effect we measured the amount of stress-induced birefringence in a few used test view ports whose histories were unknown. Those results were roughly consistent across all those tested, and for our paper we described in detail the characterization of one new view port we purchased for that purpose; that discussion is (with some alterations) reproduced below.

A standard 1.33 inch diameter fused silica view port from MDC Vacuum Products, LLC served as a test view port. To replicate a view port *in situ*, the test view port was baked for five days at a temperature of 150° C while pumped down to a pressure of $\sim 2.0 \times 10^{-7}$ Torr. Although longer bakes and lower pressures are needed for real trapped ion experiments these

[1] Anecdotes from our field abound with speculations of the exact sources of birefringence in the standard amorphous view ports that we used. We attempted some quick studies to search out particular mechanisms that induce birefringence but were unable to reach strong conclusions. What we did observe was that even a brand new view port was optically active at about the same level as those which had been used in old vacuum setups.

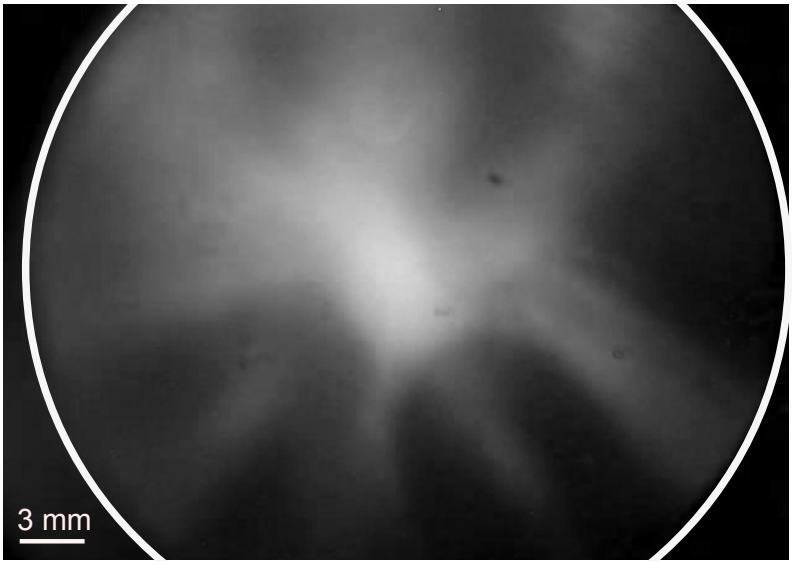

Figure 5.6: A CCD image of the stress pattern in the view port obtained by shining incoherent red light through the view port between a pair of crossed polarizers. The image shows the stress-optic behavior of the view port qualitatively. Bright regions in the image correspond to higher amounts of stress-induced birefringence. The view port edge is indicated in white.

conditions were sufficient for our intentions here. A charge-coupled device (CCD) image of the stress-induced birefringence present in the view port was taken prior to baking and is shown in Fig. 5.6. The figure should be taken with a grain of salt, though, as the intensity over the view port was not uniform, exaggerating the apparent ellipticity at the center.

To quantify the effect we determined the orientation of the view port's optical axes, α, and the relative phase retardation between the axes, Γ, at its center and two points on a diameter. The measurements were made with a linearly polarized 650 nm beam with a full width at half max of 2 mm. The choice to take the measurements at this wavelength was made simply for our convenience, since our 650 nm laser has the most power and is readily fiber coupled. A schematic of the experiment is provided in Fig. (5.6). The 650 nm light was delivered via single-mode optical fiber to a Glan-Thompson polarizer (P1) that set the linear polarization angle Θ of the light incident on the front of the view port. We took $\Theta = 0$ to mean horizontal polarization with respect to the optics table. A second identical

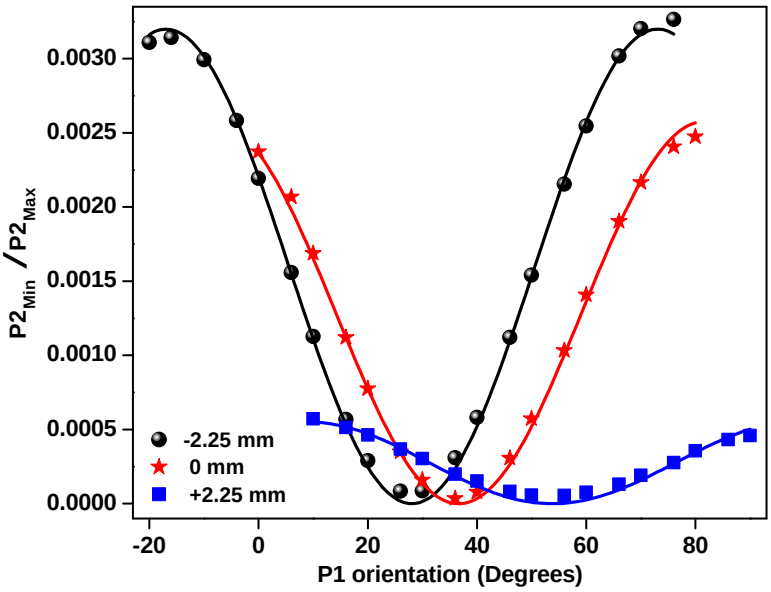

Figure 5.7: Ratio of P_{Min} to P_{Max} as a function of P1 orientation at the center and ± 2.25 mm off center of the view ports. The data is fit to Eq. (5.34) to get Γ and α for each spatial incidence.

Glan-Thomson polarizer (P2) is placed after the test view port and was used to analyze the beam's polarization state after transmitting through the view port. The Glan-Thompson polarizers had a manufacturer quoted extinction ratio of about 100 000:1 in power, which we verified. The relative optical power after P2 was measured with a silicon photo-diode. The optical fiber, polarizers, and photo-diode were mounted on a translation stage that was moved transverse to the view port with a micrometer.

Each measurement consisted of placing P1 to a known orientation and then rotating P2 to find the minimum and maximum power in the beam, P_{Min} and P_{Max}. The ratio P_{Min}/P_{Max} is approximately the square of the ellipticity introduced into the beam's polarization by the view port. The finite extinction ratio of P1 and P2 did cause a non-zero P_{Min}/P_{Max} without a view port placed between the polarizer, however this contribution was

ten times smaller than what was induced by the view port and was ignored.

For this experiment the optical axis orientation and phase retardation of the view port at a given location are related to P_{Min}/P_{Max} by,

$$\frac{P_{Min}}{P_{Max}} = \frac{\sin^2\left[\frac{\Gamma}{2}\right]\sin^2\left[2(\Theta-\alpha)\right]}{1-\sin^2\left[\frac{\Gamma}{2}\right]\sin^2\left[2(\Theta-\alpha)\right]} \tag{5.34}$$

To find Γ and α we measured the power ratio for 18 orientations of P1 between $0\,^\circ$ to $90\,^\circ$ at each spatial incidence; that data is displayed in Fig (5.7). The parameters Γ and α were found by fitting Eq. 5.34 to the data, the results of which are displayed in Table 5.2.

These measurements place an upper bound on the anticipated polarization distortion of

Position	Measured at 650 nm	
	Γ	α
-2.25 mm	$6.47\,^\circ \pm 0.02\,^\circ$	$28.08\,^\circ \pm 0.15\,^\circ$
0.00 mm	$5.81\,^\circ \pm 0.02\,^\circ$	$39.67\,^\circ \pm 0.18\,^\circ$
+2.25 mm	$2.69\,^\circ \pm 0.05\,^\circ$	$53.79\,^\circ \pm 0.57\,^\circ$

Table 5.2: The retardance and optical axis orientation of the view port for the center and opposite points along the edge.

the 2051 nm beam. The stress-optic law predicts that Γ will be about three times less for a 2051 nm beam. The effect is further suppressed at 2051 nm by dispersion of the stress-optic coefficient [75]. Extrapolating the results in Table (5.2) to 2051 nm suggested Γ of a couple degrees as a crude but typical value for the phase retardance to be expected. While this scale does make Γ a reasonable expansion parameter, it is larger than any of the other parameters considered here. What is truly needed is an *in situ* technique to characterize the optical behavior of the view port. We have addressed this issue with a spectroscopic measurement that will be described later on. Risking giving too much away, Γ is indeed about this size.

The $\lambda/2$ plate was a lucky find. It was custom made by Advanced Thin Films for 2053 nm for another customer and was allegedly very nearly ideal at 2051 nm. Because of the

small number of quality polarizers we had at 2051 nm at the time we could not independently verify this claim to better than a few degrees, however for the experiments presented here that was adequate.

The polarizer we used has a manufacturer quoted extinction ratio of 1/10000 in power, or 1/100 in electric field, which we confirmed as best we could by crossing it with another, somewhat inferior, polarizer. This specification means that if we sent equal amounts of light at the polarizer both parallel and perpendicular to its optical axis, then the perpendicular field amplitude leaked through will be about one hundredth the size of the intentionally passed amplitude. In our actual beam line the polarization state of the 2051 nm beam before the polarizer is nearly vertical, so we can safely claim that $\left|\eta/E\right| \ll 0.01$. Although we know that η is small we do not know the phase of the leaked amplitude, so, unlike γ and Γ, η is in general a (small) complex number.

Carrying out these expansions of Eqs. (5.32) to second order gives the following terms,

$$\begin{pmatrix} E_{x'} \\ E_{y'} \end{pmatrix} = E \begin{pmatrix} \sin\left(2\phi - \zeta\right) \\ -\cos\left(2\phi - \zeta\right) \end{pmatrix} + \tag{5.35}$$

$$\underbrace{iE\,\frac{\Gamma}{2}\begin{pmatrix} \sin\left(2\phi - 2\alpha + \zeta\right) \\ \cos\left(2\phi - 2\alpha - \zeta\right) \end{pmatrix} + iE\,\frac{\gamma^{'}}{2}\begin{pmatrix} \sin\left(\zeta\right) \\ -\cos\left(\zeta\right) \end{pmatrix} + \eta\begin{pmatrix} \cos\left(2\phi - \zeta\right) \\ \sin\left(2\phi - \zeta\right) \end{pmatrix}}_{\text{systematic effects at linear order}}$$

$$\underbrace{-E\frac{\gamma^{2'} + \Gamma^2}{8}\begin{pmatrix} \sin\left(2\phi - \zeta\right) \\ -\cos\left(2\phi - \zeta\right) \end{pmatrix} + E\frac{\Gamma\,\gamma^{'}}{4}\begin{pmatrix} \sin\left(2\alpha - \zeta\right) \\ -\cos\left(2\alpha - \zeta\right) \end{pmatrix} + i\eta\frac{\Gamma}{2}\begin{pmatrix} -\cos\left(2\phi - 2\alpha - \zeta\right) \\ \sin\left(2\phi - 2\alpha + \zeta\right) \end{pmatrix} + i\eta\frac{\gamma^{'}}{2}\begin{pmatrix} \cos\left(\zeta\right) \\ \sin\left(\zeta\right) \end{pmatrix}}_{\text{systematic effects at quadratic order}}$$

$$+ \quad \text{effects at higher order}$$

Not surprisingly, the leading order term is simply the action of the $\lambda/2$ plate on a laser field offset by the beam's initial polarization along ζ, which is the ideal behavior expected in the polarization rotation experiment. The subsequent terms represent different distortions incurred by imperfections in the polarization optics. At linear order we find corrections to the beam's polarization due to the independent action of optics. At higher order these effects are combined or compounded.

The magnetic fields are also needed of course, and they can be written down after referring to Eq. (5.3), which informs us that to preserve right handedness $B_{x'}$ must oscillate with $-E_{y'}$ and $B_{y'}$ with $E_{x'}$, so that we have,

$$\begin{aligned}
B_{x'} = {} & B\,\sin\left(\frac{\gamma}{2}\right)\cos\left(\frac{\Gamma}{2}\right)\cos\left(2\phi-\zeta\right) \\
& + B\,\cos\left(\frac{\gamma}{2}\right)\sin\left(\frac{\Gamma}{2}\right)\cos\left(2\alpha-\zeta\right) \\
& - i\,B\,\sin\left(\frac{\gamma}{2}\right)\sin\left(\frac{\Gamma}{2}\right)\cos\left(2\phi-2\alpha-\zeta\right) \\
& + i\,B\,\cos\left(\frac{\gamma}{2}\right)\cos\left(\frac{\Gamma}{2}\right)\cos\left(\zeta\right) \\
& - \eta_B\,\sin\left(\frac{\gamma}{2}\right)\cos\left(\frac{\Gamma}{2}\right)\sin\left(2\phi-\zeta\right) \\
& - \eta_B\,\cos\left(\frac{\gamma}{2}\right)\sin\left(\frac{\Gamma}{2}\right)\sin\left(2\alpha-\zeta\right) \\
& - i\,\eta_B\,\sin\left(\frac{\gamma}{2}\right)\sin\left(\frac{\Gamma}{2}\right)\sin\left(2\phi-2\alpha+\zeta\right) \\
& - i\,\eta_B\,\cos\left(\frac{\gamma}{2}\right)\cos\left(\frac{\Gamma}{2}\right)\sin\left(\zeta\right)
\end{aligned}$$

$$\begin{aligned}
B_{y'} = {} & B\,\sin\left(\frac{\gamma}{2}\right)\cos\left(\frac{\Gamma}{2}\right)\sin\left(2\phi-\zeta\right) \\
& + B\,\cos\left(\frac{\gamma}{2}\right)\sin\left(\frac{\Gamma}{2}\right)\sin\left(2\alpha-\zeta\right) \\
& + i\,B\,\sin\left(\frac{\gamma}{2}\right)\sin\left(\frac{\Gamma}{2}\right)\sin\left(2\phi-2\alpha+\zeta\right) \\
& + i\,B\,\cos\left(\frac{\gamma}{2}\right)\cos\left(\frac{\Gamma}{2}\right)\sin\left(\zeta\right) \\
& + \eta_B\,\sin\left(\frac{\gamma}{2}\right)\cos\left(\frac{\Gamma}{2}\right)\cos\left(2\phi-\zeta\right) \\
& + \eta_B\,\cos\left(\frac{\gamma}{2}\right)\sin\left(\frac{\Gamma}{2}\right)\cos\left(2\alpha-\zeta\right) \\
& - i\,\eta_B\,\sin\left(\frac{\gamma}{2}\right)\sin\left(\frac{\Gamma}{2}\right)\cos\left(2\phi-2\alpha-\zeta\right) \\
& + i\,\eta_B\,\cos\left(\frac{\gamma}{2}\right)\cos\left(\frac{\Gamma}{2}\right)\cos\left(\zeta\right)
\end{aligned} \tag{5.36}$$

The expansion of $\vec{B}$ is less critical than $\vec{E}$, but is written down for completeness all the same.

$$\begin{pmatrix} B_{x'} \\ B_{y'} \end{pmatrix} = B \begin{pmatrix} \cos\left(2\phi - \zeta\right) \\ \sin\left(2\phi - \zeta\right) \end{pmatrix} + \tag{5.37}$$

$$\underbrace{iB\frac{\Gamma}{2}\begin{pmatrix} -\cos\left(2\phi - 2\alpha + \zeta\right) \\ \sin\left(2\phi - 2\alpha + \zeta\right) \end{pmatrix} + iB\frac{\gamma'}{2}\begin{pmatrix} \cos\left(\zeta\right) \\ \sin\left(\zeta\right) \end{pmatrix} + \eta_B \begin{pmatrix} -\sin\left(2\phi - \zeta\right) \\ \cos\left(2\phi - \zeta\right) \end{pmatrix}}_{\text{systematic effects at linear order}}$$

$$\underbrace{-B\frac{\gamma^{2'} + \Gamma^2}{8}\begin{pmatrix} \cos\left(2\phi - \zeta\right) \\ \sin\left(2\phi - \zeta\right) \end{pmatrix} + B\frac{\Gamma\gamma'}{4}\begin{pmatrix} \cos\left(2\alpha - \zeta\right) \\ \sin\left(2\alpha - \zeta\right) \end{pmatrix} - i\eta_B\frac{\Gamma}{2}\begin{pmatrix} \sin\left(2\phi - 2\alpha + \zeta\right) \\ \cos\left(2\phi - 2\alpha - \zeta\right) \end{pmatrix} + i\eta_B\frac{\gamma'}{2}\begin{pmatrix} -\sin\left(\zeta\right) \\ \cos\left(\zeta\right) \end{pmatrix}}_{\text{systematic effects at quadratic order}}$$

$$+ \quad \text{effects at higher order}$$

5.3.2 Simulation of the experiment

To model the behavior expected from the experiment we use Eqs. (5.32) and (5.36) ignoring $\gamma^{'}$, η, and ζ, which are too small to affect the qualitative behavior. The field components left are,

$$E_{x'} = E\Big[\ \cos\Big(\frac{\Gamma}{2}\Big)\sin\big(2\phi\big) + i\ \sin\Big(\frac{\Gamma}{2}\Big)\sin\big(2\phi - 2\alpha\big)\ \Big] \tag{5.38a}$$

$$E_{y'} = -E\Big[\ \cos\Big(\frac{\Gamma}{2}\Big)\cos\big(2\phi\big) - i\ \sin\Big(\frac{\Gamma}{2}\Big)\cos\big(2\phi - 2\alpha\big)\ \Big] \tag{5.38b}$$

$$B_{x'} = B\Big[\ \cos\Big(\frac{\Gamma}{2}\Big)\cos\big(2\phi\big) - i\ \sin\Big(\frac{\Gamma}{2}\Big)\cos\big(2\phi - 2\alpha\big)\Big] \tag{5.39a}$$

$$B_{y'} = B\Big[\ \cos\Big(\frac{\Gamma}{2}\Big)\sin\big(2\phi\big) + i\ \sin\Big(\frac{\Gamma}{2}\Big)\sin\big(2\phi - 2\alpha\big)\ \Big] \tag{5.39b}$$

Figure (5.8) plots $\Omega^{(0)}$ as a function of the polarization orientation ϕ of using these field components. The angle of the optical axis α, relative to $\phi = 0$, was set to -20°. The alignment angle θ was set to 70°, which was about typical. The black, red, blue, and purple curves correspond to a view port retardance of 0°, 5°, 10°, and 20°. Retardances of tens of degrees are greater than we have observed, but are instructive cases modeling. As seen in the figure the ellipticity adds significantly to the minimum in $\Omega^{(0)}$, and also broadens the feature. In the large retardance curves it is evident that in addition to lifting the minimum it also shifts it to the side. This effect is due to the asymmetric relative placement of the view port's optical axis and is not present when α occurs at 45°. For more realistic retardances, which were no more than a few degrees, this effect is negligible but could be significant in future studies. The bottom plot is the same but zoomed in on the minimum feature. The dashed lines correspond to having no M1. From knowledge of Γ and α, the E2 coupling due to the elliptic field at $\phi = 0$ can be subtracted out to leave M1.

To experimentally find α and Γ we look to both of the $\Omega^{(\pm 2)}$ transitions. As we saw before, with a perfectly linear polarized beam these transition's Rabi frequencies are identical, however referring back to Table (5.1) we see that the $E_{x'}$ and $E_{y'}$ components generically add with $\pm i$ complex phase depending on the transition. When driven with an elliptic field, if one experiences constructive interference the other will see destructive

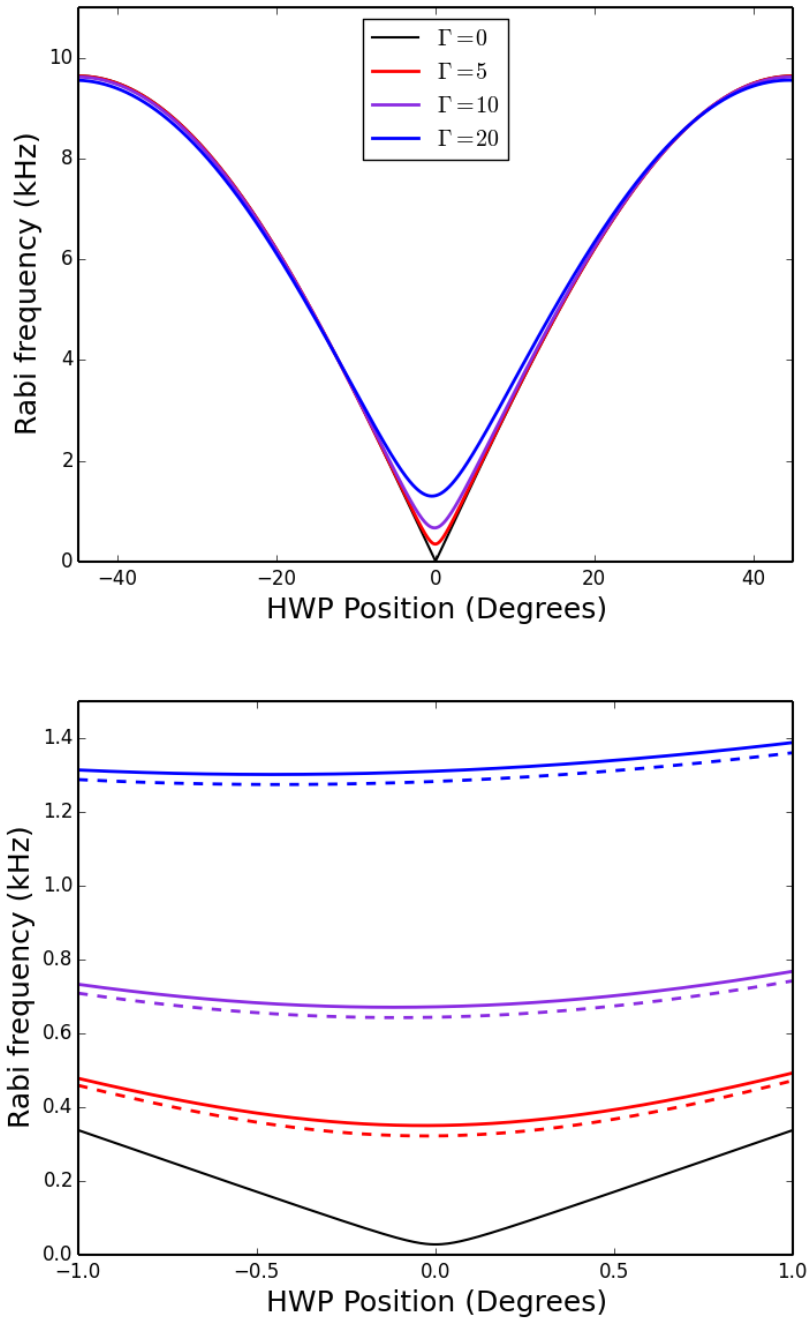

Figure 5.8: Plots of $\Omega^{(0)}$ for the birefringence-enhanced measurement technique. The plot on top shows the full-scale behavior, and the bottom plot zooms in on the minimum feature from which M1 can be extracted. For every plot α was set to 65° and θ was set to 70°, which are experimentally realistic values. Each color represents a different retardance in the arbitrary phase retarder with black, red, purple, and blue corresponding to 0°, 5°, 10°, and 20°, respectively. The dashed lines in the zoomed-in plot have A_{M1} set to zero, and in the solid lines it is 30 Hz. In all plots A_{E2} is 15 kHz.

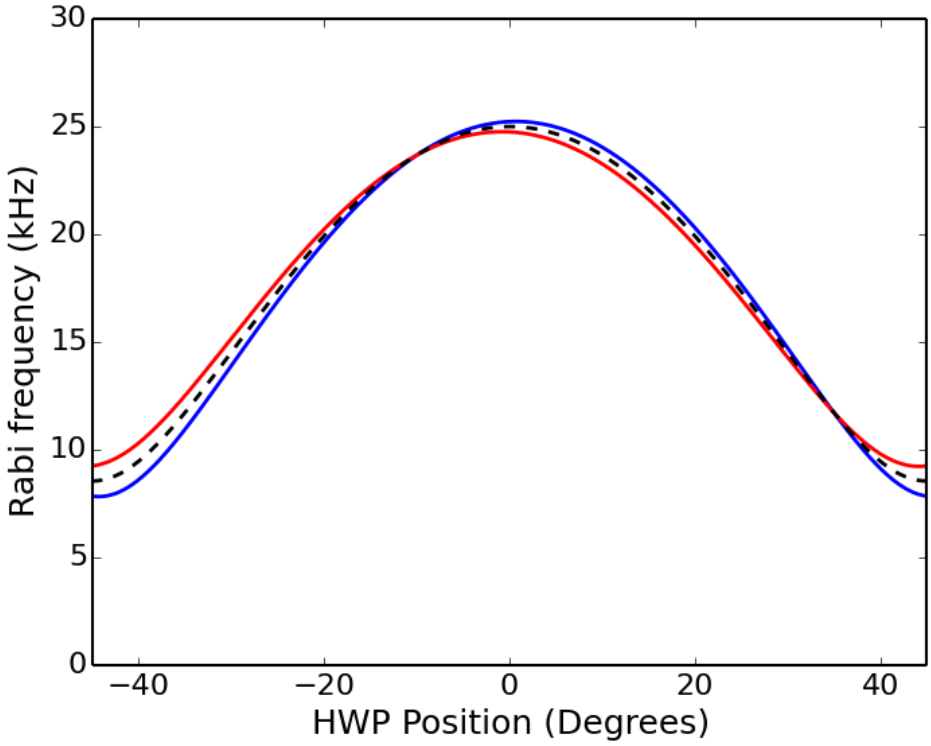

Figure 5.9: Plots of both of the $\Omega^{(\pm 2)}$ transitions including the effects of the view port birefringence. The blue and red curves correspond to Δm = +2 and Δm = -2, respectively. For this simulation the view port's optical axis, α was set to -20° and its retardance, Γ, was set to 5°.

interference, causing them to become skewed with respect to one another. Where the two curves cross over each other indicates the location of the optical axes, and the amount of asymmetry between them increases with Γ, as seen in Fig. (5.9). The blue and red curves there are Δm of +2 and -2 respectively for $\alpha = -20°$ and $\Gamma = 5°$.

5.3.3 Data and analysis

To obtain all of the necessary pieces needed to get M1, three measurements were undertaken; first of $\Omega^{(0)}$, then $\Omega^{(+2)}$ alone, then $\Omega^{(\pm 2)}$ measured simultaneously. A sample Rabi flop is displayed in Fig. (5.10). The first two Rabi oscillation data sets were used to calculate M1 without correcting for 2051 nm ellipticity, and the $\Omega^{\pm 2}$ data were used to extract the view port parameters. In all cases the Rabi frequency measurements were taken at 10° intervals of half-wave plate rotation, except near the minimum of $\Omega^{(0)}$, where more data was needed. The half-wave plate position was set manually using a Thorlabs PRM1 high-precision rotation mount, which had an angular resolution of five arc-minutes read off a vernier scale. All Rabi frequency measurements were recorded with respect to the reading of the half-wave plate's rotation mount which were assigned a ± 10 arc-minute (0.16°) error bar to account for potentially misreading the scale. The rotation was always carried out from low angle to high angle to avoid inconsistency from backlash. We did not know *a priori* how the half-wave plate was oriented in its rotation mount (with respect to the plane spanned by the 2051 nm $\vec{k}$ vector and the ion's quantization axis), so in all cases the data were fit with an additional phase offset ϕ_0 to account for this initial alignment. This angle is different from ζ, which accounts for misalignment of the polarizer.

Each individual experimental run, be it to map out the transition resonance or to perform a Rabi oscillation, took about five minutes. Most of that time was software overhead. To ensure that the 2051 nm laser was on resonance for each Rabi oscillation measurement the resonance was remapped every few scans. For the view port birefringence calibration data frequency scans were needed before each Rabi frequency measurement because of the additional time needed to tune the laser between the two transition. Tables (5.3), (5.4), and (5.5) summarize the pertinent fit parameters for all resonance scan and Rabi oscillation runs for the polarization rotation measurement. In those tables the resonance frequencies f_0 (relative to the 2051 nm ULE) are listed in MHz with the transition's full width at half max (FWHM) in the adjacent bracket. Uncertainties for these parameters are not listed, but in all cases they were below or just at the order of the least significant digit reported. Observe that by that rule the transition resonance was resolved to at least an order of mag-

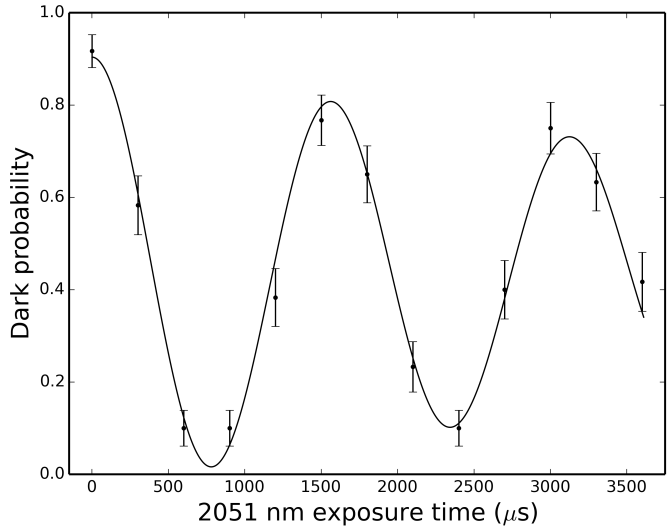

Figure 5.10: An example of a Rabi oscillation taken along the 2051 nm Δm=0 transition.

nitude better than the FWHM for all positions. The remaining parameters all pertain to the corresponding Rabi oscillation measurement. Please take note that all measured Rabi frequencies are reported as a linear frequency, $\Omega/2\pi$. Each frequency scan also had a fitted shelving and optical pumping efficiency as well, however these are not reported because they are redundant and uninteresting.

The data for $\Omega^{(+2)}(\phi)$ and $\Omega^{(0)}(\phi)$ are plotted together in the top panel of Fig. (5.11). Fitting the data with the full laser field model developed in Sec. (5.3) is impractical because of the overwhelming number of terms and parameters, many of which add qualitatively similar features. Instead to fit these data we assume the ideal experiment using the perfect linear polarization model of Sec. (5.2.1). As we saw in Sec. (5.3.2) for the low amounts of stress-induced birefringence we expect (and will see shortly) the principle effect of the view port in the $\Omega^{(0)}(\phi)$ data is to raise the minimum value observed, $\Omega^{(0)}_{min}$, without significantly skewing its position. The consequence of these observations is that the fit model, to a good approximation, looks exactly the same as the ideal experiment prescribed by Eq. (5.14) except for the reinterpretation that $\Omega^{(0)}_{min}$ now equals $A^{(0)}_{M1}$ plus some erroneous E2 coupling that we can subtract out once the view port parameters are known. The model used to fit

the data then is,

$$\Omega^{(0)}_{ideal} = \sqrt{|\Omega^{(0)}_{max}|^2 \sin^2(2\phi - 2\phi_0) + |\Omega^{(0)}_{min}|^2 \cos^2(2\phi - 2\phi_0)} \tag{5.40}$$

Where the variables A_{E2} and A_{M1} have been relabeled to $\Omega^{(0)}_{max}$ and $\Omega^{(0)}_{min}$ because of the shift in their interpretation. In the data we were unable to properly resolve $\Omega^{(0)}_{min}$ because of the system's decoherence, and for that reason what we will report here is an upper limit on M1. To get that limit (without the ellipticity correction) we need the alignment angle between the 2051 nm laser and the ion's quantization axis θ which we get from the stand-alone measurement of $\Omega^{(+2)}$.

Again here we use the ideal experimental model for the fit. The angle is a fit parameter to the data and accounts for the amplitude of the oscillation in $\Omega^{(+2)}(\phi)$. The effect of ellipticity in the beam, as can be seen qualitatively in Fig. (5.9), is to skew the data both vertically and horizontally which shifts θ's apparent value, however the effect contributes minimally to our final M1 value and can be corrected for once the view port parameters are known. And so to obtain θ we proceed with the ideal fit model for the transition which again is,

$$\Omega^{(+2)}_{ideal} = C_{E2} \sin(\theta) \sqrt{\cos^2(\theta) \sin^2(2\phi - 2\phi_0) + \cos^2(2\phi - 2\phi_0)} \tag{5.41}$$

which is the same as Eq. (5.16) with the phase offset ϕ_0 included. Because this ideal fit model does not have any parameters to allow for asymmetry, the resulting χ^2 is unsurprisingly quite large. Using other *ad hoc* models with a parameter to allow for asymmetry can improve the χ^2, but those do not significantly affect the fitted value of θ. Once we have the view port parameters we can to first order correct θ to get closer to the true value, however as the physics has it M1 is not particularly sensitive to θ, at least for our chosen geometry, so this correction is not critical for the experiments interpretation. Returning to Fig. (5.11), the bottom panel displays the fractional residuals from both the fits and the fitted parameters for the measurements are listed in Table (5.6). A sanity check we can take from the fits is that ϕ_0 agrees between either fit to a few hundredths of a degree.

Table 5.3: Measurements of $\Omega^{(0)}(\phi)$ and their associated fit parameters

HWP Pos.	f_0 [FWHM] (MHz)	Sh. Eff.	Op. Eff.	$\Omega^{(0)}(\phi)/2\pi$ (kHz)	$\gamma/2\pi$ (kHz)	χ^2
32.0°	217.0312 [0.0104]	0.90 ± 0.03	0.87 ± 0.04	12.059 ± 0.074	-0.084 ± 0.128	0.65
40.0°	−−	0.90 ± 0.05	0.97 ± 0.05	11.697 ± 0.155	0.223 ± 0.185	2.32
50.0°	−−	0.89 ± 0.04	0.95 ± 0.04	10.067 ± 0.092	0.094 ± 0.146	1.14
60.0°	217.0315 [0.0057]	0.90 ± 0.04	0.93 ± 0.05	6.711 ± 0.083	0.090 ± 0.114	1.51
70.0°	−−	0.84 ± 0.04	0.89 ± 0.05	3.036 ± 0.047	0.002 ± 0.073	1.24
72.0°	217.0318 [0.0027]	0.90 ± 0.03	0.95 ± 0.04	2.202 ± 0.028	0.039 ± 0.033	1.19
74.0°	−−	0.92 ± 0.03	0.91 ± 0.05	1.430 ± 0.028	0.063 ± 0.032	1.14
75.0°	217.03224 [0.0010]	0.94 ± 0.04	0.94 ± 0.06	0.970 ± 0.024	0.084 ± 0.027	1.63
75.5°	−−	0.93 ± 0.05	1.07 ± 0.06	0.773 ± 0.025	0.088 ± 0.029	2.30
75.8°	217.03258 [0.0008]	0.93 ± 0.06	1.03 ± 0.09	0.664 ± 0.043	0.138 ± 0.047	3.17
75.8°	−−	0.99 ± 0.02	1.15 ± 0.06	0.643 ± 0.041	0.171 ± 0.041	2.46
79.0°	217.03292 [0.0011]	0.88 ± 0.07	0.99 ± 0.10	0.831 ± 0.040	0.112 ± 0.049	3.51
80.0°	217.03338 [0.0010]	0.95 ± 0.03	0.93 ± 0.04	1.222 ± 0.018	0.095 ± 0.023	0.85
82.0°	−−	0.87 ± 0.03	0.91 ± 0.04	2.077 ± 0.014	0.010 ± 0.019	0.68
85.0°	−−	0.92 ± 0.03	0.89 ± 0.04	3.269 ± 0.030	0.030 ± 0.035	0.96
90.0°	−−	0.86 ± 0.04	0.91 ± 0.06	5.264 ± 0.055	0.015 ± 0.072	1.82
100.0°	−−	0.94 ± 0.02	1.04 ± 0.02	8.591 ± 0.062	0.331 ± 0.067	0.66
110.0°	−−	0.86 ± 0.02	0.89 ± 0.04	11.175 ± 0.077	-0.029 ± 0.112	0.53
120.0°	−−	0.87 ± 0.03	0.84 ± 0.05	12.206 ± 0.088	-0.241 ± 0.156	1.03
125.0°	−−	0.90 ± 0.03	0.90 ± 0.04	12.065 ± 0.122	0.301 ± 0.169	0.76

Table 5.4: Measurements of $\Omega^{(+2)}(\phi)$ and their associated fit parameters

HWP Pos.	f_0 [FWHM] (MHz)	Sh. Eff.	Op. Eff.	$\frac{\Omega^{(+2)}(\phi)}{2\pi}$ (kHz)	$\gamma/2\pi$ (kHz)	χ^2
20.0°	211.343 [0.011]	0.88 ± 0.02	0.86 ± 0.04	9.035 ± 0.073	0.093 ± 0.101	0.62
30.0°	−−	0.88 ± 0.02	0.90 ± 0.03	6.919 ± 0.060	0.093 ± 0.086	0.51
40.0°	−−	0.95 ± 0.02	0.94 ± 0.03	7.900 ± 0.103	0.372 ± 0.108	0.83
50.0°	−−	0.89 ± 0.02	0.91 ± 0.03	10.713 ± 0.077	0.140 ± 0.101	0.53
60.0°	211.341 [0.014]	0.92 ± 0.01	0.93 ± 0.02	13.959 ± 0.071	0.210 ± 0.093	0.32
70.0°	−−	0.89 ± 0.06	0.93 ± 0.08	15.442 ± 0.253	0.369 ± 0.379	3.42
80.0°	211.341 [0.020]	0.89 ± 0.03	0.85 ± 0.05	15.956 ± 0.155	-0.177 ± 0.222	1.26
90.0°	−−	0.91 ± 0.04	0.94 ± 0.05	14.833 ± 0.150	0.211 ± 0.238	1.65
100.0°	211.340 [0.012]	0.84 ± 0.03	0.86 ± 0.04	12.250 ± 0.079	-0.054 ± 0.134	0.68
110.0°	211.340 [0.008]	0.86 ± 0.02	0.86 ± 0.04	9.039 ± 0.072	-0.011 ± 0.100	0.70
120.0°	211.341 [0.008]	0.89 ± 0.02	0.86 ± 0.02	7.153 ± 0.046	0.005 ± 0.072	0.36
130.0°	−−	0.83 ± 0.03	0.84 ± 0.05	7.863 ± 0.089	-0.138 ± 0.129	1.14

Table 5.5: Measurements of $\Omega^{(\pm 2)}(\phi)$ and their associated fit parameters. The resonance frequencies for the Δm = +2 and Δm = -2 were nominally 210.2 MHz and 228.8 MHz, respectively.

HWP Pos.	f_0 [FWHM] (MHz)	Sh. Eff.	Op. Eff.	$\Omega^{(\pm 2)}(\phi)/2\pi$ (kHz)	$\gamma/2\pi$ (kHz)	χ^2
30.0	210.206 [0.011]	0.86 ± 0.04	0.85 ± 0.06	7.159 ± 0.101	-0.024 ± 0.140	1.35
	228.822 [0.009]	0.92 ± 0.04	0.85 ± 0.07	7.717 ± 0.147	0.154 ± 0.206	2.22
40.0	210.204 [0.010]	0.94 ± 0.03	0.92 ± 0.06	$9.222 \pm 0.s146$	0.221 ± 0.182	2.10
	228.821 [0.011]	0.83 ± 0.04	0.73 ± 0.07	10.014 ± 0.109	-0.200 ± 0.215	1.32
50.0	228.820 [0.014]	0.82 ± 0.02	0.82 ± 0.04	12.388 ± 0.073	-0.138 ± 0.120	0.41
	210.203 [0.015]	0.90 ± 0.04	0.84 ± 0.05	12.793 ± 0.146	0.105 ± 0.194	1.23
60.0	210.202 [0.017]	0.88 ± 0.03	0.94 ± 0.04	15.195 ± 0.152	0.510 ± 0.200	0.66
	228.821 [0.018]	0.90 ± 0.02	0.87 ± 0.04	15.477 ± 0.134	0.379 ± 0.194	0.56
70.0	228.819 [0.019]	0.89 ± 0.02	0.93 ± 0.03	16.769 ± 0.128	0.243 ± 0.181	0.57
	210.201 [0.020]	0.91 ± 0.06	0.84 ± 0.09	16.484 ± 0.299	-0.103 ± 0.448	3.45
80.0	210.201 [0.020]	0.87 ± 0.04	0.93 ± 0.05	16.458 ± 0.211	0.369 ± 0.285	1.20
	228.817 [0.017]	0.86 ± 0.03	0.79 ± 0.05	16.059 ± 0.175	-0.051 ± 0.256	0.83
90.0	228.817 [0.019]	0.94 ± 0.04	0.89 ± 0.06	14.696 ± 0.282	0.362 ± 0.304	2.15
	210.200 [0.020]	0.83 ± 0.04	0.75 ± 0.07	14.454 ± 0.235	-0.203 ± 0.348	1.42
100.0	210.200 [0.014]	0.84 ± 0.05	0.81 ± 0.08	11.899 ± 0.188	-0.408 ± 0.275	2.47
	228.817 [0.015]s	0.94 ± 0.04	0.90 ± 0.05	11.68 ± 0.18	0.166 ± 0.213	1.78

Table 5.6: Fit parameters for the $\Omega^{(0)}(\phi)$ and $\Omega^{(+2)}(\phi)$ measurements

$\Omega^{(0)}$	$\Omega^{(0)}_{max}/2\pi$ (Hz)	$\Omega^{(0)}_{min}/2\pi$ (Hz)	ϕ_0 (Degrees)	χ^2
	12156 ± 35	319 ± 34	$77.18° \pm 0.02°$	1.29

$\Omega^{(+2)}$	C_{E2} (Hz)	θ (Degrees)	ϕ_0 (Degrees)	χ^2
	17764 ± 81	$64.4 \pm .3$	$77.16° \pm 0.19°$	3.6

To find the view port optical axis orientation α and its retardance Γ we measured $\Omega^{(\pm 2)}(\phi)$ simultaneously. These data had to be collected and interpreted in isolation from the previous data sets because in the interim we were forced to change our quantization axis (and θ with it) for the needs of another experiment. However the 2051 nm pointing onto the atom was not changed and therefore from these data α and Γ were consistent. Because the $\pm$ 2 transitions involve different ground states the optical pumping handedness had to be flipped as well as the laser frequency be tuned. This adds real time into the measurement, so partially to expedite the collection the data were collected by fixing the HWP orientation, were measuring both of the $\pm$ 2 transition Rabi frequencies before moving on to the next HWP position, whereupon the transitions then measured in the opposite order. By staggering the measurements this way fewer changes had to be made to the system before any one scan. Because of the extra time taken between measurements on the same transition and the size of the laser tunings required, the resonances were mapped before every Rabi oscillation measurement. The data are plotted in Fig. (5.12).

To analyze these data we fit under the assumption that the view port is the only source of birefringence as was modeled in Sec. (5.3.2). This choice is motivated there and by the discussion in Sec. (5.3) where it was pointed out that Γ is the largest and most critical ellipticity-inducing parameter. Taking the electric field from the simulation and plugging it

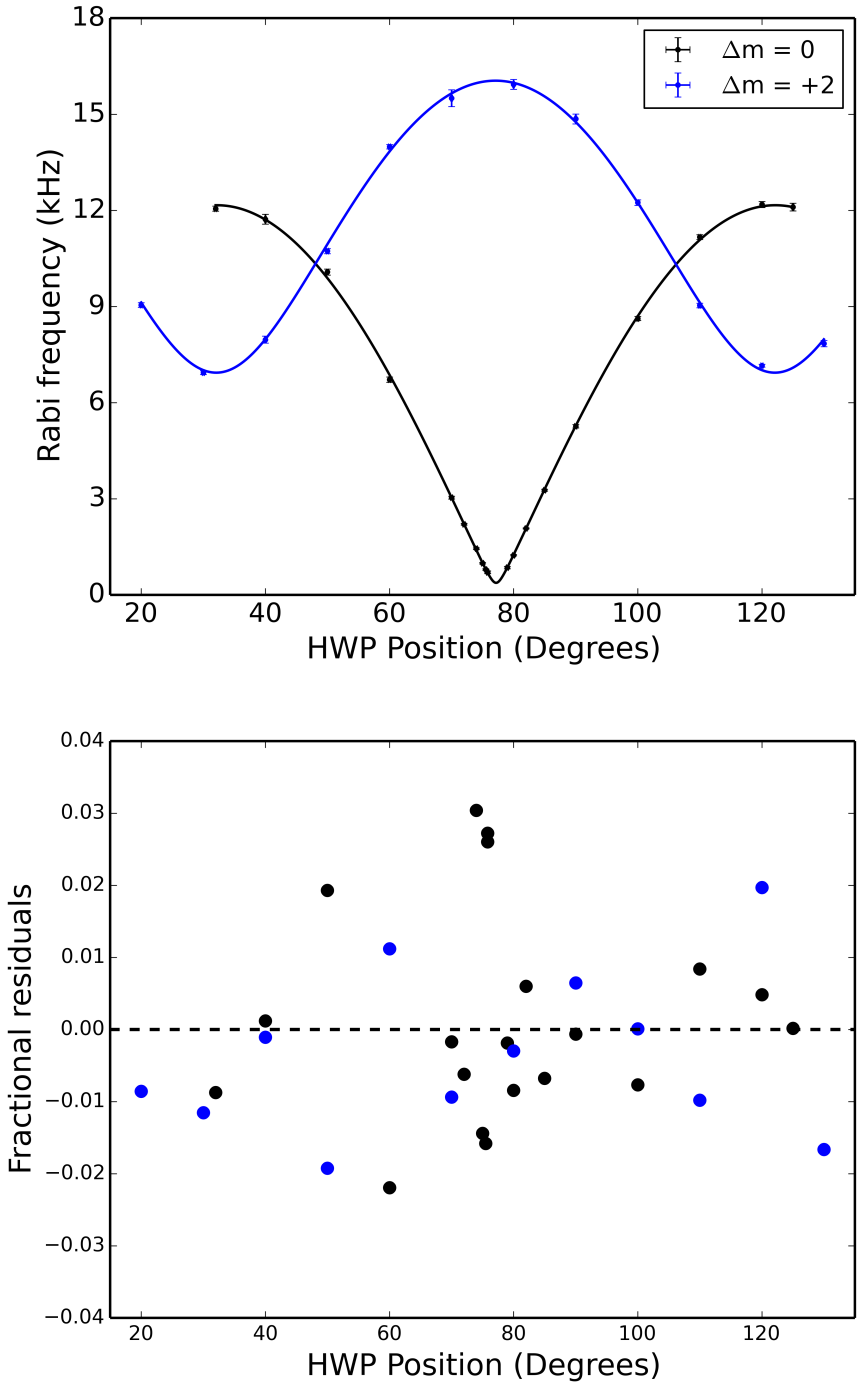

Figure 5.11: Plots of the $\Omega^{(0)}$ and $\Omega^{(+2)}$ data sets along with their fits, which are described in the text. The lower panel displays the fractional residuals for both fits.

Table 5.7: Fit parameters obtained from the $\Omega^{(\pm 2)}$ data fitted simultaneously

$C_{E2}/2\pi$ (kHz)	θ (Degrees)	ϕ_0 (Degrees)	γ (Degrees)	α (Degrees)	χ^2
16.7 ± 0.4	$63.3^\circ \pm 2.5^\circ$	$73.4^\circ \pm 1.1^\circ$	$2.9^\circ \pm 3.5^\circ$	$159^\circ \pm 41^\circ$	2.05

into the general Rabi frequency formulas of Table (5.1) gives,

$$\begin{aligned}\Omega^{(\pm 2)} = E\big|\big[\cos(\theta)\cos\big(\tfrac{\gamma}{2}\big)\sin(2\phi) \pm \sin\big(\tfrac{\gamma}{2}\big)\cos(2\alpha - 2\phi)\big)\big] \\ -i\left[\cos(\theta)\sin\big(\tfrac{\gamma}{2}\big)\sin(2\alpha - 2\phi) \mp \cos\big(\tfrac{\gamma}{2}\big)\cos(2\phi)\right]\big|\end{aligned} \tag{5.42}$$

Fitting either data set to Eq. (5.42) fails because the parameters are not sufficiently well isolated. Moreover, since the functionality for these transition's Rabi frequencies differ only in two places by a sign and share all the same parameters, a direct fit to either set seems an inefficient path for analysis. As a first attempt at fitting the data (though not the last) we can instead seek to fit the two curves simultaneously to their common set of parameters. This is done by defining a cost function that is the sum of both of their weighted residuals squared. The result of the simultaneous fit are summarized in Table (5.7). The simultaneous fit results illustrate the difficulty of fitting to Eqs. (5.42). The parameters obtained are reasonable, but the uncertainties are found to be quite large, especially in the view port parameters that are our quarry. The precision of the analysis can be greatly improved by taking combinations of the data sets that exaggerate the effect of α and Γ separately. The first of these combinations is the ratio $\Omega^{(+2)}/\Omega^{(-2)}$, which for perfect linear polarized light would not deviate from unity. Because in the ratio the electric field amplitude is canceled, any deviation of $\Omega^{(+2)}/\Omega^{(-2)}$ from 1 is due to Γ alone. The purpose of measuring both $\pm$ 2 Rabi frequencies at a given HWP orientation before moving to the next position was to minimize the possibility that the laser field amplitude could have changed significantly between the scans. However over the several years during which this measurement was attempted there was never any indication that the laser power jumped or drifted meaningfully over the course of a day, much less over the 10 minutes these scans took. The particular shape that the ratio takes depends on θ, α, and ϕ_0 in a complicated

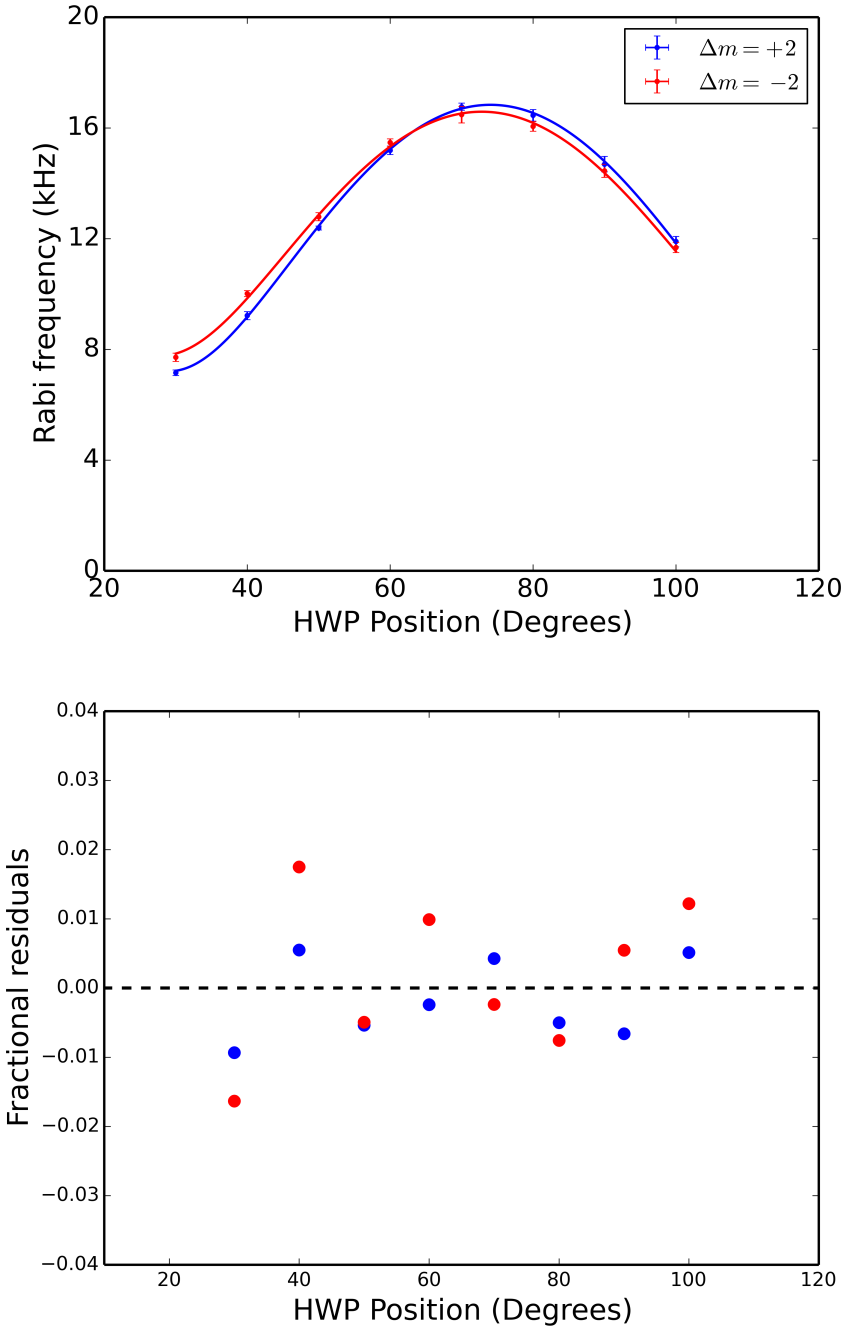

Figure 5.12: The top panel displays plots of the data and the fit of the $\Omega^{(\pm 2)}$ measurements fitted simultaneously to the birefringence laser field model. The blue indicates the Δm = +2 data and the red indicates the Δ = -2 data. The lower panel shows the fractional residuals from the simultaneous fit of both transitions.

Table 5.8: Fit parameters for $\Omega^{(+2)}/\Omega^{(-2)}$ and $\left|\Omega^{(+2)}\right|^2 - \left|\Omega^{(-2)}\right|^2$.

$\Omega^{(+2)}/\Omega^{(-2)}$	γ (Degrees)	α (Degrees)	χ^2
	$2.8^\circ \pm 0.3^\circ$	$155^\circ \pm 9^\circ$	0.40

$\left\|\Omega^{(+2)}\right\|^2 - \left\|\Omega^{(-2)}\right\|^2$	A (Hz^2)	α (Degrees)	χ^2
	$3.57 \pm .07$	$159^\circ \pm 1.6^\circ$	0.41

way, leading to their corresponding uncertainties from the fit being significantly larger than for γ. The second combination of the data is less obvious. By studying Eq. (5.42) one can observe that after evaluating the modulus there will be many redundant terms between the two transitions at quadratic order. These can be canceled out by taking the squared difference between the two data sets $\left|\Omega^{(+2)}\right|^2 - \left|\Omega^{(-2)}\right|^2$. What remains are the interference terms that only differ by their sign, which leads to a dramatic simplification in functionality,

$$\left|\Omega^{(+2)}\right|^2 - \left|\Omega^{(-2)}\right|^2 = 2\,A_{E2}\,\cos(\theta)\sin(\gamma)\,\sin\left[4(\phi - \phi_0) - 2\alpha\right] \tag{5.43}$$

As should be expected, when the retardance is dialed down to zero, $\left|\Omega^{(+2)}\right|^2 - \left|\Omega^{(-2)}\right|^2$ vanishes. Clearly a fit to Eq. (5.43) will have no means to distinguish between A_{E2}, θ, or γ, but since ϕ_0 is already known reasonably well from the simultaneous fit of $\Omega^{(\pm 2)}$ it can be used to get α better than the previous estimates. To do this we replace $2\,A_{E2}\,\cos(\theta)\sin(\gamma)$ with a single amplitude A and plug in for ϕ_0, leaving α as a second model parameter. From these two combinations of the data we obtain the view port parameters that are given in Table (5.8). As hoped, the uncertainties in γ and α are greatly reduced by either fitting procedure. The fit to square difference actually comes out with an uncertainty in α of only $\pm 1^\circ$, however we report $\pm 1.6^\circ$ to account for the propagated uncertainty from ϕ_0.

With that, finally, we can get down to brass tacks. We have all of the pieces needed to calculate our upper bound on M1. It is interesting first to take a close look at the naive analysis approach, using the ideal polarization rotation picture described in Sec. (5.2.1), which serves to make our corrected result seem that much better. Recall that since we were

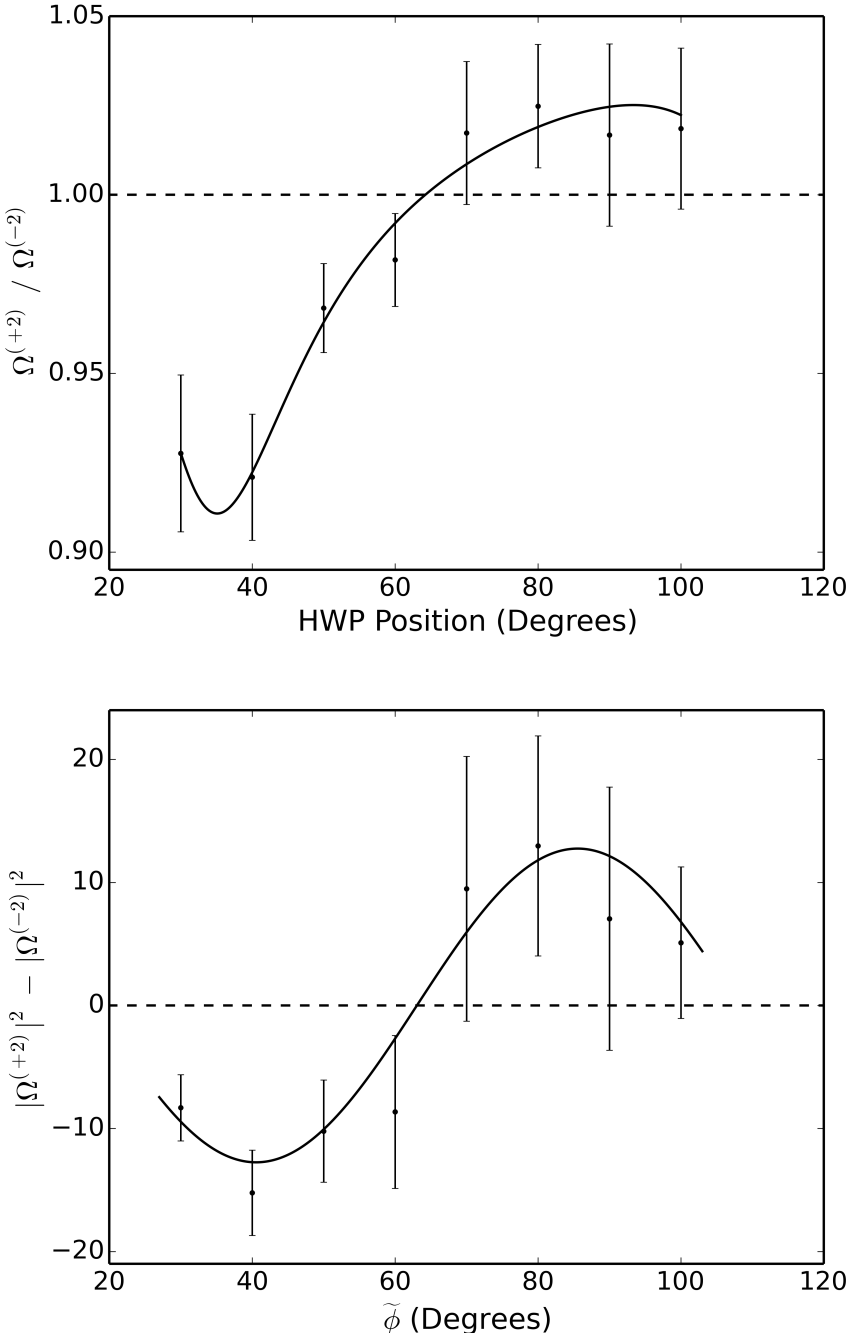

Figure 5.13: The top panel shows the ratio between the $\Omega^{(+2)}$ and $\Omega^{(-2)}$ data sets and the bottom panel shows the square difference $\left|\Omega^{(+2)}\right|^2 - \left|\Omega^{(-2)}\right|^2$. From these curves we are able to extract the view port optical axis orientation and retardance experienced by the 2051 nm beam.

unable to resolve the minimum in $\Omega^{(0)}(\phi)$ we can only report an upper bound on M1, and from the parameters in Table (5.6) we get,

$$\begin{aligned} M1 &< \frac{\Omega^{(0)}_{min}}{\Omega^{(0)}_{max}} \times \sqrt{\frac{3}{5}} \times \frac{c\,k\,E2}{2} \times \cos(\theta) \\ &= 246 \pm 26 \times 10^{-5}\mu_B \qquad \text{(No birefringence correction)} \end{aligned} \tag{5.44}$$

which is not a bad start. This is probably the right time to bring back to mind that the range of predicted values was 17 - 80 ($\times 10^{-5}\mu_B$). The reported uncertainty is the propagated error from the fit parameters as well as from the quadrupole moment, which was assigned a $\pm 1\%$ uncertainty estimated from [19]. The contributed uncertainties from $E2$, θ, and $\Omega^{(0)}_{max}$ are an order of magnitude less than from $\Omega^{(0)}_{min}$. The reason for the relatively large uncertainty there is our inability to resolve the minimum $\Omega^{(0)}_{min}$ properly in the data and the larger than average relative uncertainty in the Rabi frequency measurements near it. For the values of $\Omega^{(0)}(\phi)$ that we were able to measure in the neighborhood of the minimum, M1's contribution is nearly maximized, however it is a relatively small contribution to the still electric-quadrupole dominated values. The fit then must extrapolate the slight deflection of these points due to M1 which is a subtle contribution. The result is that the relative uncertainty contributed from $\Omega^{(0)}_{min}$ alone is approximately equal to the full reported uncertainty in the (uncorrected) M1 upper bound. The next most significant uncertainty is from θ, which contributes $\sim 3 \times 10^{-5}\mu_B$. So far we have not applied any correction to θ either, which is needed to account for skewing in the data from ellipticity, so that uncertainty will increase, but not by enough to make any significant difference. In future generations of this experiment, however, more precise knowledge of θ could become critical and improvements to the system will be discussed that could reduce the 0.4° uncertainty in θ used here. Not far behind θ's contribution is the 1% uncertainty added by E2 which adds $\sim 2.5 \times 10^{-5}\mu_B$ to the total uncertainty. The quadrupole moment is known experimentally from measurements of the spontaneous decay life time, however since the $5D_{3/2}$ manifold is so long lived (at 80 seconds) it is a hard thing to measure precisely and at present has been done only to $\sim 6\%$ in [18]. Improving on this state of affairs, by an (even more patient) lifetime measurement or by some spectroscopic method, could be a useful direction for future studies. The last error propagated is from $\Omega^{(0)}_{max}$ and contributes only $\sim 0.7 \times 10^{-5}\mu_B$

uncertainty to M1, however, like θ, the fitted value of the maximum is slightly shifted by the ellipticity. Now that we know what we have from the ideal experimental analysis we want to correct for the ellipticity induced by the view port birefringence.

To account for the ellipticity induced by view port birefringence we first have to settle on which values of α and Γ will be used. For these we take a weighted average over the different fitting schemes described above and find $\alpha = 158.5^\circ \pm 1.6^\circ$ and $\Gamma = 2.8^\circ \pm 0.3^\circ$. From our simulation we know that θ obtained from the ideal fit to Ω^{+2} should be $\sim 1^\circ$ more than the true value, and so we use the corrected value of $\theta = 63.3^\circ \pm 0.3^\circ$. It is good to see this agree very well with the θ obtained from simultaneously fitting the separate $\Omega^{(\pm 2)}$ measurements, however, to be clear, this had to be verified because of the changes made the the ion's quantization axis. The fact that these values of θ so closely agree suggests that the gradient in our applied magnetic field is in the vertical direction, which minimally affects θ but maximally changes ϕ_0. This correction to θ affects our reported limit for M1 at the level of $1 \times 10^{-5}\mu_B$, so the shift is quite small. In order to subtract off the erroneous E2 coupling appearing in $\Omega^{(0)}_{min}$ we will need the electric field amplitude. This is contained within $\Omega^{(0)}_{max}$ according to,

$$|E| = \frac{4\sqrt{10}}{k} \times \frac{\Omega^{(0)}_{max}}{E2} \tag{5.45}$$

which in principle is also shifted (up in this case) by the ellipticity. However, from our simulation demonstrated in Sec. (5.3.2) we know that for our measured retardance this effect enters at the level of $\sim 0.1 \times 10^{-5}\mu_B$, so it will not be included in this analysis, though it may become relevant to future studies. Now that we have our parameters straightened out, we turn our attention back to the measured minimum which holds in it M1. Using the laser field's of Eqs. (5.38 - 5.39) we have

$$\begin{aligned} \Omega^{(0)}_{min} &= \left| \frac{ik}{4\sqrt{10}\hbar} E2 \sin(2\theta) E_{x'}(|E|, \phi_0, \alpha, \Gamma) - \frac{1}{\sqrt{6}\hbar} M1 \sin(\theta) B_{x'}(|E|, \phi_0, \alpha, \Gamma) \right| \\ &= \left| \Omega^{(\epsilon)}_{min} + A^{(M1)}_{min} \times M1 \right| \end{aligned} \tag{5.46}$$

where the only unknown left is M1. Since $E_{x'}(|E|, \phi_0, \alpha, \Gamma)$ and $B_{x'}(|E|, \phi_0, \alpha, \Gamma)$ are complex functions, solving for M1 by hand is hard and instead we use a numerical root-finding algorithm to do the work. The complexness of the fields makes error propagation an

even harder problem, so instead we estimate our propagated uncertainty by applying the triangle inequality,

$$\Omega_{min}^{(0)} = \left|\Omega_{min}^{(\epsilon)} + A_{min}^{(M1)} \times M1\right| \leq \left|\Omega_{min}^{(\epsilon)}\right| + \left|A_{min}^{(M1)}\right| \times M1 \tag{5.47}$$

and propagate through the magnitudes instead.

Like before, the uncertainty in $\Omega_{min}^{(0)}$ is the largest single contributor to the propagated uncertainty in M1, and this underscores the importance for a next generation measurement to further reduce our system's decoherence rate. Separating out the other parameters individual contributions is trickier here because of how nested the functionality of Eq. (5.46) is. The uncertainty in the erroneous quadrupole coupling[2], $\Omega_{min}^{(\epsilon)}$, contributes near equal part to $\Omega_{min}^{(0)}$, with $A_{min}^{(M1)}$ contributing less but at the same order. These latter two uncertainties are dominated by the uncertainties in the elliptic laser fields, which in turn are dominated by the uncertainty we have in Γ. Table (5.9) summarizes the partial errors in these parameters propagated through to M1. Adding those in quadrature we arrive at our final value,

$$M1 < 93 \pm 39 \times 10^{-5}\mu_B \qquad \text{(with birefringence correction)} \tag{5.48}$$

A palindrome, what were the odds?

[2]In this uncertainty calculation we ignore any contribution from the laser's wave number, k, because it enters many orders of magnitude below those terms listed.

Table 5.9: A summary of the propagated uncertainty to M1. The parameters X are the independent variables from which M1 is calculated, which in turn depend on the parameters Y. The relative uncertainty in $E2$ is taken from [19] to be 1%. The uncertainty in $\left|E_x\right|$ and $\left|B_x\right|$ were obtained by propagating the uncertainties in $\left|E\right|$, ϕ_0, α, and Γ.

Parameter $(X/2\pi)$	Value	Parameter (Y)	$\left\lvert\partial X/\partial Y\right\rvert\ \sigma_Y/X$	$\left\lvert\partial M1/\partial X\right\rvert\ \sigma_X$
$\Omega_{min}^{(0)}$	319 ± 35 Hz	$--$	$--$	$28\times10^{-5}\mu_B$
$\Omega_{min}^{(\epsilon)}$	203 ± 30 Hz			
		$\lvert E_x\rvert$	0.148	
		$E2$	0.010	
		θ	0.005	
				$24\times10^{-5}\mu_B$
$A_{min}^{(M1)}$	.125 ± .004 MHz/μ_B			
		$\lvert B_x\rvert$	0.029	
		θ	0.003	
				$13\times10^{-5}\mu_B$
			Total σ_{M1}	$39\times10^{-5}\mu_B$

5.4 Comments on systematic effects

5.4.1 Magnetic field drift and noise

The magnetic field sensitivity of the 2051 nm transitions was a serious source of systematic effects. The first requirement for the measurement's success was that the ion's quantization axis, set by the magnetic field we apply, be stable over the measurement period. The applied field itself was stable enough in time, however the coils with which we applied the field were not in true Helmholtz configuration causing a significant field gradient. I measured this gradient to be on the order of 100 μG per micron by using the micro-motion compensation voltage to push the ion by a known distance and measure the shift in the transition. The trouble is that immediately after loading an ion the 337 nm photo-ionization laser charges the trap rods. As these patch charges dissipate the ion drifts through the magnetic field gradient. To get a sense of the size of the induced patch charges and the time scale for their dissipation we tracked the ground state spin-flip resonance for about two and a half hours immediately after loading a single ion. For that particular experiment loading the ion took $\sim$ 2 minutes while pulsing the 337 nm laser at 2 Hz, which was a typical loading rate during the period in which the M1 measurement was undertaken. The result of the spin-flip resonance tracking is plotted in Fig. (5.14). Here again we report linear frequencies, as opposed to angular frequencies. By fitting to a decaying exponential we found the resonance drifted by $\sim$ 750 Hz over the two hours with a time constant of $\sim$ 26 minutes. For the narrow spectroscopy carried out near the minimum in $\Omega^{(0)}(\phi)$ this was a potentially large shift; luckily, the solution was easy. Prior to recording any polarization rotation data the ion's position was given about 4 hours to relax (at the time it took about that long to get the 2051 nm into a working state anyway). Waiting patiently is one way to handle this problem, but a more long term solution would be to replace our current coils with true Helmholtz coils to reduce the size of the gradients directly.

That, however, is only one manifestation of the problem. Magnetic fields external to our trap have the same effect, for example, large super-conducting magnets around the basement have been observed to shift our transition's resonances around by as much as kilohertz. Perhaps more melodramatically, it has been documented that the Seattle city

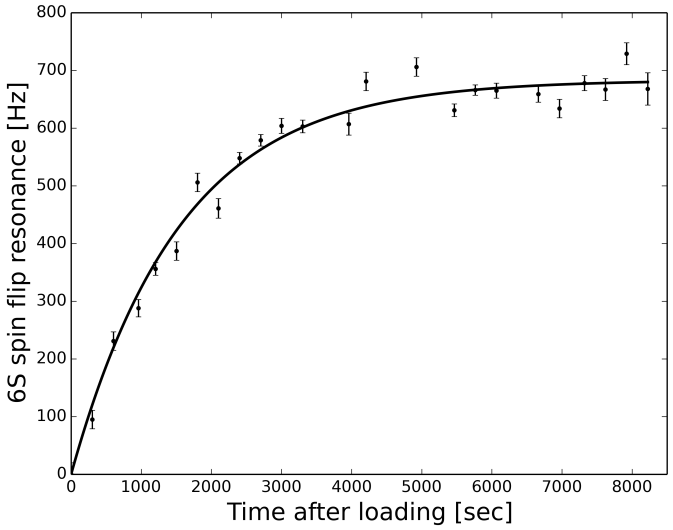

Figure 5.14: Measurements of the ground state Zeeman splitting (or spin-flip resonance frequency) for two and a half hours immediately after loading a single ion. Here we found that the resonance relaxes with a time constant of 26 minutes.

electric buses also have the potential to generate magnetic fields capable of shifting our transition resonances by kilohertz as well [33]. At the time the data presented here were taken this problem had been reduced to the hertz level through actions taken by the City, but it points to the severity of our magnetic field sensitivity. To minimize these external-to-our-trap perturbations most of the data presented here was collected late in the day or over weekends when they were minimized and the resonances themselves were remapped frequently.

Slow variation in the static magnetic field seen by the ion was more of an inconvenience than a genuine problem, however, higher bandwidth noise on that magnetic field was a serious limitation to measuring slow and narrow Rabi oscillations. Magnetic field noise, as opposed to slow drift, translates directly to decoherence in the laser-atom interaction. In our earliest studies on coherently driving the 2051 nm transitions that decoherence rate was estimated to be $\sim$ 300 Hz [70]. From the slowest Rabi frequency oscillation measurements reported above we see this was probably an over estimate for the data reported, however

$\sim$ 100 Hz seems to be a reasonable estimate. For the amount of 2051 nm laser power available at the time of these studies this noise level would have to be reduced by at least two orders of magnitude should we wish to resolve the M1 with the polarization rotation technique. To reduce our decoherence to the hertz level for a next-generation measurement I installed a bi-layer mu-metal magnetic shield around our trapping apparatus shortly before the end of my tenure. To make room for the shielding, the trap and all of the nearby optics had to be lifted 3 inches, which made the installation quite time consuming. After installing the shielding we measured our magnetic field decoherence by performing Rabi oscillations in the ground state, using ARP with the 2051 nm for state read-out. When measured this way the experiment is largely immune to decoherence from either laser parameters or ion temperature, while having an exaggerated sensitivity to magnetic field noise due to the ground state's large effective g-factor. Thus any decoherence observed can be used to place an upper bound on that due to magnetic field noise. By attenuating the RF power delivered to the spin-flip rod we slowed the Rabi oscillation to a (linear) frequency of 120.0 ± 0.7 Hz and observed a decoherence rate of 5 ± 1 Hz, which is a $\sim$30$\times$ decrease in our systems magnetic field noise. The data and fit are displayed in Fig. (5.16). Adjusting these results for the g-factor of the Δm $= 0$ transition we would expect a magnetic field decoherence rate of only 3 Hz in that transition.

Figure 5.15: Photographs of our magnetic shielding before being installed and *in situ*.

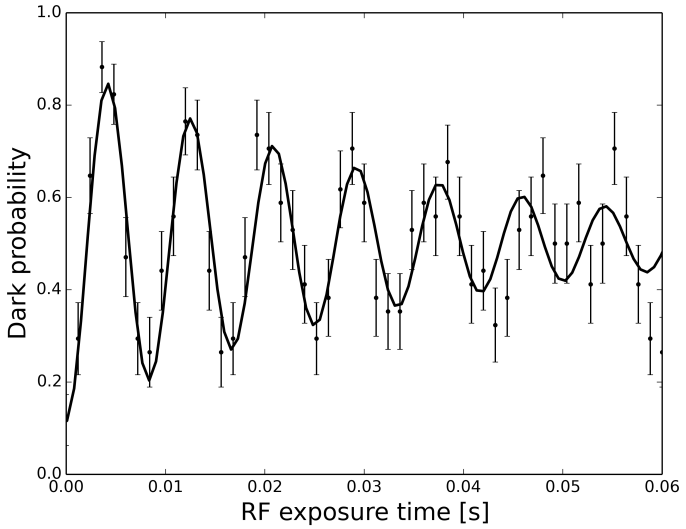

Figure 5.16: An example of a ground state spin-flip Rabi oscillations after the installation of magnetic shielding. From these data we know our magnetic field decoherence rate to be better than 5 ± 1 Hz in the ground state. Notice that the horizontal scale is reported in seconds, instead of our usual micro-seconds.

For fun we also pushed our ground state Rabi oscillations as fast as we could and measured the first 50 oscillations. The data for that measurement are displayed in Fig. (5.17). The fitted (linear) Rabi frequency was 41.735 kHz $\pm$ .003 kHz with a decoherence rate of 0.012 kHz $\pm$ 0.005 kHz and a χ^2 of 1.7. The decoherence rate appears larger here likely because the decay envelop is poorly sampled in the data. From these data, though, we see that the problem of high bandwidth magnetic field noise originating from outside of our shielding is essentially solved.

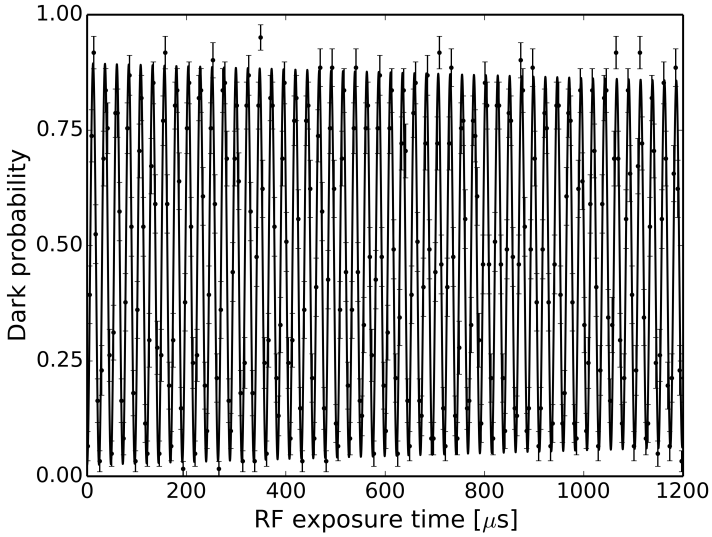

Figure 5.17: The first 50 Rabi oscillations in the ground state. The fitted Rabi frequency was 41.735 kHz ± .003 kHz with a decoherence rate of 0.024 kHz ± 0.009 kHz with a χ^2 of 1.7.

5.4.2 More on polarization distortions and noise

As we have emphasized throughout, polarization distortions are the paramount concern for any M1 measurement. If we consider the theorist's estimate of $\sim 20 \times 10^{-5}\mu_B$ then in the ideal polarization rotation measurement we should expect,

$$A_{M1}/A_{E2} \sim 0.002 \tag{5.49}$$

which is the level to which the laser field's ellipticity must be limited, or calibrated to, for an ultimate measurement. To assess the feasibility of improving our system below this level we consider Eq. (5.35) and Eq. (5.37) and attempt an estimate of where we are now. One complication with polarization noise and distortion is that, as opposed to magnetic field noise which sets a constant decoherence level, polarization effects scale with the laser power so they cannot be beat just by going faster. We have already used some of the induced ellipticity (that from the view port alone) to enhance our measurement sensitivity, however the problems persist in the remaining terms of our laser field expansions.

The most troubling term potentially is the term linear in η, the leaked electric field

through the polarizer, which is,

$$\eta \begin{pmatrix} \cos\Big(2\phi - \zeta\Big) \\ \sin\Big(2\phi - \zeta\Big) \end{pmatrix}$$

because it exactly mimics the laser magnetic field in the ideal polarization rotation experiment. The actual size of η is not known, however, as discussed in Sec. (5.3.1), even before the polarizer the ellipticity in the 2051 nm was on the order of degrees. The polarizer reduces the value further, by a factor of 100, ultimately bringing $\left|\eta/E\right|$ below 0.001. For our presented measurement η is too small to contribute meaningfully, however a next-generation study may wish to further reduce η by employing additional polarizers.

The remaining linear term in Eq. (5.35) actually involves the two parameters $\gamma^{'}$, which is the deviation in the half-wave plate's retardance from $\pi/2$, and ζ, which is the orientation of the polarizer with respect to the normal of the plane spanned by the 2051 nm laser and the ion's quantization axis. The distortion these produce in the laser field's polarization is,

$$iE\,\frac{\gamma^{'}}{2} \begin{pmatrix} \sin\Big(\zeta\Big) \\ -\cos\Big(\zeta\Big) \end{pmatrix}$$

Reasonable estimates for $\gamma^{'}$ and ζ, based on the discussion in Sec. (5.3.1), would be that they each are one degree or so. For these estimates we would have

$$\lesssim iE \begin{pmatrix} 0.001 \\ -0.01 \end{pmatrix}$$

Because of our geometry the effect is minimized along $\mathrm{E}_{x'}$, where we want it least. Here again the contribution from this field perturbation is nearly low enough to get to M1 as it is now and too small to be significant to our current reported limit. Since this term has no ϕ dependence, this perturbation shifts the data in a global and uniform way so it can be corrected for simply. To calibrate $\gamma^{'}$ properly one needs only a pair of sufficiently high extinction polarizers with which it could be measured the same way we roughly estimated view port birefringence. In those studies, recall that we were able to measure the retardance in the optic with a precision of 0.02°, and with the 2051 nm beam we have over $10\times$ more power to perform the calibration with. For the polarizers we had available we were able to

confirm the half wave plate retardance to within only 1° of its manufacturer-specified value, however the wave plate is likely better than that. For this distortion, though, ζ is the real unknown. The complication is that while $\gamma^{'}$ can be calibrated directly, ζ offers no simple means for calibration. The magnetic shielding along with a pair of proper Helmholtz coils would lend a lot of confidence to the claim that the applied magnetic field is parallel to the optics table, which would make reducing ζ easier. Ultimately though, ζ is a consequence of misalignment of a polarizer and not of more fundamental optical properties, so it should be a very surmountable problem in the long term, if it turns out to be one at all.

Given the approximated sizes of the terms at linear order in Eq. (5.35) there is no present need to go further down the expansion to the terms at higher orders. However, there is the more basic matter of our underlying approximation that the view port actually does behave like a single-valued phase retarder. From Fig. (5.6) and Table (5.2) we know that both α and Γ vary over the view port, and that consequently, because the beam has a non-zero spot size, within the beam's profile there is likely to be some variation in polarization. Although the ion only interacts with a very small subset of the beam's spot size, diffraction in the beam will cause that small sample to be composite of the whole illuminated area of the view port. This exactly contradicts the assumption that the view port action can be described as a single phase retarder. The spot size of the beam at the view port is around a few millimeters in diameter, and, referring back to the results of Table (5.2), there was variation in the optical parameters measured in the test view port on that scale. It would seem to some extent that the effect would average out to give some effective retardance and optical axis orientation, but to what extent diffraction contributes to the total decoherence rate is an open question that will need further study. At the end of this section I will present one final measurement that suggests, though non-commitally, that defocussing the beam at the ion may be part of a solution to this potential issue.

5.4.3 Other concerns from the 2051 nm laser

The finite spot size of the beam was only one potential source of issue the 2051 nm could bring to future M1 studies. Because Rabi frequencies are linear in the driving field, intensity noise in the laser must be minimal. When the 2051 nm laser system was first commissioned its intensity noise spectrum was measured; a full description of that characterization is here [69]. The intensity noise distribution they found contained two resonances, one at 35 kHz added to the spectrum by the laser frequency stabilization and another at 400 kHz attributed to spontaneous emission of the Holmium atoms in the oscillator. Both peaks in the relative intensity noise (RIN) came in below -120 dB. Being generous to the problem and estimating the RIN to be constant at that value, the fluctuations in the relative laser field amplitude should be below 10^{-6}, which is far lower than is relevant to our Rabi frequency measurements. Because of our desperation for more 2051 nm power, poverty of good means of detection, and a lack of pick offs, we did not monitor the beam power throughout the experiments described here, however the effect was expected to be so small that was of little concern. Should that situation change, a simple noise-eater could be introduced to the system to further reduce power noise.

The power stability day-to-day was another concern as well. Because of the long setup and data collection time the different $\Omega(\phi)$ measurements had to be taken on different days, over which there could be slight variations in the observed Rabi frequencies. This drift, regardless of its source, did not appear meaningfully across any of the $\Omega(\phi)$ measurements presented earlier. In those data at the end of the day the first half-wave plate position's Rabi frequency was remeasured and checked for consistency. Significant drifts were observed occasionally, however these accumulated over the course of weeks to months, and two probable culprits for these variations were drifts in either 2051 nm pointing or in the laser power. There is no doubt the ion's position in the trap changes over time; Fig. (5.14) can attest to that. However, pointing of the 2051 nm laser, which was checked frequently during my earliest 2051 nm spectroscopy studies, could almost never correct for these deviations, and so they have been attributed to drift in the power. The temperature of the oscillator crystal was changed daily to find the 2051 nm transition in the ULE cavity. Its variation could also

have contributed to any drift in the laser's power. The resolution to these kinds of slow drift inconsistencies is to make the experiment itself faster. At the time the data presented in this thesis was collected each 2051 nm scan took about five minutes, only a few seconds of which were actually used for the different required laser-atom interactions. The rest of the time was accumulated in overhead in the LabView software. Replacing these scripts with faster implementations would be a great improvement to the measurement, not only for the reduction of these systematics but also to increase our data collection rate.

An interesting future study of the laser's performance could be to repeat the RIN measurement described in [69] with and without filtering the 2051 nm polarization, which could provide insights into the polarization noise spectrum of the beam.

5.4.4 Ion temperature effects

The non-zero temperature of our trapped ions imposes important limitations to our Rabi frequency measurements. Speaking of the temperature of a single trapped atom is a nuanced misnomer, but conceptually it is associated with the spread of the ion's wave function over the different harmonic oscillator levels of the trapping potential. For a thermal state distribution, the width of the distribution is related to the average motional state occupation number $\bar{n}$. The trouble is that each of these harmonic oscillator levels over which the ion's wave function is spread experiences a slightly different Rabi frequency. For any given motional sub level, n, the ion's Rabi oscillation is slightly modified according to [57],

$$\Omega_n = \Omega_0 L_n(\eta^2) \tag{5.50}$$

where Ω_0 is the true Rabi frequency, for an ion in its motional ground state, and $L_n(\eta^2)$ are the Laguerre polynomials,

$$L_n(\eta^2) = 1 - \eta^2 n + \frac{1}{4}\eta^4 n(n-1) + \mathcal{O}(\eta^6) \tag{5.51}$$

The parameter η is called the Lamb-Dicke parameter and describes how strongly the ion's motional degrees of freedom are coupled by the recoil momentum of absorbing a photon [76]. For our transitions, $\eta \sim 0.01$, so for an $\bar{n}$ of about 100, which is typical, the first order correction to Ω_0 is about 1%. This could become a significant shift as the precision in the M1 measurement is improved, however, for our presented work this shift was insignificant.

For small η the probability of finding the ion in the excited state is found to be,

$$P_{excited}(t) = \frac{1}{2}\big(1 - \frac{\cos(2\Omega_0 t) + (2\Omega_0 t\eta^2\bar{n})\sin(2\Omega_0 t)}{1 + (2\Omega_0 t\eta^2\bar{n})^2}\big) \tag{5.52}$$

The problem in Eq. (5.52) may not be immediately obvious, but what we see there is a decoherence, through the $2\Omega_0 t\eta^2\bar{n}$ factors, that scales with the Rabi frequency. In effect this limits the number of coherent Rabi oscillations that can be observed. Where this decoherence mechanism is most important is in a situation where one drives a transition much faster than other decoherence mechanisms, such as magnetic field noise, that have a fixed time scale associated with them. For us this situation arises most notably for our $\Omega^{\pm 2}$ measurements. In those we achieve a relative uncertainty in the Rabi frequency measurements of

about 0.5%, which in the ratio and squared-difference approach to birefringence calibration, leads to the unimpressive signal-to-noise obtained in Fig. (5.13). Compare this situation to relative uncertainty obtained in the fast ground state spin-flip data of Fig. (5.17), where a relative uncertainty of 0.007% was achieved. The principle impediment to that kind of highly coherent oscillation in the optical transition is the ion's temperature, which limits the number of oscillations that can be performed. To significantly improve upon this situation would require sub-Doppler cooling methods, like resolved side band cooling [51].

5.5 One final measurement of $\Omega^{(0)}(\phi)$

After installing the magnetic shielding we undertook a final measurement of the 2051 nm Δm = 0 transition polarization rotation measurement. In this last attempt the 2051 nm beam was significantly defocused. The data, which show marked improvement in decoherence compared to before, are plotted in Fig. (5.18). The slowest Rabi flop measured by our system was performed in the course of this experimental run, a plot of which is in Fig. (5.19). For that Rabi oscillation measurement we obtained a Rabi frequency of 44 $\pm$ 1 Hz with a decoherence rate of 7 $\pm$ 1 Hz and a $\chi^2 = 1.34$. This is down from the approximately 650 Hz obtained in our completed measurement. As before we were unable to properly resolve the minimum, however here that minimum was extrapolated to be only 13 $\pm$ 12 Hz. Without knowing the ellipticity we cannot claim any value for M1 from these data, however this is roughly the size that M1 would be expected to appear without any ellipticity. One scenario is that after the shielding installation we chanced upon very nearly aligning the view port optical axis to ϕ_0, where $\Omega^{(0)}_{min}$ occurs. Another could be that in this new geometry the E2-M1 interference is destructive; if the retardance is sufficiently low that E2 is roughly the size of M1 then these could cancel completely. Our extrapolated minimum of 13 $\pm$ 12 Hz could very well represent zero. Following the measurements of Fig. (5.18) we tightened the 2051 nm focus onto the ion and the decoherence rose nearly back to where it was for our previous measurements. This observation may end up being a straw man, however it is a lead worth further investigation.

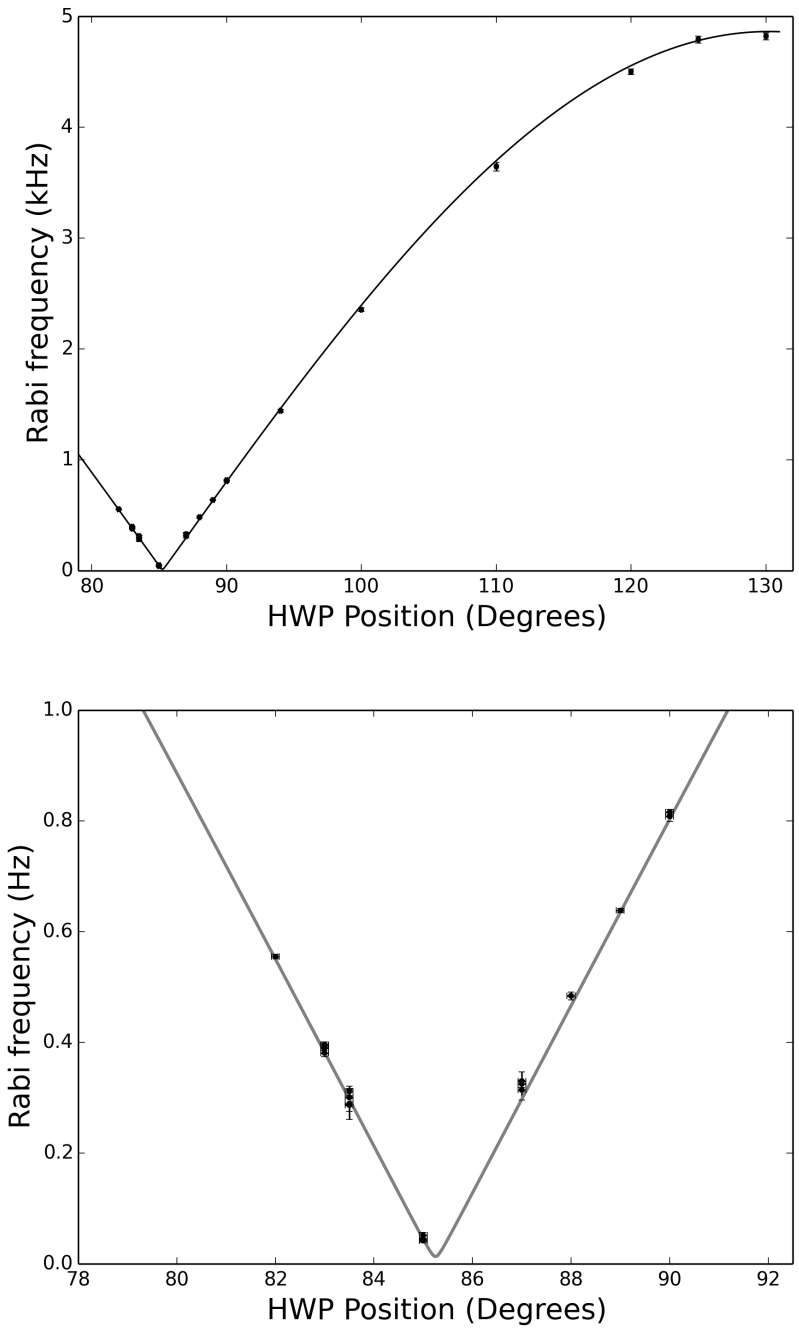

Figure 5.18: Data and fit for a polarization rotation measurement along the Δm = 0 transition after the installation of our magnetic shielding. In this attempt we found A_{E2} = 4863 $\pm$ 17 Hz and A_{M1} = 13 $\pm$ 12 Hz. The phase offset ϕ_0 was equal to 85.25° $\pm$ 0.02°, which indicates a significant change to the experiment's geometry from prior to the shielding's installation.

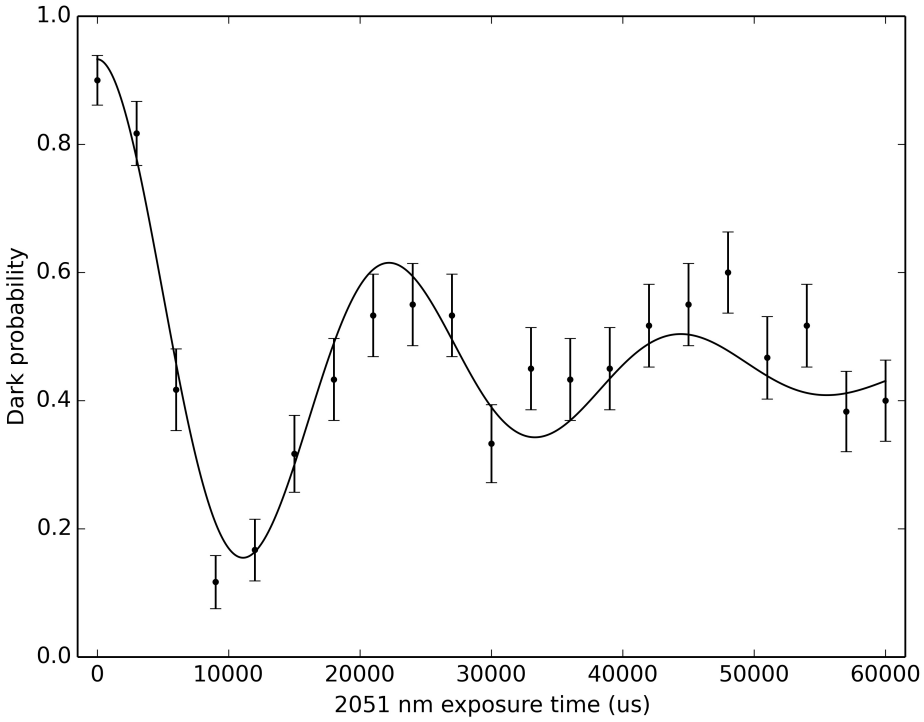

Figure 5.19: The slowest 2051 nm transition observed in our experiment at the time of writing this thesis. For this oscillation we found a (linear) Rabi frequency of 44 ± 1 Hz with a decoherence rate of 7 ± 1 Hz.

BIBLIOGRAPHY

[1] T. D. Lee and C. N. Yang, "Question of parity conservation in weak interactions," *Phys. Rev.*, vol. 104, pp. 254–258, Oct 1956.

[2] C. S. Wu, E. Ambler, R. W. Hayward, D. D. Hoppes, and R. P. Hudson, "Experimental test of parity conservation in beta decay," *Phys. Rev.*, vol. 105, pp. 1413–1415, Feb 1957.

[3] Y. B. Zel'dovich *Sov. Phys. JETP*, vol. 9, p. 682, 1959.

[4] M. Bouchiat and C. Bouchiat, "I. parity violation induced by weak neutral currents in atomic physics," *J. Phys. France*, vol. 35, no. 12, 1974.

[5] Bouchiat, M. A. and Bouchiat, C., "Parity violation induced by weak neutral currents in atomic physics. part ii," *J. Phys. France*, vol. 36, no. 6, pp. 493–509, 1975.

[6] W. J. Marciano and J. L. Rosner, "Atomic parity violation as a probe of new physics," *Phys. Rev. Lett.*, vol. 65, pp. 2963–2966, Dec 1990.

[7] S. G. Porsev, K. Beloy, and A. Derevianko, "Precision determination of electroweak coupling from atomic parity violation and implications for particle physics," *Phys. Rev. Lett.*, vol. 102, p. 181601, May 2009.

[8] C. Burgess and G. Moore, *The standard model: A primer*. Cambridge University Press, 2007.

[9] E. N. Fortson, Y. Pang, and L. Wilets, "Nuclear-structure effects in atomic parity nonconservation," *Phys. Rev. Lett.*, vol. 65, pp. 2857–2860, Dec 1990.

[10] V. Flambaum, I. Khriplovich, and O. Sushkov, "Nuclear anapole moments," *Physics Letters B*, vol. 146, no. 6, pp. 367 – 369, 1984.

[11] C. S. Wood, S. C. Bennett, D. Cho, B. P. Masterson, J. L. Roberts, C. E. Tanner, and C. E. Wieman, "Measurement of parity nonconservation and an anapole moment in cesium," *Science*, vol. 275, no. 5307, pp. 1759–1763, 1997.

[12] E. Fortson and L. Lewis, "Atomic parity nonconservation experiments," *Physics Reports*, vol. 113, no. 5, pp. 289 – 344, 1984.

[13] M.-A. Bouchiat and C. Bouchiat, "Parity violation in atoms," *Reports on Progress in Physics*, vol. 60, no. 11, p. 1351, 1997.

[14] N. Fortson, "Possibility of measuring parity nonconservation with a single trapped atomic ion," *Phys. Rev. Lett.*, vol. 70, pp. 2383–2386, Apr 1993.

[15] V. Dzuba, V. Flambaum, and J. Ginges, "Calculations of parity-nonconserving sd amplitudes in cs, fr, baˆ{+}, and raˆ{+}," *Physical Review A*, vol. 63, no. 6, p. 062101, 2001.

[16] B. K. Sahoo, B. P. Das, R. K. Chaudhuri, and D. Mukherjee, "Theoretical studies of the $6s^2 s_{1/2} \rightarrow 5d^2 d_{3/2}$ parity-nonconserving transition amplitude in ba^+ and associated properties," *Phys. Rev. A*, vol. 75, p. 032507, Mar 2007.

[17] B. M. Roberts, V. A. Dzuba, and V. V. Flambaum, "Quantum electrodynamics corrections to energies, transition amplitudes, and parity nonconservation in rb, cs, ba^+, tl, fr, and ra^+," *Phys. Rev. A*, vol. 87, p. 054502, May 2013.

[18] N. Yu, W. Nagourney, and H. Dehmelt, "Radiative lifetime measurement of the ba^+ metastable $d_{3/2}$ state," *Phys. Rev. Lett.*, vol. 78, pp. 4898–4901, Jun 1997.

[19] B. K. Sahoo, M. R. Islam, B. P. Das, R. K. Chaudhuri, and D. Mukherjee, "Lifetimes of the metastable $^2d_{3/2,5/2}$ states in Ca^+, Sr^+, and Ba^+," *Phys. Rev. A*, vol. 74, p. 062504, Dec 2006.

[20] G. H. Gossel, V. A. Dzuba, and V. V. Flambaum, "Calculation of strongly forbidden $m1$ transitions and g-factor anomalies in atoms considered for parity-nonconservation measurements," *Phys. Rev. A*, vol. 88, p. 034501, Sep 2013.

[21] "Private communication," 2014.

[22] U. I. Safronova, "Relativistic many-body calculation of energies, lifetimes, hyperfine constants, multipole polarizabilities, and blackbody radiation shift in ^{137}Ba ii," *Phys. Rev. A*, vol. 81, p. 052506, May 2010.

[23] V. A. Dzuba, V. V. Flambaum, and M. S. Safronova, "Breit interaction and parity nonconservation in many-electron atoms," *Phys. Rev. A*, vol. 73, p. 022112, Feb 2006.

[24] I. Lindgren and J. Morrison, *Atomic Many-Body Theory.* Springer; Softcover reprint of the original 1st ed. 1982 edition, 1982.

[25] K. Gottfried and T. Yan, *Quantum Mechanics: Fundamentals 2nd Ed.* Springer, 2004.

[26] J. R. Johnson, *Atomic Structure Theory.* Springer Science+Business Media, 2007.

[27] J. J. Sakurai, *Modern Quantum Mechanics Revised Ed.* Addison-Wesley Publishing Company, 1994.

[28] B. W. Shore, *The Theory of Coherent Atomic Excitations Vol.1.* John Wiley and Sons, Inc., 1990.

[29] B. W. Shore, *The Theory of Coherent Atomic Excitations Vol.2.* John Wiley and Sons, Inc., 1990.

[30] R. Shankar, *Principles of Quantum Mechanics, Second Edition.* Springer Science+Business Media, Inc., 1994.

[31] C. J. Foot, *Atomic Physics.* Oxford University Press Inc., New York, 2005.

[32] A. Kramida, Yu. Ralchenko, J. Reader, and and NIST ASD Team. NIST Atomic Spectra Database (ver. 5.2), [Online]. Available: `http://physics.nist.gov/asd` [2014, December 6]. National Institute of Standards and Technology, Gaithersburg, MD., 2014.

[33] M. Hoffman, *Observation of the Nuclear Magnetic Octupole Moment of $^{137}Ba^+$.* PhD thesis, University of Washington, 2014.

[34] C. Auchter, T. W. Noel, M. R. Hoffman, S. R. Williams, and B. B. Blinov, "Measurement of the branching fractions and lifetime of the $5D_{5/2}$ level of ba^+," *Phys. Rev. A*, vol. 90, p. 060501, Dec 2014.

[35] D. Hanneke, S. Fogwell, and G. Gabrielse, "New measurement of the electron magnetic moment and the fine structure constant," *Phys. Rev. Lett.*, vol. 100, p. 120801, Mar 2008.

[36] D. J. Griffiths, *Introduction to Quantum Mechanics, 2nd.* Pearson Education, Inc., 2005.

[37] J. Sucher, "Magnetic dipole transitions in atomic and particle physics: ions and psions," *Reports on Progress in Physics*, vol. 41, no. 11, p. 1781, 1978.

[38] T. Noel, M. R. Dietrich, N. Kurz, G. Shu, J. Wright, and B. B. Blinov, "Adiabatic passage in the presence of noise," *Phys. Rev. A*, vol. 85, p. 023401, Feb 2012.

[39] T. W. Koerber, *Measurement of light shift ratios with a single trapped $^{138}Ba^{+}$ ion, and prospects for a parity violation experiment.* PhD thesis, University of Washington, 2003.

[40] P. K. Ghosh, *Ion Traps.* Oxford University Press Inc., New York, 1995.

[41] D. J. Berkeland, J. D. Miller, J. C. Bergquist, W. M. Itano, and D. J. Wineland, "Minimization of ion micromotion in a paul trap," *Journal of Applied Physics*, vol. 83, no. 10, 1998.

[42] D.J. Wineland, C. Monroe, W.M. Itano, D..Leibfried, B.E. King, D.M. Meekhof, "Experimental issues in coherent quantum-state manipulation of trapped atomic ions," *J.Res.Natl.Inst.Stand.Tech. 103 (1998) 259.*

[43] A. V. Steele, L. R. Churchill, P. F. Griffin, and M. S. Chapman, "Photoionization and photoelectric loading of barium ion traps," *Phys. Rev. A*, vol. 75, p. 053404, May 2007.

[44] G. Herzberg, *Atomic Spectra and Atomic Structure.* Dover publications, 1944.

[45] D. J. Wineland, R. E. Drullinger, and F. L. Walls, "Radiation-pressure cooling of bound resonant absorbers," *Phys. Rev. Lett.*, vol. 40, pp. 1639–1642, Jun 1978.

[46] D. J. Wineland and W. M. Itano, "Laser cooling of atoms," *Phys. Rev. A*, vol. 20, pp. 1521–1540, Oct 1979.

[47] K. B. Davis, M. O. Mewes, M. R. Andrews, N. J. van Druten, D. S. Durfee, D. M. Kurn, and W. Ketterle, "Bose-einstein condensation in a gas of sodium atoms," *Phys. Rev. Lett.*, vol. 75, pp. 3969–3973, Nov 1995.

[48] M. H. Anderson, J. R. Ensher, M. R. Matthews, C. E. Wieman, and E. A. Cornell, "Observation of bose-einstein condensation in a dilute atomic vapor," *Science*, vol. 269, no. 5221, pp. 198–201, 1995.

[49] B. DeMarco and D. S. Jin, "Onset of fermi degeneracy in a trapped atomic gas," *Science*, vol. 285, no. 5434, pp. 1703–1706, 1999.

[50] A. D. Ludlow, M. M. Boyd, J. Ye, E. Peik, and P. O. Schmidt, "Optical atomic clocks," *Rev. Mod. Phys.*, vol. 87, pp. 637–701, Jun 2015.

[51] F. Diedrich, J. C. Bergquist, W. M. Itano, and D. J. Wineland, "Laser cooling to the zero-point energy of motion," *Phys. Rev. Lett.*, vol. 62, pp. 403–406, Jan 1989.

[52] G. Morigi, J. Eschner, J. I. Cirac, and P. Zoller, "Laser cooling of two trapped ions: Sideband cooling beyond the lamb-dicke limit," *Phys. Rev. A*, vol. 59, pp. 3797–3808, May 1999.

[53] C. Monroe, D. M. Meekhof, B. E. King, S. R. Jefferts, W. M. Itano, D. J. Wineland, and P. Gould, "Resolved-sideband raman cooling of a bound atom to the 3d zero-point energy," *Phys. Rev. Lett.*, vol. 75, pp. 4011–4014, Nov 1995.

[54] H. Metcalf, "Entropy exchange in laser cooling," *Phys. Rev. A*, vol. 77, p. 061401, Jun 2008.

[55] C. Corder, B. Arnold, and H. Metcalf, "Laser cooling without spontaneous emission," *Phys. Rev. Lett.*, vol. 114, p. 043002, Jan 2015.

[56] I. Marzoli, J. I. Cirac, R. Blatt, and P. Zoller, "Laser cooling of trapped three-level ions: Designing two-level systems for sideband cooling," *Phys. Rev. A*, vol. 49, pp. 2771–2779, Apr 1994.

[57] C. Roos, *Controlling the quantum state of trapped ions.* PhD thesis, University of Innsbruck, 2000.

[58] H. W, "Optical pumping," *Rev. Mod. Phys.*, vol. 44, pp. 169–249, Apr 1972.

[59] D. J. Berkeland and M. G. Boshier, "Destabilization of dark states and optical spectroscopy in zeeman-degenerate atomic systems," *Phys. Rev. A*, vol. 65, p. 033413, Feb 2002.

[60] W. Nagourney, J. Sandberg, and H. Dehmelt, "Shelved optical electron amplifier: Observation of quantum jumps," *Phys. Rev. Lett.*, vol. 56, pp. 2797–2799, Jun 1986.

[61] N. Kurz, M. R. Dietrich, G. Shu, R. Bowler, J. Salacka, V. Mirgon, and B. B. Blinov, "Measurement of the branching ratio in the $6P_{3/2}$ decay of BaII with a single trapped ion," *Phys. Rev. A*, vol. 77, p. 060501, Jun 2008.

[62] G. Shu, *Novel Ion Traps for Enhanced Fluorescence Collections and Single Photon Sources Based on Barium Ions.* PhD thesis, University of Washington, 2010.

[63] T. W. Noel, *Ion Photon Entanglement with Barium.* PhD thesis, University of Washington, 2014.

[64] A. Hrter, A. Krkow, A. Brunner, and J. Hecker Denschlag, "Long-term drifts of stray electric fields in a paul trap," *Applied Physics B*, vol. 114, no. 1-2, pp. 275–281, 2014.

[65] D. A. Steck, *Quantum Chaos, Transport, and Decoherence in Atom Optics.* PhD thesis, University of Texas at Austin, 2001.

[66] W. L. Trimble, *High-resolution spectroscopy of $^{115}In^{+}$ and prospects for an indium ion optical frequency reference.* PhD thesis, University of Washington, 2007.

[67] W. Nagourney, *Quantum Electronics for Atomic Physics.* Oxford University Press Inc., New York, 2010.

[68] T. W. Hansch and B. Couillaud, "Laser frequency stabilization by polarization spectroscopy of a reflecting cavity," *Opt. Comm.*, vol. 35, pp. 441–444, Dec 1980.

[69] A. Kleczewski, *Towards a measurement of the nuclear magnetic octupole moment in barium-137.* PhD thesis, University of Washington, 2011.

[70] A. Kleczewski, M. R. Hoffman, E. Magnuson, B. B. Blinov, and E. N. Fortson, "Frequency doubling and stabilization of a Tm,Ho:YLF laser at 2051 nm to a high finesse optical cavity.," 2011.

[71] R. Drever, J. Hall, F. Kowalski, J. Hough, G. Ford, A. Munley, and H. Ward, "Laser phase and frequency stabilization using an optical resonator," *Applied Physics B*, vol. 31, no. 2, pp. 97–105, 1983.

[72] E. D. Black, "An introduction to pounddreverhall laser frequency stabilization," *American Journal of Physics*, vol. 69, no. 1, pp. 79–87, 2001.

[73] S. R. Williams, A. Jayakumar, M. R. Hoffman, B. B. Blinov, and E. N. Fortson, "A method for measuring the $6s_{1/2} \leftrightarrow 5d_{3/2}$ magnetic dipole transition moment in Ba^+," *Phys. Rev. A*, vol. 88, p. 012515, Jul 2013.

[74] J. W. Dally and W. F. Riley, *Experimental Stress Analysis 2nd. Ed.* McGraw-Hill Book Company, 1978.

[75] T. N. Vasudevan and R. S. Krishnan, "Dispersion of the stress-optic coefficient in glasses," *Journal of Physics D: Applied Physics*, vol. 5, no. 12, p. 2283, 1972.

[76] D. M. Meekhof, C. Monroe, B. E. King, W. M. Itano, and D. J. Wineland, "Generation of nonclassical motional states of a trapped atom," *Phys. Rev. Lett.*, vol. 76, pp. 1796–1799, Mar 1996.

VITA

Spencer R. Williams was born in Chula Vista, grew up a little, went to school, and kept going. This is the end of all that.